Airborne Wind Energy Systems for Mars Habitats

Master of Science Thesis

Mario Cesar Rodriguez

Delft University of Technology - Technical University of Denmark

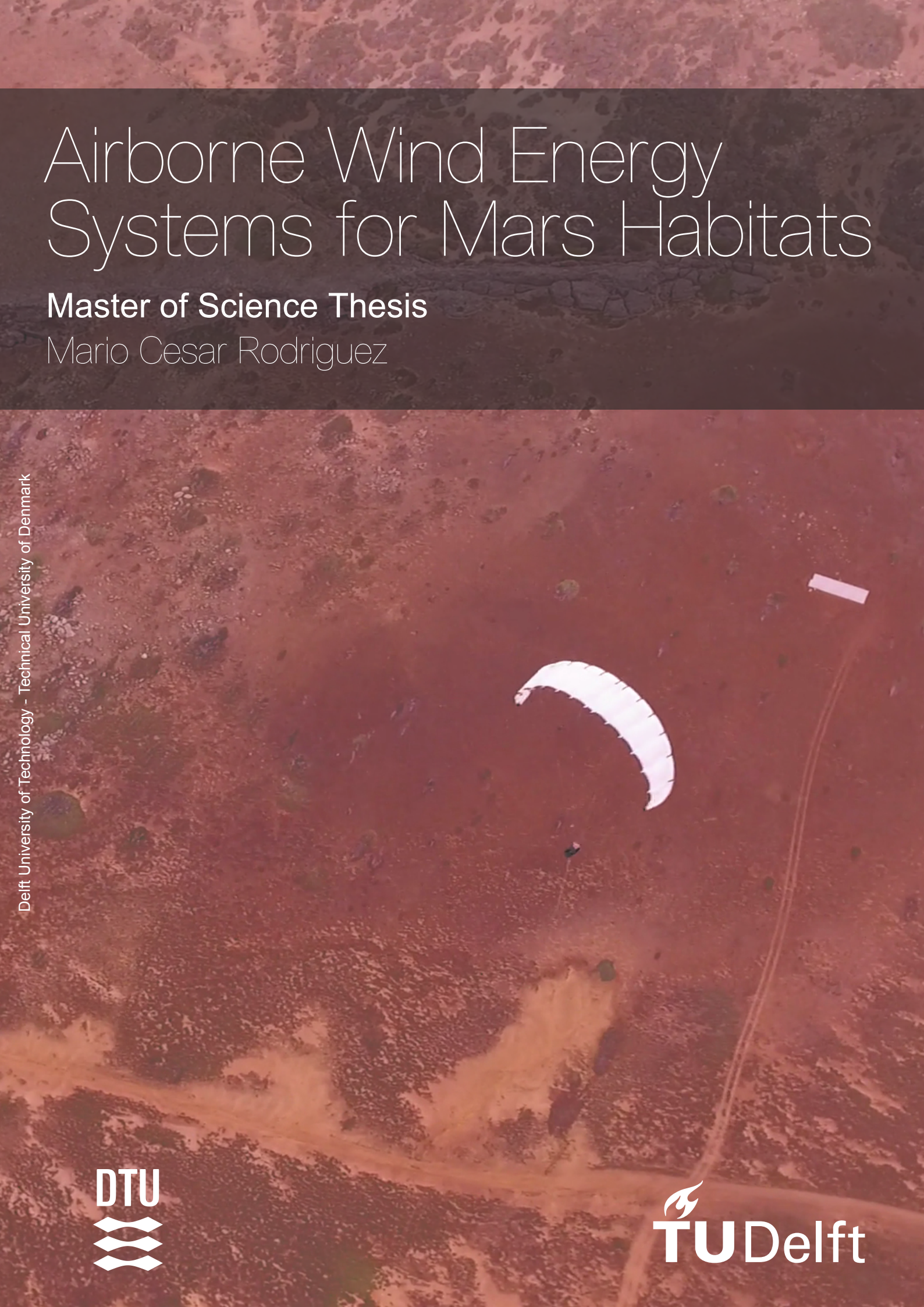

Airborne Wind Energy Systems for Mars Habitats

by

Mario Cesar Rodriguez

to obtain the degree of Master of Science in Aerospace Engineering at the Delft University of Technology and Master of Science in Engineering (European Wind Energy) at Technical University of Denmark, to be defended publicly on 2 Sept 2022 at 1:00 PM.

Faculty of Aerospace Engineering, Delft University of Technology

Student number:	5396506 (TU Delft), s203359 (DTU)	
Project Duration:	November 1, 2021 - July 31, 2022	
Thesis committee:	Dr.-Ing. R. Schmehl,	TU Delft, supervisor
	Dr. M. Gaunaa,	DTU, supervisor
	Prof.Dr. S.J Watson,	TU Delft, reader
	Asst. Prof. A. Cervone	TU Delft, reader

An electronic version of this thesis is available at https://repository.tudelft.nl

Preface

Mars presents many challenges, which result in difficult and interesting design constraints. I learned how to predict wind speeds on another planet where measurements are scarce, proposed a scaled Mars kite design and ran various simulations to assess the expected performance. I learned a great deal about Martian atmospheric conditions, aerodynamic modeling but also doing research with limited information and working around those limitations. I believe this is a fitting end to my European Wind Energy Master's program. This was the most interesting project I have ever worked on and it was a pleasure to work on this everyday.

This Master thesis has allowed me to combine my two passions, namely, wind energy and space exploration. For this, I would like to thank my two supervisors Dr.-Ing. Roland Schmehl (TU Delft) and Dr. Mac Gaunaa (DTU) and student assistant Lora Ouroumova (TU Delft) for helping me along the way as they were critical to my work. Roland, thank you for proving me with the opportunity to do research on this fascinating subject. Mac, your scaling study background is fundamental to this work. Lora and her DSE team laid the foundation I built my thesis around so without them, I would not have been able to make develop all of the work alone.

I like to believe that this thesis will serve as a catalyst for awareness of the technological benefits of AWE and ultimately drive more funding to the AWE sector.

Mario Cesar Rodriguez
Delft, August 2022

Abstract

Using renewable energy to power a Mars habitat is a technological challenge because resources such as solar and wind are significantly weaker than on Earth. This work investigates the feasibility of using airborne wind energy (AWE) systems in combination with solar photovoltaic (PV) modules to power a Mars habitat. The Luchsinger model and the higher fidelity QSM are used to simulate the performance of the AWE system and compared. This thesis builds upon two earlier design synthesis exercise (DSE) projects by implementing a version of the quasi-steady model (QSM) that accounts for the transition phase, models a realistic retraction trajectory, and accounts for the mass of the airborne components. Additionally, the results of the first DSE indicate that the Luchsinger model used did not appear to consume any energy during the reel-in phase, which is not realistic and led to an over-prediction of mean cycle power. However, this thesis aims to implement the Luchsinger model correctly.

Creating a road map for sizing AWE kite systems on Mars is the main objective of this thesis. Since the performance of the AWE system is varying in time and space, the Mars Climate Database (MCD) is used to retrieve atmospheric and surface solar flux data including wind Weibull probability distribution functions (PDF). The second DSE used the MCD and validated the results against wind data from various Mars landers. The MCD is based on numerical simulations of the Martian atmosphere using a general circulation model and validated with available observational data. Seasonal vertical wind profiles are generated from the meteorological data to characterise the boundary layer over time. A scaling study assesses how AWE on Mars differs from that on Earth, performing dimensional analysis. In the system characteristics chapter, the initial sizing of the kite area and mass is computed using the scaling study. The performance models create the power curves, which together with the wind PDFs and surface solar flux data are used in the habitat energy model to verify whether the power requirements are met. Due to an insufficient amount of quantitative information on the energy consumption of the robotic construction of the habitat, the design of the microgrid is covering only the use of the habitat, which is 10 kW of continuous power. This is similar to remote off-grid solutions on Earth, with the additional challenge of having lower resource availability, both for wind and solar. This thesis concludes that various configurations of a hybrid power plant can continuously provide 10 kW of power throughout the entire Martian year. Moreover, the results indicate that using kites alone could generate sufficient power for the habitat without using solar PV.

Contents

List of Figures

List of Tables

Nomenclature

Abbreviations

Abbreviation	Definition
AWE	Airborne wind energy
DSE	Design Synthesis Exercise
ESA	European Space Agency
LEI	Leading edge inflatable
MCD	Mars Climate Database
MOLA	Mars Orbiter Laser Altimeter
NASA	National Aeronautics and Space Administration
PDF	Probability Distribution Function
PV	Photovoltaic
QSM	Quasi-steady model

Greek Symbols

Symbol	Definition	Unit
β	Elevation angle	°
γ	Reeling factor	°
Δt	Change in time	°
ϵ_g	Gravitational importance" for turn radius	-
μ	Dynamic viscosity	kg m^{-1} s^{-1}
μ_P	Velocity parameter	-
κ	Kinematic ratio	-
λ	Tangential velocity factor	-
ρ	Atmospheric density	kg m^{-3}
σ	Non-dimensional control surface deflection (0-1)	-
σ_{grav}	Strain due to gravitational loads	N m^{-2}
ϕ	Azimuth Angle	°

Latin Symbols

Symbol	Definition	Unit
A	Projected kite area	m^2
a_c	Acceleration due to circular motion	m s^{-2}
C_{D}	Effective drag coefficient	-
$C_{\text{D,visc}}$	Kite viscous drag coefficient	-
$C_{\text{d,tether}}$	Tether cross-sectional drag coefficient	-
C_{L}	Lifting coefficient	-
C_P	Power coefficient	-
C_R	Resultant aerodynamic force coefficient	-
C_T	Thrust coefficient	-
C_{turn}	Kite side force to kite pulling force coefficient	-
D	Effective drag	N

Symbol	Definition	Unit
D_k	Kite drag	N
D_t	Tether drag	N
d_T	Tether diameter	N
E_c	Cycle energy	W s
F	Force factor	-
$F_{A,R}$	Resultant radial aerodynamic force	N
$F_{C,R}$	Resultant radial centrifugal force	N
$F_{G,R}$	Resultant radial gravitational force	N
F_{grav}	Gravitational force	N
F_t	Tether forces	N
f_c	Dimensionless power	-
f	Reeling factor	-
g	Gravitational constant	m s^2
L	Lift force	N
ℓ_c	Change in tether length	m
ℓ_T	Tether length	m
LE	Launching easiness	N
M	Mass	kg
Ma	Mach number	-
P_{kite}	Kite mechanical power	W
P_w	Wind power density	W
$\tilde{R}$	Kite maneuverability	-
R	Turning radius	m
Re	Reynolds number	-
T	Tether force	N
$\forbidden{V}$	Volume	m^3
v_a	Apparent velocity	m s^-1
$v_{a,\tau}$	Apparent velocity tangential component	m s^-1
$v_{a,r}$	Apparent velocity radial component	m s^-1
v_K	Kite flight-speed	m s^1
$v_{n,P}$	Nominal Power Wind Speed	m s^1
v_R	Apparent Wind Speed	m s^1
vs	Speed of Sound	m s^1
$v_{n,T}$	Nominal Tether Force Wind Speed	m s^1
v_w	Wind speed	m s^1

Scaling Factors

Symbol	Definition	Unit
K_D	Tether Diameter Scaling Factor	-
K_{kiteCSA}	Kite cross-sectional area scaling factor	-
$K_{\epsilon,g}$	Effect of Gravity on Loops Relative to Aerodynamic Effects Scaling Factor	-
K_μ	Dynamic Viscosity Scaling Factor	-
K_ρ	Density Scaling Factor	-
$K_{\sigma,\text{grav}}$	Strain due to Gravitational Loads Scaling Ratio	-
K_g	Gravitational Acceleration Scaling Factor	-
K_{gf}	Gravitational Force Scaling Factor	-
K_{linear}	Linear length Scaling Factor	-
K_{LE}	Launch Easiness Scaling Factor	-
K_M	Mass Scaling Ratio	-
K_{Ma}	Mach Number Scaling Ratio	-

Symbol	Definition	Unit
$K_{\text{orientation}}$	Kite Orientation	-
K_P	Power Scaling Factor	-
K_{Re}	Reynolds Number Scaling Factor	-
$K_{\tilde{R}}$	Kite Maneuverability Scaling Factor	-
K_T	Tether Force Scaling Factor	-
K_{TA}	Tether Cross Sectional Area Scaling Factor	-
$K_{\text{thickness}}$	Material Thickness Scaling Factor	-
K_v	Wind Speed Scaling Factor	-
K_{vs}	Speed of Sound Scaling Factor	-

1

Introduction

Space exploration has long been fundamental to understanding how the universe works through validating theoretical predictions, such as the expansion of the universe. Humanity's understanding of the universe and how we fit within it, has changed vastly over the centuries. One hundred years ago most astronomers considered the universe to be about 3600 light years in extent, less than a billion years old, and with our solar system near its center [1]. Now astronomers have seen objects 13 billion light-years away in a universe 13.7 billion years old containing hundreds of billions of galaxies [1]. Although humans have not stepped on another heavenly body in over 50 years, the spirit of exploration continues to live on. As of this writing the James Webb telescope is the most sophisticated observatory ever put into operation and is now allowing the public to see what the universe looked like around a quarter of a billion years (possibly back to 100 million years) after the Big Bang, when the first stars and galaxies started to form [2]. The space industry is growing rapidly. Bank of America expects the growing space economy will become a $1.4 trillion market by 2030 [3]. The number of active satellites has more than quadrupled in the last decade, and a new race to space between private companies is ongoing [4]. Using the international space station, humans have held a permanent presence in space for over 22 years [5]. Now the United States Artemis program is expected to begin flights with humans to the moon in May 2024 [6]. NASA plans to use the Artemis program as a stepping stone for human exploration and building self-sustaining outposts on Mars [7].

Although governments and private companies are currently laying the foundations of the lunar economy, space exploration and extra-terrestrial settlements are actually still highly debated. One of the most common issues associated with space exploration is the high costs. Currently, Americans spend almost 2.5 times more on the National Football League (NFL) than on NASA [8][9]. Despite the lack of funding, space technology is already helping solve climate problems on a global scale, because satellites are able to collect data and use that data to solve those problems [10]. Colonizing Mars would result in many new technologies that would benefit people and the Earth. "We're literally talking about putting a million people on another planet in an extremely hostile environment. Many of the challenges that we're going to have to solve to do that are going to also help us solve the climate issue on Earth because it's all about scarce resources, human ingenuity, doing more with less" said Tim Ellis, the CEO and co-founder of Relativity Space, at the 2022 World Economic Forum [10]. NASA and ESA have both subscribed to leaving no traces on other planets [11][12]. Therefore, it is logical mission objective to transition towards sustainable extra-terrestrial habitats. Renewable energy would be one of the founding pillars of this objective.

Renewable energy for a Mars habitat is a technological challenge. Resources such as solar and wind are weaker than on Earth because the atmosphere is 60 times less dense, solar irradiation is roughly half and global dust storms can sometimes render photovoltaic (PV) panels useless for months [13]. The aerodynamic forces depend linearly on the atmospheric density and, consequently, also the tether force depends linearly on the density. That means the kite either has to fly a lot faster (which is limited by the aerodynamic design and the available wind resource) or the wing surface has to be a lot bigger. Because of the low atmospheric density, the Reynolds number on Mars is generally lower than

on Earth, about two orders of magnitude, which is close to laminar flow conditions. This laminar flow around the kite could potentially cause issues with power production due to early flow separation and delayed flow reattachment. The requirements for reliability and robustness are demanding. Martian gravity is a third of that on Earth, which results in a reduction in mass effects and influences the cut-in wind speed of the kite. Wind and solar resources are complementary due to the strong diurnal variations of energy supply and the anti-correlated nature between them. This results in a more consistent power supply. AWE was selected as a solution because of its low mass-to-wing-surface-area ratio, compact packing volume, and high capacity factor which enables it to endure strong dust storms in an airborne parking mode [14].

Given the highly successful and ongoing flights of NASA's Ingenuity Mars helicopter, engineers are turning their attention to future aerial craft for the Red Planet [15] [16]. AWE systems are essentially autonomous drones harvesting power. This could provide much-needed resources and financial support to the AWE industry if it were to be considered a feasible way of generating sufficient power on Mars. AWE is especially well positioned for this opportunity since towered turbines will not work due to their high mass [17], solar energy alone would not be feasible due to long period global dust storms, and radioisotope thermoelectric generators are only an option until the United States national Plutonium-238 stockpile is exhausted [18].

This thesis builds upon the results of two consecutive design synthesis exercise (DSE) groups at the Faculty of Aerospace Engineering of TU Delft [14][19], which succeeded the submission of a proposal to an ESA ideas competition [20]. The winners of the ESA ideas competition, called the Rhizome project group, provided the framework for this thesis project, which necessitates a wind-solar hybrid power plant system that can supply a continuous power supply of 10 kW. The first DSE concluded that renewable energy utilising AWE is a feasible option for a Mars mission, however, without the MCD, their modeling of the environmental conditions was limited. Their trade-off study found that an AWE system using a flexible LEI kite was most ideal for the application. The second DSE improved upon this by incorporating the MCD, which yielded more accurate vertical wind speed profiles at a new habitat location, Protonilus Mensae. Using an engineering trade-off approach optimised for power performance, which is defined as $\frac{C_L^3}{C_D^2}$, the optimal kite design was found to be a semi-rigid swept flying wing. In this thesis, kite design is optimised for specific power because it is considered by NASA to be the true measure of feasibility for wind energy systems on Mars [21]. The specific power is defined as ratio between the power performance and mass of the kite. The AWE design considered in thesis is based on a remote-controlled flexible membrane wing that is operated in pumping cycles. The 20 kW demonstrator system that has originally been developed by the TU Delft spin-off Kitepower for terrestrial applications is used as a reference Earth kite to scale to Martian conditions.

One of the main contributions of this thesis is the scaling study mathematical framework. Horizontal axis wind turbine (HAWT) and vertical axis wind turbine (VAWT) designers utilise scaling laws to redesign components for different wind classes. No such scaling laws exist in the current body of literature for AWE kites for different atmospheric and gravitation effects. Using first principles, scaling laws can be derived and used to get a first-order approximation of the Mars kite design parameters. These scaling laws will be used to compute the initial sizing of the kite. Unlike the first DSE group, this thesis implements the QSM, which accounts for the transition phase, a different retraction trajectory and mass of the system. Additionally, the results of the first DSE indicate that the Luchsinger model used in [14] did not appear to consume any energy during the reel-in phase, which is non-physical and led to an over prediction of mean cycle power. Thus, this coding bug is addressed.

This thesis will not investigate the effects of the low Reynolds number flow (10^4) because too little is known about low-Reynolds airfoil performance in Martian conditions. Realistically, this will result in a slight reduction in performance due to issues with flow separation seen in laminar flow conditions. Further work should include more realistic polar curves computed by means of computational fluid dynamics. This work is only applicable to leading edge inflatable wings and ram-air wings. The MCD does not model the vertical component of the wind realistically. This could affect the performance of the AWE system. Notably, this thesis is not meant to give an optimal design, but instead, bolster AWE on Mars as a proof of concept. Furthermore, the durability of the AWE system is not accounted for in

this analysis. Durability for fabric wings such as LEI, foil and delta kites, is an issue. Performance is compromised soon and lifetime is usually around several hundred hours [22]. Individual developers have reported continuous operation of AWE systems over several days [23]. A Mars mission would require continuous operation for years. It is assumed that by the time humans go to Mars, AWE technology will have matured enough to be much more durable.

This thesis is structured as follows. Chapter 2 begins with a literature review on the basic aspects of AWE generation, the different types of AWE systems, Martian atmospheric conditions, research questions, and an outline. Next, Chapter 3 presents a dimensional-analysis-based method for Earth-based kite systems to be scaled to the Martian environment. Afterwards, Chapter 4 discusses how the wind resource will be investigated, a new habitat location is chosen and the results of a simple wind resource assessment are shown. Chapter 5 discusses the chosen Earth-based kite system and proposes a Mars kite design based on scaling results using the scaling methodology previously explained in Chapter 3. Next, in Chapter 6 the performance of the AWE kite is assessed using two different performance models and the micro-grid subsystems are sized. Lastly, this thesis will end with a concluding chapter where the results of each chapter will be summarised and recommendations for further work are detailed.

2

State-of-the-art/Literature Review

2.1. Background

Resources such as solar and wind are weaker on Mars than on Earth. The solar irradiance is only 43 percent of that on Earth [13], which means roughly twice as many solar PV panels are needed to produce an equivalent amount of power as on Earth. Solar irradiance at the surface level is reduced further by strong seasonal dust storms [24]. Martian gravity is a third of that on Earth [13]. The requirements for reliability and robustness are demanding. The surface temperatures can range from -140 to 30 degrees Celsius [13]. This difference in temperature changes the wind power density proportional to the change in atmospheric density. Where the wind power density is a quantitative measure of wind energy available at any location, which includes the effect of wind velocity and air density. The atmosphere of Mars presents many challenges. Flight on Mars occurs in the low Reynolds number (Re) (10^4), high subsonic Mach number regime (during crosswind maneuvers), which is not typically found in flight on Earth [25]. Thus, ideal airfoils for Mars may look different than those conventionally used on terrestrial flights [25]. For reference, the speed of sound on Mars is about 250 meters per second, which is slower than on Earth, where sound travels through the air at about 340 m/s [26]. This means that transonic effects occur at lower wind speeds than on Earth, which could lead to a reduction in performance because severe instability can occur at transonic speeds [27].

Due to dust storms lasting as long as a few months, a stand-alone solar-powered habitat would likely need an unfeasible amount of energy storage. The main impeding effect of the dust storms is the effect on the irradiation on solar panels, rather than the corrosive effect [28]. Because Mars missions are extremely costly and transportation capacity is limited, in situ material and energy utilization will be crucial [29]. It is crucial to combine resources for an effective renewable energy solution. Wind and solar resources are complementary and result in a more consistent power supply. Batteries are used to store excess energy for periods of exceptionally low energy production.

Nuclear technology is mature and can provide constant reliable power, which makes a valid option. Radioisotope thermoelectric generators are small enough to be used on satellites and various landers [30]. Furthermore, NASA and the U.S. Department of Energy recently developed their ”Kilopower Reactor” using nuclear fission and Stirling technology to generate 10 kilowatts of continuous power [31]. However, radioisotope thermoelectric generators are only an option until national plutonium-238 stockpiles are exhausted [18].

An extensive study on utilizing local material and energy sources for a Martian outpost was presented by [32], covering geothermal, solar, and wind resources and confirming that the exploitation of wind power would be feasible. The use of solar and wind energy systems to power a sustainable Mars base was investigated in [33], suggesting the use of a modified cold-weather wind turbines to cover the missing solar power during month-long Martian global dust storms. While NASA was trying to develop durable wind turbines for demanding conditions such as North of the Arctic circle, the researchers proposed to use this technology to construct future Mars wind turbines [34]. The use of wind energy on

Mars was analyzed by [35], who concluded that despite the low density of the Martian atmosphere, wind speeds are high enough to make wind energy competitive with nuclear power in terms of power produced per unit mass. On the other hand, [36] came to the conclusion that the low density of the Martian atmosphere and the lower level atmospheric wind speeds make wind energy an inappropriate power source. [37] investigated wind as a backup energy source for Mars missions and concluded that in order for towered turbines to be competitive against fission reactor, an equivalent turbine would require weight savings of more than 90% compared to the Earth turbines, which is challenging. A lightweight horizontal axis wind turbine was proposed by [38] and tested in a wind tunnel in a simulated Martian atmospheric environment. Furthermore, a low Reynolds number 500 W vertical axis wind turbine for Mars was proposed in [39].

NASA analysed the performance and feasibility of a wind turbine power system for use on Mars, arguing that the total power output is not the real measure of feasibility. Instead, the real measure is specific power, the ratio of power output to total system mass [21]. AWE systems have a much higher specific power than VAWT or HAWT systems. Therefore, AWE is very competitive with nuclear options and often complementary with PV due to the intermittent nature of wind resource. Moreover, one study even urged others to investigate the feasibility of using modern AWE systems on Mars [17]. Today, Skysails has managed to deploy a 400 m^2 demonstration kite of an innovative wind propulsion technology for cargo vessels [40]. This is considered to be the maximum size limit for such kites.

The reduction of the structural mass required for wind energy harvesting on Mars can be achieved with AWE systems due to the lack of using a tower or foundation. Another advantage is that the AWE system's flight operation can be adjusted continuously to the available wind resource, by which the capacity factor can be maximized for a given wind profile [41]. Over the past two decades, automatic flight control has seen many major advancements, which have contributed to the commercialization of airborne wind energy for terrestrial applications [42], and a number of different implementations have reached the prototype stage [43]. Within this context, researchers of NASA have proposed to use kites for wind energy harvesting on Mars [44].

Typically, an AWE system utilises the principle of a kite pumping cycle to harvest mechanical power from the wind. Put simply, the lift force generated by a wing is a function of a wing's angle of attack. Therefore, a kite coupled with a generator/motor can in principle set a high angle of attack, increasing the lift force and generating power by reeling out the kite. Then, once the tether has reached the maximum length, the angle of attack can be set to zero, which reduces the lift force and the power needed by the motor to reel the kite back in. Once the kite reaches the minimum length, a high angle of attack is set, reel out begins and the pumping cycle starts all over again. Positive mean cycle power is then stored in a short-term energy storage solution. The innovative technology is based on tethered flying devices, either combining onboard wind turbines with a conducting tether or converting the pulling power of the flying devices with ground-based generators [45].

AWE systems could either generate power on the ground with a static ground station, a moving ground station, or the power generation occurs onboard the aircraft during flight. Onboard generation would make the kite heavier and reducing the kite launch mass is important to reduce the kite's cut-in wind speed in Mars's thin atmosphere. Moving ground stations add complexity and weight to the AWE system, therefore only static ground generation systems are considered. As seen in Figure 2.1, the kites can be further divided into rigid, semi-rigid, and flexible kites. Preliminary scaling results indicated that the kite planform area would be required to be at least 200 m^2. A rigid or semi-rigid wing design implies the presence of both rigid and foldable elements in the wing. As the new pumping kite has an area of 200 m^2 the dimensions of the rigid elements would be far greater than previously anticipated which is not in line with the package design. Therefore, only the flexible kites in Figure 2.1, (a) LEI SLE, (b) LEI C-kite, and (c) foil kites can be considered. Due to the existence of readily available data for Kitepower's V3 kite LEI SLE, it is used for this thesis.

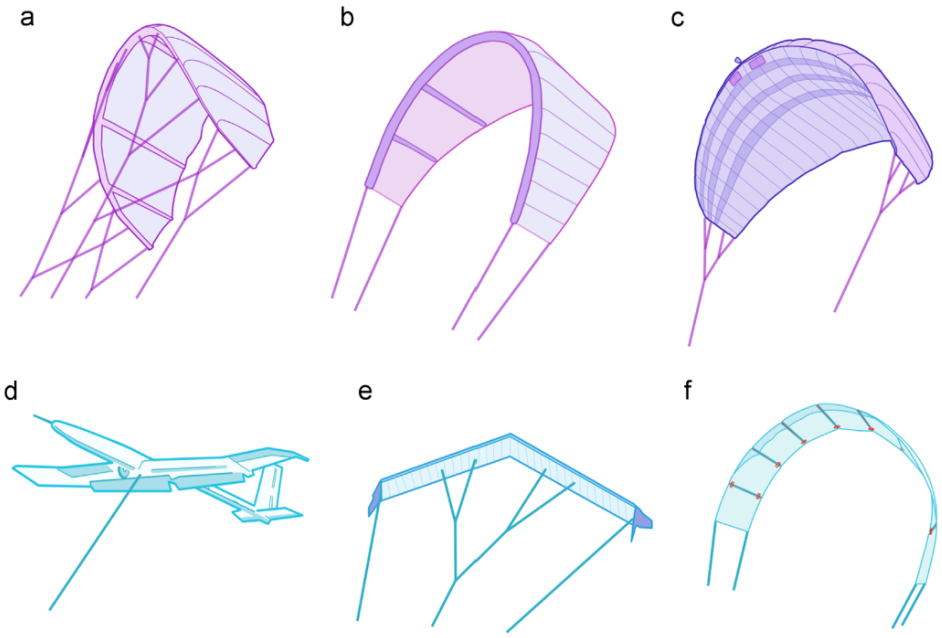

Figure 2.1: Different types of aircraft in Ground-Gen systems. (a) LEI SLE (Leading Edge Inflatable, Supported Leading Edge) Kite; (b) LEI C-kite; (c) Foil Kite, design from Skysails; (d) Glider, design from Ampyx; (e) Swept rigid wind, design from Enerkite; (f) Semi-rigid wing, design form Kitegen. [46]

2.2. Modeling

Two different models were used to quantify the performance of various kite sizes, namely, the Luchsinger Model and the QSM. The reason for using two performance models is to be able to verify the QSM results are similar to the Luchsinger model results. Additionally, the QSM is able to account for the effects of kite and tether mass on the mean cycle power. Both of these models assume that the tether is straight and the aerodynamic properties of the kite are constant per phase. Furthermore, both models assume a constant wind field. A detailed explanation of each model's mathematical framework and assumptions can be seen in Chapter 6.

The Luchsinger kite performance model is used for estimating the net power generated by the kite over a whole cycle [47], called the mean cycle power. The mean cycle power is computed by finding the optimal combination of reel-out and reel-in factors that maximise the normalised cycle power f_c using SciPy's minimize function in python. The QSM instead finds the optimal combination of reel-out and reel-in factors that maximise the cycle power P_c using the same SciPy minimize function. Once the nominal tether force has been reached, the Luchsinger model simply optimises the reel-in factor in order to maximise the normalised cycle power f_c. The QSM uses the nominal tether force to find the aerodynamic force from the kite, which begins the iteration procedure to find the true kinematic ratio and reeling factor, which together with the tether force computes the power. Once the nominal tether force is reached, only the reel-in factor is varied to optimise the mean cycle power. The QSM assumes a static equilibrium of aerodynamic forces, tether, and gravitational forces and can be approximated as a transition through quasi-steady flight states [48]. This allows for time series simulation of the pumping cycle to be done with QSM, while the Luchsinger model can not do this.

The Luchsinger and steady state analysis, explained in Chapter 6, allows for the incorporation of power limits by prescribing the nominal power, tether force, and reeling speed only after the traction power reaches the maximum power limit. This was attempted in the time series QSM, but was not successful. Nevertheless, the maximum power limits occur at high wind speeds that are thought to be infrequent, if at all possible, on Mars. A detailed explanation of each model's derived formulas, assumptions and control strategies is presented in Chapter 6.

2.3. Martian Atmosphere

The atmosphere on Mars is 70 times less dense than on Earth [13]. Although the Martian atmosphere is much less dense, the wind speeds, on the other hand, can be higher than on Earth. At the Viking land sites, the wind speeds varied between 2 to 7 m/s during summer, 5 to 10 m/s during fall, and 17 to 30 m/s during dust storms, resulting in an average of 10 m/s over the whole year [49]. Although there is available meteorological data very close to the surface of Mars and at very high altitudes, little wind data is available at the altitudes of interest for AWE [50]. The literature indicates that the Tharsis bulge has potential good wind resource [51][52]. This is due to the formation of a cross-equatorial jet during the northern hemisphere summer which can result in higher wind speeds at the Tharsis bulge. This is of great importance because summers usually experience lower wind speeds.

Due to the lack of in situ observations of meteorological data, the MCD is used to retrieve wind data including Weibull probability distribution functions [53]. The MCD is based on numerical simulations of the Martian atmosphere using a General Circulation Model and validated with available observational data. Seasonal vertical wind profiles are generated from the meteorological data.

The diurnal variations of wind speed on Mars predicted by the MCD appear to match closely with evidence found in literature Figure 2.2. It appears that there are usually two periods throughout the day where the kite can not fly. These low wind speed periods together usually last about 4 hours and occur a few hours before noon and around midnight. This means that solar PV could help generate energy in the morning when there is no wind.

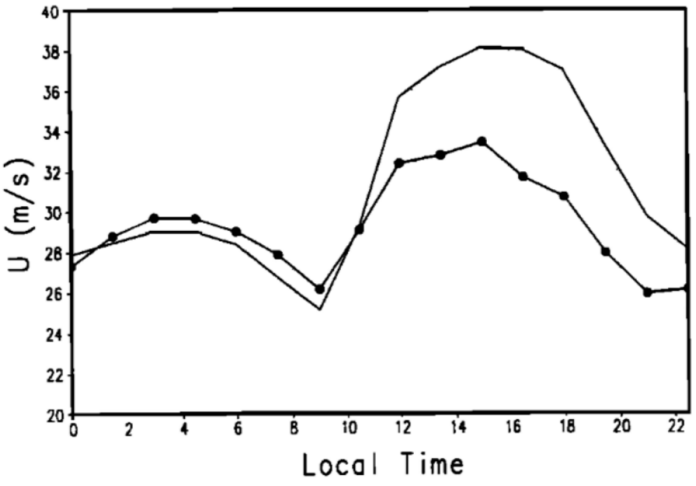

Figure 2.2: Variation of zonal wind u (m s^{-1}) with local time at 30°S using the Mars Global Climate Model in different using flat topography (unmarked curve) and Zonally symmetric topography (dots) [52]

For the northern hemisphere summer, experiments with global climate models have shown that a low altitude (500 m) cross-equatorial jet can form along the eastern flank of Tharsis [54], as seen in Figure 2.3. This low-level jet could be advantageous because it is strongest during Tharsis Bulge's summer, which is usually when the wind speeds are the lowest throughout the year. However, it appears that the low-level jet is too far north of Tharsis Bulge to have any significant effect. A wind resource assessment will indicate the presence of the low-level jet through the characterisation of the atmospheric boundary layer. These are some interesting features of the Tharsis Bulge, but their applicability to AWE have not been assessed by anyone yet, so that's what I'm going to do.

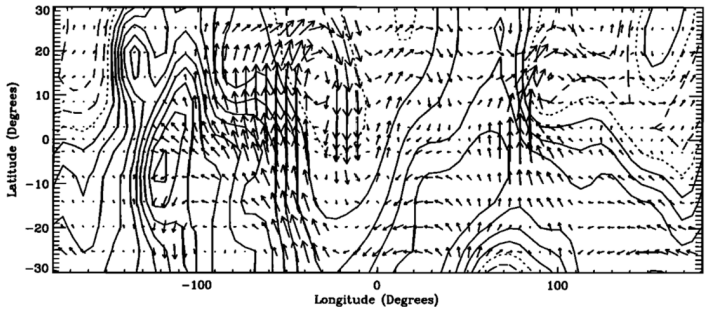

Figure 2.3: Low-level cross-equatorial jet during the Northern Summer [54]

Lastly, [55] investigates the atmospheric thermal circulation of the volcano Arsia Mons using a mesoscale numerical model. Their finds indicate that near the volcano, the vertical component of the wind speed vector increases. However, in the MCD, no vertical wind speeds were detected. The MCD does not model the vertical component of the wind realistically. This could affect the performance of the AWE system.

2.4. Research Questions and Outline

2.4.1. Research Objective

The main research objective of this thesis is to determine the size of the AWE, solar, and energy storage needed to produce 10 kilowatts of continuous power and whether this can be done using kites smaller than the largest flown Earth-made kites today, which are 400 m^2. In order to achieve this goal, an optimal kite design must be devised. Next, meteorological data needs to be collected at various heights throughout an entire Martian year at a particular location set by the Rhizome group. These data points include wind speeds, atmospheric densities and solar flux. The MCD uses a Mars global circulation model refined using the Mars Orbiter Laser Altimeter data from the Mars Global Surveyor space probe [53]. Previous work has validated the accuracy of the MCD and it was deemed good enough to use after being compared to wind measurements from the Viking 1, InSight and Phoenix landers [19].

To extract meaningful energy, the Martian wind speeds must be roughly twice what is seen on Earth, in order to compensate for the low atmospheric density. Next, the MCD wind speed and density data can be used to conduct a scaling study on KitePower's 20-kilowatt V3 kite demonstrator, which will be used to compute the necessary parameters needed to initialize the performance models such as planform area, kite mass, tether mass, and tether force. The accuracy of the scaling study will later be validated by comparing the mean cycle power from V3 kite demonstrator experimental data and the QSM modeling the same kite. Additionally, the scaling study will also give an insight into other important flight parameters, such as Mach and Reynolds numbers, which greatly affect the lift and drag coefficients of an airfoil. Next, the Luchsinger and QSM models are discussed and compared. Finally, using the mean cycle power curves computed from the QSM and Rhizome habitat energy model developed by the Rhizome group is used to assess the performance of the hybrid power plant as a function of kite projected size, number of kites, and solar flux. Different configurations are assessed to ensure power demands are met throughout the Martian year. Solar PV is by far the hardest power source to install, transport, and is an order of magnitude more expensive than AWE systems. Therefore, the use of solar PV is avoided when possible. Additionally, the less energy storage needed, the lighter and less expensive the energy system is. Therefore, increasing the kite size is believed to be more advantageous than installing more energy storage capacity.

Creating a road map for sizing AWE kite systems is a main objective of this project. Since the performance of the AWE system is varying in time and space, a wind resource assessment can be conducted using the MCD after a location has been proposed. Then, a preliminary kite size can then be determined using the scaling study and validated using the QSM and Rhizome habitat energy model.

2.4.2. Research Questions

The main question that this project will be trying to answer is if an AWE system with a kite planform area less than 400 could generate the necessary energy to provide 10 kW of continuous power to a habitat throughout a Martian year. The sub-questions that may spawn are, (1) is there high enough wind speeds to extract meaningful energy and what altitude are the highest average wind speeds found, (2) what type of kite design is optimal for Mars, (3) how should the dimensions of the Mars kite be scaled from existing reference kite design, (4) could the habitat rely solely on wind power and energy storage, and (5) how will the power curves of the AWE system change after implementing the kite and tether mass into the QSM?

3

Scaling Study

Can wind energy be used practically on Mars? A scaling study based on first principles could indicate whether the concept is feasible. The atmospheric viscosity, gravity, speed of sound, and atmospheric density are known and well-defined. The atmospheric density, and speed of sound, vary as a function of the elevation and temperature. Conversely, wind speed is less well known, as it is dependent on many variables, such as elevation, seasonal effects, and local topography. In order to investigate the feasibility of using kite-based wind energy systems on Mars, the following subsection contains a novel theoretical framework for analysing key aspects of these types of systems based on a first-principles scaling approach. After the framework is presented, scaling study results are computed using different atmospheric densities and wind speeds representative of Mars conditions at different locations. Furthermore, the results from this study will provide the initial kite parameters for the system sizing design iteration phase of this thesis. Lastly, it is important to note that this section will also be published in a currently unpublished Springer textbook.

Physical property	Scaling law	Scaling parameter
Atmospheric density	$\rho_{\text{mars}} = K_\rho \rho_{\text{earth}}$	K_ρ
Dynamic viscosity	$\mu_{\text{mars}} = K_\mu \mu_{\text{earth}}$	$K_\mu = 0.722$
Gravity	$g_{\text{mars}} = K_{\text{g}} g_{\text{earth}}$	$K_{\text{g}} = 0.379$
Speed of sound	$a_{\text{mars}} = K_{\text{a}} a_{\text{earth}}$	$K_{\text{a}} = 0.71$
Wind speed	$v_{\text{w, mars}} = K_{\text{vw}} v_{\text{w, earth}}$	K_{vw}

(3.1)

The key performance of a kite wind energy system operated for maximum power capture can be quantified in a simple way using equations described in [56] with the effects of kite elevation angle, β.

Power
$$P_{\text{kite}} = \frac{1}{2}\rho v_w^3 A \frac{4}{27}\frac{C_{\text{L}}^3}{C_{\text{D,eff}}^2}\cos^3\beta \tag{3.2}$$

Tether Force
$$T_{\text{kite}} = \frac{1}{2}\rho v_w^2 A \frac{4}{9}\frac{C_{\text{L}}^3}{C_{\text{D,eff}}^2}\cos^2\beta \tag{3.3}$$

Where A is the kite planform area, β is the kite elevation angle, v_w is the wind speed, C_{L} is the lift coefficient, and $C_{\text{D,eff}}$ is the effective drag coefficient which includes the effect of tether drag. The lift and drag coefficients are defined as:

$$C_{\text{L}} = \frac{L}{\frac{1}{2}\rho v_R^2 A} \qquad C_{\text{D,eff}} = \frac{D_{\text{eff}}}{\frac{1}{2}\rho v_R^2 A} \tag{3.4}$$

Key kite design parameters and performance can be derived for the Mars kite from a reference Earth kite by specifying that the power production should be the same for both systems. It is assumed that the same relative planform and materials will be used for both kites.

3.1. Power

Using Equation 3.2 to equate the power between the Earth and Mars kites results in:

$$\frac{1}{2}\rho_{\text{earth}} v_{w,\text{earth}}^3 A_{\text{earth}} \underbrace{\frac{4}{27}\frac{C_{\text{L,earth}}^3}{C_{\text{D,eff,earth}}^2}\cos^3\beta_{\text{earth}}}_{C_{\text{P,kite,earth}}} = \\ = \frac{1}{2}\rho_{\text{mars}} v_{w,\text{mars}}^3 A_{\text{mars}} \underbrace{\frac{4}{27}\frac{C_{\text{L,mars}}^3}{C_{\text{D,eff,mars}}^2}\cos^3\beta_{\text{mars}}}_{C_{\text{P,kite,mars}}} \tag{3.5}$$

By assuming initially that C_{L}, $C_{\text{D,eff}}$ and β are the same on Mars and Earth, the power coefficients can be assumed to be equal.

$$C_{\text{P,kite,mars}} = C_{\text{P,kite,mars}}$$

Therefore the ratios of the planform areas on mars and the earth kites can be determined from Equation 3.5 as:

$$K_P = \frac{A_{\text{mars}}}{A_{\text{earth}}} = \frac{\frac{C_{\text{P,kite,earth}}}{C_{\text{P,kite,mars}}}}{K_\rho K_{\text{v}}^3} = \frac{1}{K_\rho K_{\text{v}}^3} \tag{3.6}$$

3.2. Tether Force

Equation 3.3 can now be used to compare the tether forces between the Mars and Earth kites.

$$K_T = \frac{T_{\text{kite,mars}}}{T_{\text{kite,earth}}} = \frac{\frac{1}{2}\rho_{\text{mars}} v_{w,\text{mars}}^2 A_{\text{mars}} \overbrace{\frac{4}{9}\frac{C_{\text{L,mars}}^3}{C_{\text{D,eff,mars}}^2}\cos^2\beta_{\text{mars}}}^{C_{\text{T,kite,mars}}}}{\frac{1}{2}\rho_{\text{earth}} v_{w,\text{earth}}^2 A_{\text{earth}} \underbrace{\frac{4}{9}\frac{C_{\text{L,earth}}^3}{C_{\text{D,eff,earth}}^2}\cos^2\beta_{\text{earth}}}_{C_{\text{T,kite,earth}}}} \\ = K_\rho K_{\text{v}}^2 \frac{A_{\text{mars}}}{A_{\text{earth}}} \frac{C_{\text{T,kite,mars}}}{C_{\text{T,kite,earth}}} \tag{3.7}$$

Using the area ratio expression from Equation 3.6 yields:

$$\frac{T_{\text{kite,mars}}}{T_{\text{kite,earth}}} = \frac{1}{K_{\text{v}}} \frac{C_{\text{P,kite}}}{C_{\text{T,kite}}}\bigg|_{\text{earth}} \frac{C_{\text{T,kite}}}{C_{\text{P,kite}}}\bigg|_{\text{mars}} \tag{3.8}$$

The ratio of $C_{\text{P,kite}}$ and $C_{\text{T,kite}}$ can be expressed from Equation 3.2 and Equation 3.3 as:

$$\frac{C_{\text{P,kite}}}{C_{\text{T,kite}}} = \frac{\cos\beta}{3} \tag{3.9}$$

Assuming $\beta_{\text{earth}} = \beta_{\text{mars}}$ as before results in:

$$K_T = \frac{T_{\text{kite,mars}}}{T_{\text{kite,earth}}} = \frac{1}{K_{\text{v}}} \frac{\cos\beta_{\text{earth}}}{\cos\beta_{\text{mars}}} = \frac{1}{K_{\text{v}}} \tag{3.10}$$

3.3. Thickness Ratio

Under the assumption that the dimensioning loads/forces are aerodynamics and that the materials used for the Earth and Mars kites are the same, we can scale ”material thickness” to obtain the same stress in the material for the Earth and the Mars kites.

$$\text{Stress} = \frac{\text{Force}}{\text{Cross-sectional Area}} = \frac{\text{Aerodynamic Force}}{\text{Cross-sectional Area}} \tag{3.11}$$

The aerodynamic force transferred through any given relative cross-section in the kite scale the same way as the total kite aerodynamic forces: $F_{\text{cross-section}} \propto T_{\text{kite}}$. This means that $F_{\text{cross-section,Mars}}/F_{\text{cross-section,Earth}} = T_{\text{cross-section,Mars}}/T_{\text{cross-section,Earth}}$.

The linear length scaling factor between Mars and Earth is the square root of the area scaling factor

$$K_{\text{planform}} = \sqrt{\frac{A_{\text{mars}}}{A_{\text{earth}}}} \tag{3.12}$$

The cross-sectional area of any given relative kite cross section scales with the material thickness scaling factor $K_{\text{thickness}}$ multiplied with the linear planform scaling factor, K_{linear}.

$$K_{\text{kiteCSA}} = K_{\text{thickness}} K_{\text{linear}} \tag{3.13}$$

So the material thickness scaling factor that results in identical stress in the material for the earth and mars kites can be determined by use of Equation 3.11 and Equation 3.13.

$$\begin{aligned}
&\frac{\text{Mars Aerodynamic Forces}}{\text{Mars Cross-sectional Area}} = \frac{\text{Earth Aerodynamic Force}}{\text{Earth Cross-sectional Area}} \\
\Longrightarrow\ &\underbrace{\frac{\text{Mars Aerodynamic Force}}{\text{Earth Aerodynamic Force}}}_{\frac{T_{\text{kite,mars}}}{T_{\text{kite,earth}}}} = \underbrace{\frac{\text{Mars Cross-sectional Area}}{\text{Earth Cross-sectional Area}}}_{K_{\text{linear}} K_{\text{thickness}}} \\
\Longrightarrow\ &K_{\text{thickness}} = \frac{\text{Mars Material Thickness}}{\text{Earth Material Thickness}} = \frac{T_{\text{kite,mars}}}{T_{\text{kite,earth}}} \sqrt{\frac{A_{\text{earth}}}{A_{\text{mars}}}}
\end{aligned} \tag{3.14}$$

Using Equation 3.6 and Equation 3.10 yields:

$$K_{\text{thickness}} = \sqrt{K_\rho K_{\text{v}}} \frac{\cos\beta_{\text{earth}}}{\cos\beta_{\text{mars}}} \sqrt{\frac{C_{\text{P,kite,mars}}}{C_{\text{P,kite,earth}}}} = \sqrt{K_\rho K_{\text{v}}} \tag{3.15}$$

3.4. Mass Ratio

With Equation 3.12 and Equation 3.14 the ratio between the Mars and Earth kite mass can be found. Mass is simply a function of volume and the density of the materials.

$$M = \cancel{V} \rho_{\text{material}} \tag{3.16}$$

The building material is assumed to be the same in both places. Using Equation 3.16, Equation 3.12, Equation 3.14 and Equation 3.6 yields:

$$\begin{aligned}
K_M = \frac{M_{\text{mars}}}{M_{\text{earth}}} = \frac{\cancel{V}_{\text{mars}}}{\cancel{V}_{\text{earth}}} = K_{\text{linear}}^2 K_{\text{thickness}} = \frac{A_{\text{mars}}}{A_{\text{earth}}} K_{\text{thickness}} = \\
= \frac{1}{\sqrt{K_\rho K_{\text{v}}^5}} \frac{\cos\beta_{\text{earth}}}{\cos\beta_{\text{mars}}} \sqrt{\frac{C_{\text{P,kite,earth}}}{C_{\text{P,kite,mars}}}} = \frac{1}{\sqrt{K_\rho K_{\text{v}}^5}}
\end{aligned} \tag{3.17}$$

3.5. Gravity Force Ratio

Next, the ratio of the gravitational forces can be evaluated using the mass ratio expression from Equation 3.17.

$$\begin{aligned}
K_{gf} = \frac{F_{\text{grav,mars}}}{F_{\text{grav,earth}}} = \frac{M_{\text{mars}}}{M_{\text{earth}}} \frac{g_{\text{mars}}}{g_{\text{earth}}} = \sqrt{\frac{K_g^2}{K_\rho K_{\text{v}}^5}} \frac{\cos\beta_{\text{earth}}}{\cos\beta_{\text{mars}}} \sqrt{\frac{C_{\text{P,kite,earth}}}{C_{\text{P,kite,mars}}}} = \\
= \sqrt{\frac{K_g^2}{K_\rho K_{\text{v}}^5}}
\end{aligned} \tag{3.18}$$

3.6. Launching Easiness Ratio

A measure of how easily a kite is launched is the ratio of aerodynamic forces to gravity forces; the so-called launching easiness or "LE". The ratio between the Mars and Earth LE can be used to determine how the relative difficulty in launching the kite change.

$$K_{LE} = \frac{LE_{\text{mars}}}{LE_{\text{earth}}} = \frac{\frac{F_{\text{aero,mars}}}{F_{\text{grav,mars}}}}{\frac{F_{\text{aero,earth}}}{F_{\text{grav,earth}}}} = \frac{F_{\text{aero,mars}}}{F_{\text{aero,earth}}}\frac{F_{\text{grav,earth}}}{F_{\text{grav,mars}}} = \frac{T_{\text{kite,mars}}}{T_{\text{kite,earth}}}\frac{F_{\text{grav,earth}}}{F_{\text{grav,mars}}} =$$
$$= \sqrt{\frac{K_\rho K_{\text{v}}^3}{K_g^2}}\sqrt{\frac{C_{\text{P,kite,mars}}}{C_{\text{P,kite,earth}}}} = \sqrt{\frac{K_\rho K_{\text{v}}^3}{K_g^2}} \tag{3.19}$$

3.7. Strain Ratio due to Gravitational Loads

Next, the ratio of material strain due to gravitational loads is computed. In the equation below, K is a constant which depends on where the material strain is evaluated in the kite. The relative location of the strain evaluation point on the Mars and Earth kites should be in the same location, so K is the same on Mars and on Earth.

$$\sigma_{\text{grav}} A_{\text{cross}} = K F_{\text{grav}} \longrightarrow \sigma_{\text{grav}} = \frac{K F_{\text{grav}}}{A_{\text{cross}}} \tag{3.20}$$

$$K_{\sigma,\text{grav}} = \frac{\sigma_{\text{grav,mars}}}{\sigma_{\text{grav,earth}}} = \frac{F_{\text{grav,mars}}}{F_{\text{grav,earth}}}\underbrace{\frac{A_{\text{cross,mars}}}{A_{\text{cross,earth}}}}_{\frac{1}{K_{\text{thickness}}K_{\text{linear}}}} = \sqrt{\frac{K_g^2}{K_g K_{\text{v}}^3}}\sqrt{\frac{C_{\text{P,kite,earth}}}{C_{\text{P,kite,mars}}}} =$$
$$= \sqrt{\frac{K_g^2}{K_g K_{\text{v}}^3}} \tag{3.21}$$

3.8. Mach Number Ratio

The Mach number, reference flow speed to speed of sound, is used to quantify to what extent compressible flow effects matter. Therefore the ratio of the Mach numbers on Mars and Earth will indicate whether compressible effects might play a role in the Mars environment. From [56] the relative wind speed observed by the kite during crosswind manoeuvres is

$$v_R = \frac{2}{3} v_w \frac{C_{\text{L}}}{C_{\text{D,eff}}} \tag{3.22}$$

Again assuming that $\left.\frac{C_{\text{L}}}{C_{\text{D,eff}}}\right|_{\text{mars}} = \left.\frac{C_{\text{L}}}{C_{\text{D,eff}}}\right|_{\text{earth}}$ yields:

$$K_{\text{Ma}} = \frac{\text{M}_{\text{A,mars}}}{\text{M}_{\text{A,earth}}} = \frac{\left.\frac{v_R}{v_{\text{S}}}\right|_{\text{mars}}}{\left.\frac{v_R}{v_{\text{S}}}\right|_{\text{earth}}} = \frac{v_{\text{R,mars}}}{v_{\text{R,earth}}}\frac{v_{\text{S,earth}}}{v_{\text{S,mars}}} = \frac{K_{\text{v}}\left.\frac{C_{\text{L}}}{C_{\text{D,eff}}}\right|_{\text{mars}}}{K_{\text{vs}}\left.\frac{C_{\text{L}}}{C_{\text{D,eff}}}\right|_{\text{earth}}} = \frac{K_{\text{v}}}{K_{\text{vs}}} \tag{3.23}$$

3.9. Reynolds Number Ratio

The Reynolds number ratio is of interest because the aerodynamic performance of the airfoils on the kite depends on it. Lowering the Reynolds number results in earlier separation, lower maximum lift, and higher airfoil drag [25].

$$K_{\text{Re}} = \frac{\text{Re}_{\text{mars}}}{\text{Re}_{\text{earth}}} = \frac{\left.\frac{\rho v_R C}{\mu}\right|_{\text{mars}}}{\left.\frac{\rho v_R C}{\mu}\right|_{\text{earth}}} = \underbrace{\frac{\rho_{\text{mars}}}{\rho_{\text{earth}}}}_{K_\rho}\underbrace{\frac{v_{\text{R,mars}}}{v_{\text{R,earth}}}}_{K_{\text{v}}\frac{\left.\frac{C_{\text{L}}}{C_{\text{D,eff}}}\right|_{\text{mars}}}{\left.\frac{C_{\text{L}}}{C_{\text{D,eff}}}\right|_{\text{earth}}}}\underbrace{\frac{C_{\text{mars}}}{C_{\text{earth}}}}_{K_{\text{planform}}}\underbrace{\frac{1}{\frac{\mu_{\text{mars}}}{\mu}}}_{\frac{\mu_{\text{mars}}}{\mu_{\text{earth}}}=K_\mu}$$

$$K_{\mathsf{Re}} = \frac{\mathsf{Re}_{\mathsf{mars}}}{\mathsf{Re}_{\mathsf{earth}}} = \frac{K_\rho K_{\mathsf{v}}}{K_\mu} \frac{\left.\frac{C_{\mathsf{L}}}{C_{\mathsf{D,eff}}}\right|_{\mathsf{mars}}}{\left.\frac{C_{\mathsf{L}}}{C_{\mathsf{D,eff}}}\right|_{\mathsf{earth}}} \sqrt{\frac{A_{\mathsf{mars}}}{A_{\mathsf{earth}}}}$$

$$= \sqrt{\frac{K_\rho}{K_{\mathsf{v}} K_\mu^2}} \frac{\left.\frac{C_{\mathsf{L}}}{C_{\mathsf{D,eff}}}\right|_{\mathsf{mars}}}{\left.\frac{C_{\mathsf{L}}}{C_{\mathsf{D,eff}}}\right|_{\mathsf{earth}}} \sqrt{\frac{C_{\mathsf{P,kite,earth}}}{C_{\mathsf{P,kite,mars}}}} = \sqrt{\frac{K_\rho}{K_{\mathsf{v}} K_\mu^2}} \tag{3.24}$$

Our resultant range of Reynolds numbers is approximately 5% to 12% of the Earth case. This means that the kite system should probably not be made too small of a power rating because of potential issues with bad aerodynamics due to low Reynolds conditions. Maybe then the assumption of $C_{\mathsf{D,eff,mars}} = C_{\mathsf{D,eff,earth}}$ is fine. Additionally, $C_{\mathsf{P,kite,mars}} = C_{\mathsf{P,kite,earth}}$ is considered fine as well.

3.10. Maneuverability Ratio

How differently does a Mars kite manoeuvre compared to an Earth kite? A suitable non-dimensional measure of the manoeuvrability of the kite is the turning radius divided by the kite's linear size.

$$\tilde{R} = \frac{R}{\sqrt{A}} \tag{3.25}$$

The determination of turning radius can be done by balancing radial forces during circular motion: centrifugal, aerodynamic, and gravitational.

$$F_{C,R} = F_{A,R} + F_{G,R} \tag{3.26}$$

The centrifugal force can be described as:

$$F_{C,R} = Ma_c = M\frac{v_K^2}{R} \tag{3.27}$$

v_K is kite speed and R is the turning radius. The aerodynamic side force can be expressed as:

$$F_{A,R} = T_{\mathsf{kite}} \delta C_{\mathsf{turn}} \tag{3.28}$$

Here T_{kite} is the total aerodynamic force, δ is known as the non-dimensional control surface deflection (0-1) and C_{turn} is the coefficient stating how big a fraction of the kite pulling force the side force can be. C_{turn} depends on the kite design, not on the scaling, so it is the same value for the Mars kite and the Earth Kite.

The gravitational force component in the direction of turn can be expressed as:

$$F_{G,R} = Mg \underbrace{K_{\mathsf{orientation}}}_{\overline{e}_g \overline{e}_{\mathsf{rotational\ center}}} \tag{3.29}$$

Where $(-1 \leq K_{\mathsf{orientation}} \leq 1)$ and depends on the kite orientation.
Substituting Equation 3.27, Equation 3.28 and Equation 3.29 into Equation 3.26 fields:

$$M\frac{v_K^2}{R} = T_{\mathsf{kite}} \delta C_{\mathsf{turn}} + MgK_{\mathsf{orientation}}$$

$$\longrightarrow R = \frac{Mv_K^2}{T_{\mathsf{kite}} \delta C_{\mathsf{turn}} + MgK_{\mathsf{orientation}}} = \frac{Mv_K^2}{T_{\mathsf{kite}} \delta C_{\mathsf{turn}}(1+\epsilon_g)} \tag{3.30}$$

Where ϵ_g is a non-dimensional parameter for "gravitational importance" for turn radius.

$$\epsilon_g = \frac{MgK_{\mathsf{orientation}}}{T\delta C_{\mathsf{turn}}} \tag{3.31}$$

Substituting Equation 3.30 into Equation 3.25 yields:

$$\tilde{R} = \frac{Mv_K^2}{\sqrt{A} T_{\mathsf{kite}} \delta C_{\mathsf{turn}}(1+\epsilon_g)} \tag{3.32}$$

A measure of the ”turning capability” of ”the scaled design” kite on Mars/Earth can be quantified by $\tilde{R}_{\text{mars}}/\tilde{R}_{\text{earth}}$. If $\tilde{R}_{\text{mars}}/\tilde{R}_{\text{earth}} = 1$ this means the turning capability relative to kite size is the same.

$$\frac{\tilde{R}_{\text{mars}}}{\tilde{R}_{\text{earth}}} = \frac{\frac{M_{\text{mars}}}{M_{\text{earth}}}\frac{v_{\text{K,mars}}^2}{v_{\text{K,earth}}^2}}{\sqrt{\frac{A_{\text{mars}}}{A_{\text{earth}}}}\frac{T_{\text{mars}}}{T_{\text{earth}}}\frac{\delta_{\text{mars}}}{\delta_{\text{earth}}}\frac{C_{\text{turn,mars}}}{C_{\text{turn,earth}}}} \tag{3.33}$$

Previously, it was assumed that $\frac{C_{\text{L}}}{C_{\text{D,eff}}}\Big|_{\text{mars}}$ is equal to $\frac{C_{\text{L}}}{C_{\text{D,eff}}}\Big|_{\text{earth}}$. This implies that $\frac{v_K}{v_w}\Big|_{\text{mars}} = \frac{v_K}{v_w}\Big|_{\text{earth}} \iff \frac{v_{\text{K,mars}}}{v_{\text{K,earth}}} = \frac{v_{w,mars}}{v_{w,earth}} = K_v$.

If a simple scaling of the same kite geometry is considered $C_{\text{turn,mars}} = C_{\text{turn,earth}}$. Furthermore, if $\delta_{\text{mars}} = \delta_{\text{earth}}$ is considered, the maneuvering capability can directly be evaluated through $\tilde{R}_{\text{mars}}/\tilde{R}_{\text{earth}}$. Substituting Equation 3.17, Equation 3.10 and Equation 3.6 into Equation 3.33 yields:

$$K_{\tilde{R}} = \frac{\tilde{R}_{\text{mars}}}{\tilde{R}_{\text{earth}}} = \frac{K_\rho^{-0.5}K_v^{-2.5}K_v^2}{\sqrt{K_\rho^{-1}K_v^{-3}}K_v^{-1}1} = K_v^2 \tag{3.34}$$

For the same control surface input, the Mars kite will have a turning radius that is proportional to K_v^2. Put another way, the Mars kite needs more effective control surfaces to have the same relative turning radius as the Earth kite.

Next, the effect of gravity on loops relative to aerodynamic effects is investigated.

$$\frac{\epsilon_{\text{g,mars}}}{\epsilon_{\text{g,earth}}} = \frac{M_{\text{mars}}}{M_{\text{earth}}}\frac{g_{\text{mars}}}{g_{\text{earth}}}\frac{1}{\frac{T_{\text{mars}}}{T_{\text{earth}}}}\underbrace{\frac{1}{\frac{\delta_{\text{mars}}}{\delta_{\text{earth}}}}\frac{\frac{K_{\text{orientation,mars}}}{K_{\text{orientation,earth}}}}{\frac{C_{\text{turn,mars}}}{C_{\text{turn,earth}}}}}_{1}$$

Assuming the same control deflection, the same orientation, and the same kite design.

$$K_{\epsilon,g} = \frac{\epsilon_{\text{g,mars}}}{\epsilon_{\text{g,earth}}} = K_\rho^{-\frac{1}{2}}K_v^{-\frac{5}{2}}K_gK_v = K_\rho^{-\frac{1}{2}}K_v^{-\frac{3}{2}}K_g \tag{3.35}$$

Therefore, the relative variation in R (or the control input) will be roughly the same on Mars and Earth. In other words, the Mars kite will have relatively the same issues with non-consistent power due to gravitational effects for the kite where the aerodynamic control surfaces have not yet been upscaled. If the control authority of the mars kite is increased, which corresponds to $\delta_{\text{mars}}/\delta_{\text{earth}} > 1$, this effect is reduced.

3.11. Tether Diameter Ratio

The tether drag is a function of tether diameter, which is influenced by the maximum tension force on the tether during the reel-out phase of the kite pumping cycle. The tether stress ratio can be expressed as such:

$$\frac{\text{Force}}{\text{Cross-sectional Area}} = \frac{\frac{T_{\text{mars}}}{T_{\text{earth}}}}{\frac{A_{\text{tether,mars}}}{A_{\text{tether,mars}}}} = \frac{K_T}{K_{TA}} \tag{3.36}$$

In order for the stress on the tether to be the same for both the Mars and Earth kites, the ratio is said to be one.

$$\frac{K_T}{K_{TA}} = 1 \longrightarrow K_T = K_{TA} \tag{3.37}$$

$$K_T = \frac{A_{\text{tether,mars}}}{A_{\text{tether,mars}}} = \frac{D_{\text{tether,mars}}^2}{D_{\text{tether,earth}}^2} = K_D^2 \tag{3.38}$$

Lastly, the tether diameter ratio can be expressed as such:

$$K_D = \sqrt{K_T} = \frac{1}{\sqrt{K_v}} \tag{3.39}$$

3.12. Evaluations of Assumptions

$$C_{\text{L,mars}} = C_{\text{L,earth}} \qquad C_{\text{D,eff,mars}} = C_{\text{C,eff,earth}} \qquad \beta_{\text{mars}} = \beta_{\text{earth}}$$

The choice for which β is difficult since it is dependent on tether drag, tether length, kite performance, and wind shear. The assumption $\beta_{\text{mars}} = \beta_{\text{earth}}$ is assumed to be a good enough approximation. Additionally, the design point C_{L} and $C_{\text{D,eff}}$ comes from maximizing power $\longrightarrow$ maximizing $\frac{C_{\text{L}}^3}{C_{\text{D,eff}}^2}$. The effective drag coefficient can be taken to be:

$$C_{\text{D,eff}} = \underbrace{C_{\text{D,visc}}}_{\text{Kite Viscous } C_D} + \underbrace{\frac{C_{\text{L}}^2}{\pi ARe}}_{\text{Induced Drag}} + \underbrace{C_{\text{d,tether}} \frac{d_T \ell_T}{4A}}_{\text{Effective Tether Drag Penalty}} \tag{3.40}$$

Where d_T is the tether diameter, ℓ_T is the tether length, A is the kite planform area, and $C_{d,tether}$ is the tether cross-sectional drag coefficient. The effective tether drag penalty is correlated to tether forces. Additionally, the tether cross-sectional drag coefficient is probably the same on Mars and Earth.

For a brute-force scaling of everything, $\frac{d_T \ell_T}{4A}$ would be constant $\longrightarrow$ same optimal design point. However, we have seen that $\frac{T_{\text{kite,mars}}}{T_{\text{kite}}} < 1$, so the tether diameter could actually be decreased on Mars despite the kite area increasing. This probably means that it is likely that the effective tether drag penalty for the Mars kite would be significantly smaller than on the Earth kite. This indicates that $\frac{C_L^3}{C_{\text{D,eff}}^2}\Big|_{mars}$ could be somewhat larger than $\frac{C_L^3}{C_{\text{D,eff}}^2}\Big|_{earth}$. To evaluate this better, a more specific analysis should be done.

3.13. Sensitivity Study

Table 3.1 is a summary table of the computed values from the scaling study, where the habitat location Arsia Mons, selected by TU Delft's Rhizome project [57], was considered. Arsia Mons is situated in Tharsis Bugle, southeast of Olympus Mons. Two locations on Arsia Mons were proposed, Arsia South A and B [58]. Since these two locations are located very close to each other, only one location was used for this analysis, namely, Arsia Mons A. This potential habitat is located roughly 9000 meters above Mars's zero elevation point. For reference, this is roughly the same altitude as the peak of Mount Everest [59]. Using the Mars Climate Database, the average density was found to be roughly 0.0065 kg/m^2. This resulted in a density ratio $K_\rho = 0.0054$. The wind speed factor was taken to be 3, assuming that the wind speeds on Mars are on average three times larger than those found on Earth. Wind data evidence from landers Viking 1 indicates that this assumption might be too optimistic. Therefore, a wind speed factor of 2 was also considered in Table 3.2.

Input Parameter	Scaling factor
Wind Speed Scaling	3
Density	0.0054

Output Parameter	Scaling factor
Area	6.8
Tether Force	0.3
K planform	2.6
K thickness	0.1
Mass	0.9
Gravitational Force	0.3
Landing Easiness	1.0
Strain	1
Mach Number	4.2
Reynolds Number	0.1
Turning Capability	9.0
Loop Gravitational Importance	1
Tether Diameter	0.6

Table 3.1: Summary Statistics based on Arsia Mons A and optimistic wind speed scaling factor

Input Parameter	Scaling factor
Wind Speed Scaling	2
Density	0.0054

Output Parameter	Scaling factor
Area	23.1
Tether Force	0.5
K planform	4.8
K thickness	0.1
Mass	2.4
Gravitational Force	0.9
Landing Easiness	0.5
Strain	1.8
Mach Number	2.8
Reynolds Number	0.1
Turning Capability	4.0
Loop Gravitational Importance	1.8
Tether Diameter	0.7

Table 3.2: Summary Statistics based on Arsia Mons A and conservative wind speed scaling factor

It can be seen in Table 3.1 that when considering an optimistic wind speed at Arsia Mons A, the area scaling factor is only 6.8. Such a kite size could be realised, however, low Reynolds flow conditions could result in issues and the turning capability is significantly reduced. Consequently, the Mars kite would have to have more effective control surfaces to achieve the same relative turning radius as the Earth kite. A conservative wind speed factor of 2 represents a more realistic scenario, such as in Table 3.2. When considering a conservative wind speed, the area scaling factor increases to 23.1. Commercial airborne wind energy flexible wing kites, such as those from SkySails, have reached kite sizes as large as 400 m^2. Therefore, an area scaling factor equal to 23.1 does not necessarily mean the concept is unfeasible.

In Table 3.2 the tether force of the Mars kite was reduced by 50% and in Table 3.1 the tether force was reduced to 1/3 of the Earth kite. This also means that the tether diameter can be reduced, which reduces tether weight and tether drag.

Whether the Mars kite will be heavier or lighter than the Earth equivalent is primarily a function of the wind speed scaling factor. A larger wind speed scaling factor, such as 3, results in a Mars kite that is actually lighter than its Earth counterpart. However, a wind speed scaling factor of 2 yields a Mars kite mass of more than twice the Earth kite. The landing easiness is relatively the same on Earth and Mars when considering an optimistic wind speed scaling factor. A conservative wind speed scaling factor results in a landing easiness of less than 1, which means that it would be harder to launch and land the kite on Mars.

The material strain due to gravitational loads is roughly the same on Earth and Mars when an optimistic wind speed scaling factor is considered. A conservative wind speed scaling factor yields a 1.8 times larger gravitational induced material strain on Mars than on Earth. In Table 3.3 Viking 1 surface density and an optimistic wind speed scaling factor of 3 are used. The surface density detected by Viking 1 is taken to be 0.02 kg/m^2. Again, a wind speed factor of 2 was also considered in Table 3.4.

Input Parameter	Scaling factor
Wind Speed Scaling	3
Density	0.0167

Output Parameter	Scaling factor
Area	2.2
Tether Force	0.3
K planform	1.5
K thickness	0.2
Mass	0.5
Gravitational Force	0.2
Landing Easiness	1.8
Strain	0.6
Mach Number	4.2
Reynolds Number	0.1
Turning Capability	9.0
Loop Gravitational Importance	0.6
Tether Diameter	0.6

Table 3.3: Summary Statistics based on Viking 1 lander location and optimistic wind speed scaling factor

Input Parameter	Scaling factor
Wind Speed Scaling	2
Density	0.0167

Output Parameter	Scaling factor
Area	7.5
Tether Force	0.5
K planform	2.7
K thickness	0.2
Mass	1.4
Gravitational Force	0.5
Landing Easiness	1
Strain	1.0
Mach Number	2.8
Reynolds Number	0.1
Turning Capability	4.0
Loop Gravitational Importance	1.0
Tether Diameter	0.7

Table 3.4: Summary Statistics based on Viking 1 lander location and conservative wind speed scaling factor

The atmospheric density at the Viking 1 lander location is about three times larger than at Arsia Mons A. The difference can be seen immediately by looking at the area scaling ratio. Even when considering a conservative wind speed scaling factor of 2, as seen in Table 3.4, the area scaling ratio is only 7.5.

3.14. Scaling Study Conclusion

The scaling study results indicate that it is feasible to operate AWE systems on Mars. However, it is highly dependent on wind resources, as is the case on Earth. Furthermore, the atmospheric density has a large effect on the cross-sectional area required for the kite. It is recommended to investigate alternative habitat locations at lower elevations to leverage higher atmospheric densities. Additionally, the cross-equatorial low-level jet (500 m) present throughout the Martian year at Tharsis Bulge has the highest wind speeds during the northern hemisphere summer and can be leveraged as well [52]. It is also worth mentioning that all of the scaling study indicates a Mars kite will have less turning capability due to a loss of control authority induced by suboptimal environmental conditions. This means the method in which these kites are steered will need to improve significantly, accomplished with kite modifications. The low Reynolds numbers experienced around the kite will be about 10% of that on Earth. Mach numbers on Mars will be as much as four times higher. This might not necessarily cause issues. The thickness of the Mars kite can be as much as ten times thinner than an Earth kite. However, in reality, making a kite with such thin dimensions would probably not be possible. The Mars tether cross-sectional area will likely be smaller so this will allow for a lighter tether that induces less aerodynamic drag.

3.15. Wind Turbine Case

All the elements for the corresponding analysis of the wind turbine-on-mars are exactly the same as the proceeding kite analysis, so all conclusions will actually hold for that case too.

4

Analysis of Martian Wind Resource

In order to adequately design a wind energy system that can meet the power requirements for a Martian habitat, the wind resource must be assessed. The following section describes the Mars Climate Database (MCD), which is used to predict meteorological conditions throughout the Martian year anywhere on the surface. The purpose of this section is to establish a road map from Martian global coordinates to wind resource characterisation.

The best reference detailing the state-of-the-art wind data on Mars from a wind energy perspective is [17]. However, all of the available wind data is above the operational altitude of an airborne wind energy system. Therefore, this thesis resorted to using the Mars Climate Database. The wind resource is strongly linked to the selection of the habitat location. However, the site selection has additional requirements, such as the existence of smaller lava tubes, the presence of water ice, and the lowest possible altitude in order to increase the atmosphere density which is needed for aerodynamic braking during Martian atmospheric reentry. Additionally, a higher atmosphere density results in higher power generation.

4.1. Mars Climate Database

The diurnal and seasonal cycles, combined with an extreme and diversified topography, make the red planet's climate quite variable in space and time, says [53]. Using the MCD these variations can be modelled and predicted. As explained by [60], the MCD is a database of meteorological fields derived from General Circulation Model (GCM) numerical simulations of the Martian atmosphere and validated using available observational data. The GCM uses a coarse grid with a spatial resolution of 332.7 by 221.8 km. Put another way, the grid has steps of $5.625°$in longitude and $3.75°$in latitude.

[60] details how the MCD is able to produce a higher fidelity model through the use of post-processing tools, such as a gravity model, high resolution (32 pixels/degree) topography data sets produced by the Mars Orbiter Laser Altimeter (MOLA) team, and the smoothed Viking Lander 1 pressure records with the MCD surface pressure in order to compute surface pressure as accurately as possible. These surface pressures can then be used to reconstruct vertical pressure levels and hence, within the restrictions of the procedure, yield high-resolution values of atmospheric variables such as density and wind speeds. The MOLA data has a much higher resolution of 32 pixels per degree, which results in an 1850-meter resolution at the equator where the grid is the largest.

The MCD allows the modelling of various conditions, such as the solar maximum, average, and minimum. Furthermore, these conditions can be combined with average climatological conditions and planetary-wide dust storm conditions. Additionally, the model allows the simulation of dusty conditions with solar maximum and low dust conditions. There is also an option to simulate specific conditions of certain years.

The solar conditions of any certain day can be known in advance since the solar activity has a

certain periodicity, namely, an 11-year magnetic cycle that influences the intensity of the solar radiation. Since the wind cycle on Mars is primarily driven by the Sun's solar radiation, this periodicity will be useful to predict wind conditions and, thus, the power output throughout the year. During the design phase, it is critical to consider both the maximum and minimum conditions so as to produce sufficient power on average throughout the year.

4.2. Mars Climate Database Use Cases & Limitations

The MCD is a very useful tool for investigating the wind resource on Mars, but it does have its limitations. For instance, the vertical grid has 49 non-linear data points, where the closest point to the ground is approximately 5 m above the surface and the highest at around 250 km altitude. The grid spacing is non-linear, therefore, the distance between vertical stations increases as a function of altitude. Consequently, only five grid points are present within the first 400 m of the atmosphere, which coincides with the altitude AWE system usually fly in.

Linear interpolation is utilised in order to compute atmospheric data between these grid points. However, this also ensures that the maximum and minimum values generated in the model will not be reflected in the database output. Therefore, [53] expresses caution in using the MCD to estimate extreme values, such as diurnal ranges or spatial maxima and minima. For these same reasons, the database may appear to underestimate rapid rates of change in variables with space or time. The interpolation method is only useful within the limits of the grid lines. Therefore, only wind data above an altitude of 5 m will be used for the purposes of this investigation.

As mentioned in [53], the Mars Climate Database is formed by averaging model output over twelve times of year (periods of 50-60 days) at twelve fixed times of day and is stored on a three-dimensional spatial grid which is sampled from the models, but which may not reflect their full resolution in any one dimension. This averaged data cannot, therefore, represent the full range of variability in the models themselves.

4.3. Update Habitat Location

The next step is to reevaluate the decision on the location of the habitat by the previous design team [14]. Their chosen location was Protonilus Mensae and chosen because NASA concluded the location has potentially been habitable in the past, has potential for present habitability, and might have water ice closer than 3 meters from the surface. The main motivation for choosing a new habitat location was due to the Rhizome project deciding to utilise lava tubes as habitats instead of excavating cavernous habitats. The main constraint was a maximum lava tube diameter of 30 m. Two locations were found to fit this requirement [58]. Namely, Arsia North and Arsia South A. Arsia South A is located at a $-14.377°$ N longitude and $240.051°$ E latitude. Arsia North is located at a $-3.062°$ N longitude and $236.07°$ E latitude. The location with the highest power density will be chosen. Thus, Table 4.1 compares the average wind speed and atmospheric density of the site computed by the MCD.

	Arsia North	Arsia South A
Mean Wind Speed [m/s]	20.359	17.343
Average Atmospheric Density [kg/m^3]	0.01	0.007

Table 4.1: Comparison between habitat locations - Arsia North and Arsia South A

Both the average wind speed and average atmospheric density are higher at Arsia North. Therefore, Arsia North is chosen as the final habitat location.

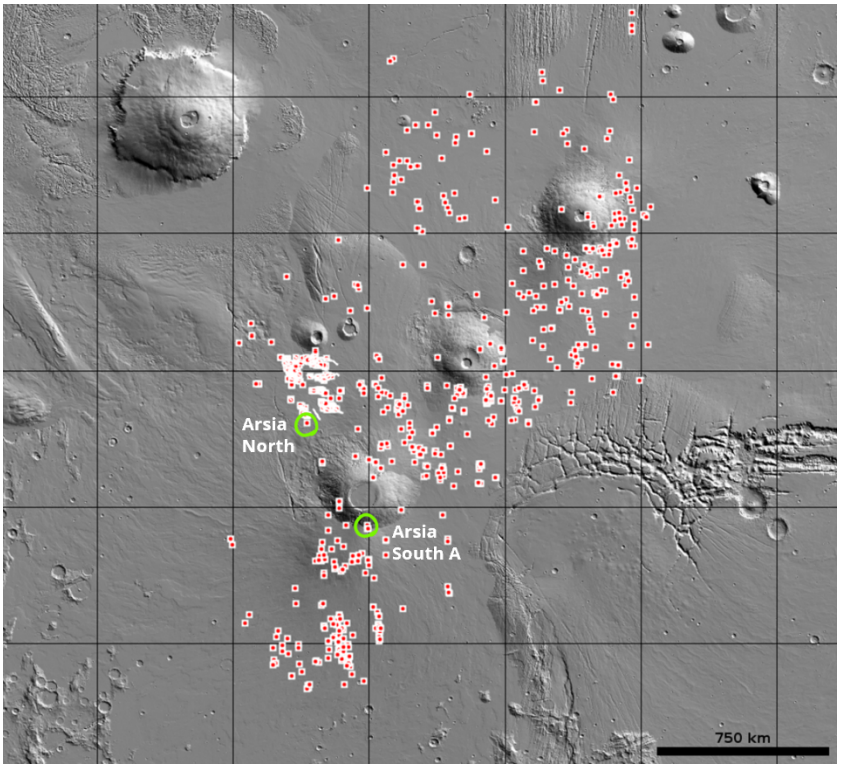

Figure 4.1: Location of candidate lava caves on the Tharsis bulge [2]. The cave on Arsia North at -3.062° N, 236.07° E, highlighted by the green circle, was selected as a compromise between lower altitude (= higher density) and reasonable wind speeds.

4.4. Mars Climate Database Results for the Operation Site

This section provides the results for Arsia North for various seasons and weather scenarios. In subsection 4.4.1 the wind profile of a few days in every season is shown, in subsection 4.4.2 the average wind speeds per season are shown and in Figure 4.4.2 a probability distribution of every season is shown.

4.4.1. Daily Wind Velocity Profile

In this section, a seasonal comparison was done for the Arsia North location in order to demonstrate how wind speeds can change throughout the Martian year. The wind velocity was plotted against altitude and the local time of day. This was done at 12 different solar longitudes, for every $30°$, in order to get a feeling of how the wind speeds change over the Martian year. The solar longitude is an indication of where Mars is in its orbit around the sun. These plots can be seen in $0°$, $90°$, $180°$ and $270°$ which are the equinox of martian spring, summer, autumn, and winter in the northern hemisphere, respectively. The plot for $360°$ was omitted since it is the same plot as $0°$, as it is the same time of year.

This comparison only represents twelve particular days out of the Martian year, therefore, reality might tell a different story. Nevertheless, these temporal wind velocity profiles give an indication of when and where the highest wind speeds are typically experienced throughout the day. Furthermore, comparing the seasons also indicates whether these periods of high wind speeds shift in time as the seasons change.

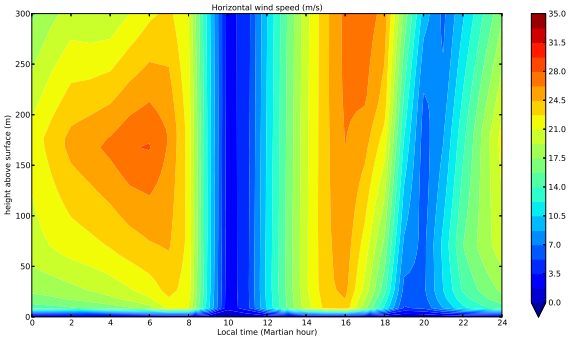

Figure 4.2: Wind velocity profile of Arsia North in Spring equinox

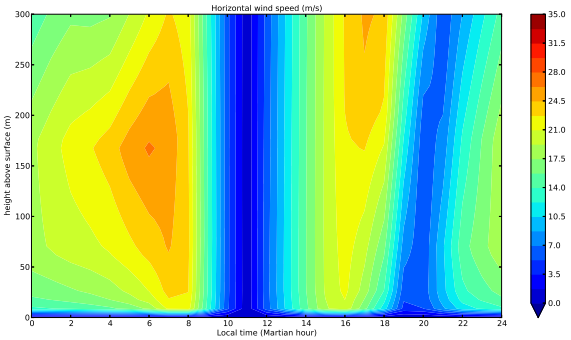

Figure 4.3: Wind velocity profile of Arsia North in late Spring

There are two periods throughout the year when wind speeds are near zero. The first period occurs from 9:00 to 12:00 and the second period is roughly around 18:00 to 22:00. It is worth noting that the wind speed in these periods continues to be near zero irrespective of the elevation. The kite will not be able to fly during these times of the day.

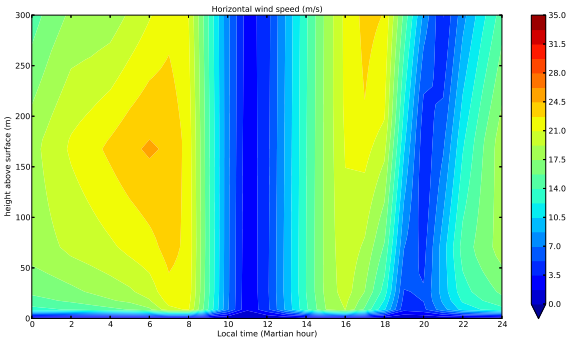

Figure 4.4: Wind velocity profile of Arsia North in early Summer

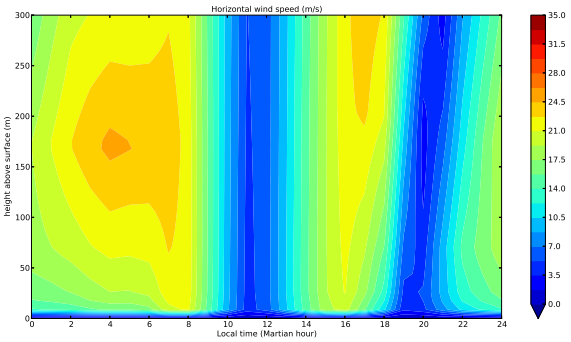

Figure 4.5: Wind velocity profile of Arsia North in Summer equinox

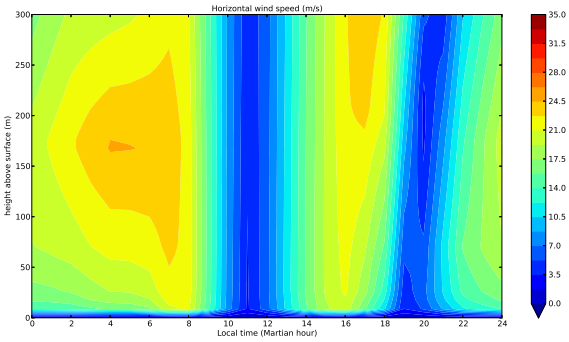

Figure 4.6: Wind velocity profile of Arsia North in late Summer

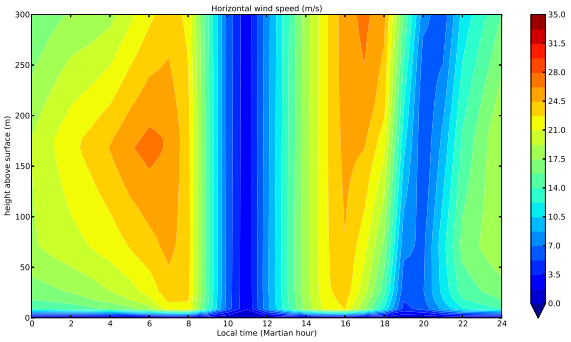

Figure 4.7: Wind velocity profile of Arsia North in early Autumn

The wind velocity profiles indicate that high wind speeds consistently occur in the morning (0:00-8:00) and afternoon (12:00-18:00) throughout the Martian year. The highest wind speeds most often occur in the afternoon, in late Autumn, and the highest wind speeds occur throughout the night, shown in Figure 4.9.

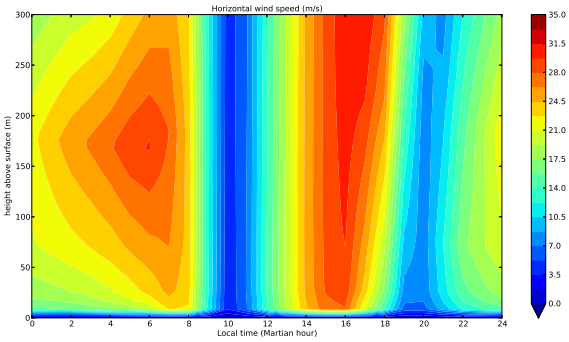

Figure 4.8: Wind velocity profile of Arsia North in Autumn equinox

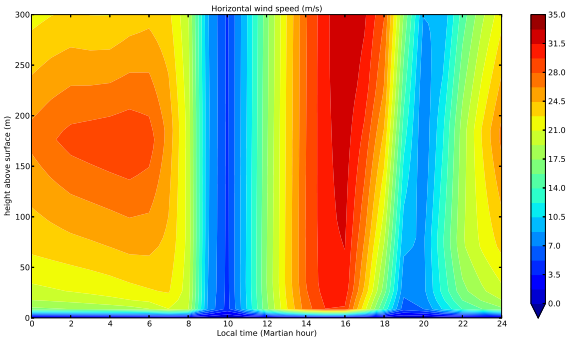

Figure 4.9: Wind velocity profile of Arsia North in late Autumn

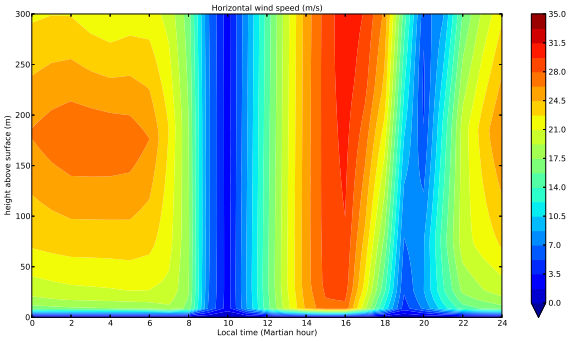

Figure 4.10: Wind velocity profile of Arsia North in early Winter

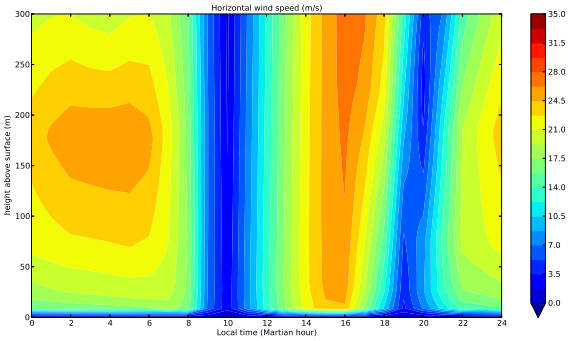

Figure 4.11: Wind velocity profile of Arsia North in Winter equinox

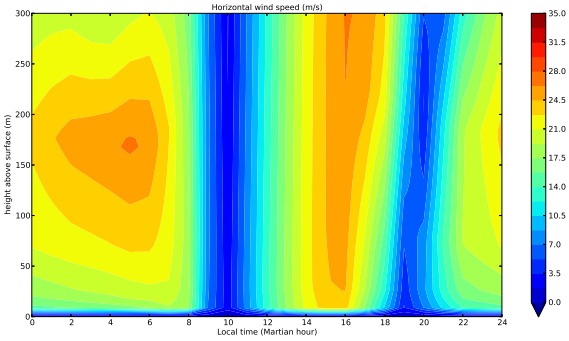

Figure 4.12: Wind velocity profile of Arsia North in late Winter

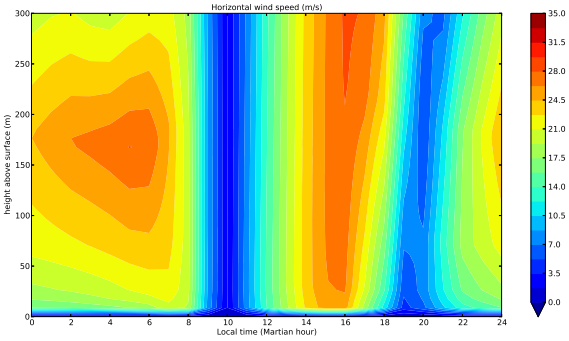

Figure 4.13: Wind velocity profile of Arsia North in early Spring

The vertical wind profiles plotted have a data point in altitude every 5 meters and a data point in time for every hour, for a total of 1500 data points per graph. From the graphs, it can be seen that throughout the year there are periods in the day where the wind speed is significantly lower for all altitudes than the rest of the day. Furthermore, it can be noted that this happens at almost the same time on all days. Usually, in summer the wind speeds are significantly worse, however, in this location, that is not the case. This is thought to occur due to a low altitude (500 m) cross-equatorial jet that can form during the northern hemisphere summer along the eastern flank of the Tharsis bulge [51].

To get a better idea of how the wind speed changes with altitude, vertical wind velocity profiles are made. These are shown to indicate some interesting points in time that might not be completely clear when looking at the daily wind velocity profiles shown previously.

In general, the wind velocity increases with increasing altitude, as seen in ideal log wind profiles. However, Figure 4.14 shows a wind velocity profile where wind speeds reduce after a certain altitude or the wind speed remains constant irrespective of altitude.

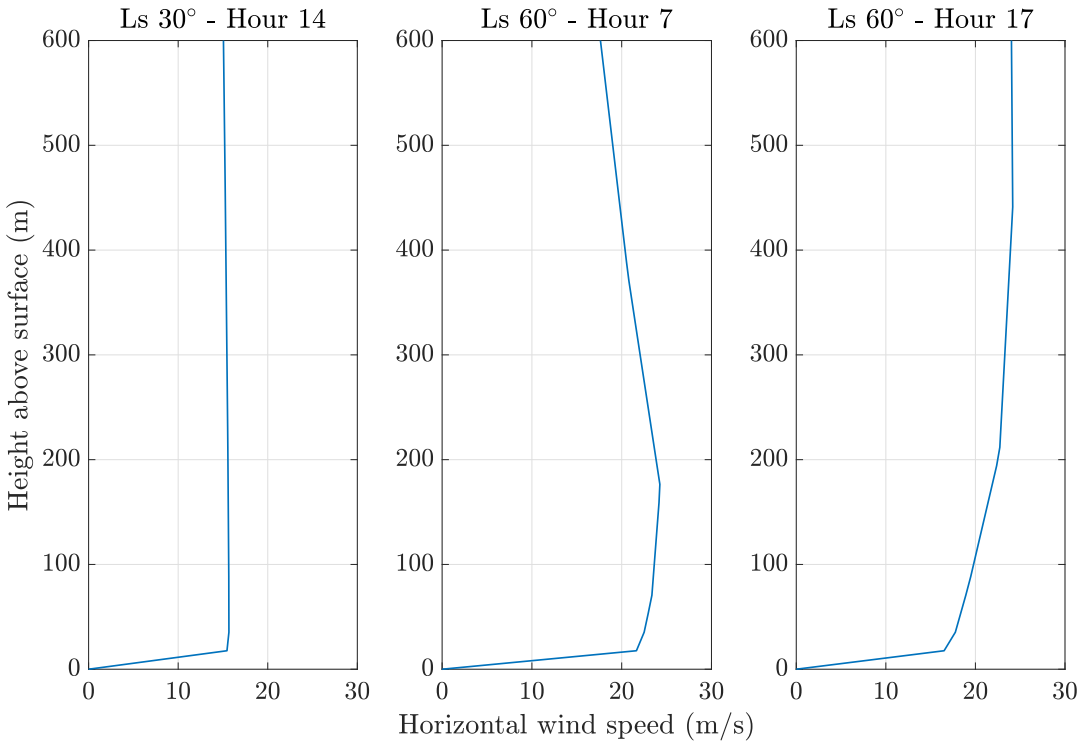

Figure 4.14: Wind speed vs height at Arsia North

4.4.2. Average Wind Speeds

For the sake of comparison, the average wind speeds are plotted for 8 periods, late spring(0-45), early summer(45-90), late summer(90-135), early autumn(135-180), late autumn(180-215), early winter(215-270), late winter(270-315) and early spring(315-360). The data for these periods are plotted for five different altitudes about the surface, 5, 105, 205, 305, and 405 meters. The results can be seen in Figure 4.15, 4.16, 4.17, 4.18 and 4.19. Figure 4.20 is included so as to better compare the average wind speeds at different altitudes. In order to calculate the average wind speed for 45 days in the season, average wind speeds are taken at every hour of the day and at the desired altitude, and then this was averaged over the season. This work provides insight into diurnal wind speed changes.

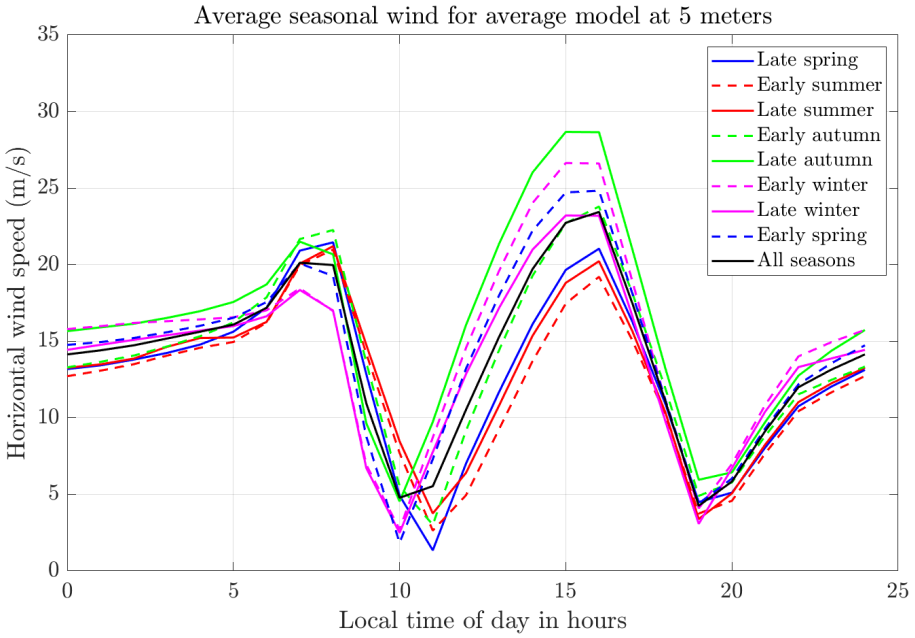

Figure 4.15: Average daily wind speeds at 5-meter altitude

Figure 4.15 indicate that the highest wind speeds occur during the day and are strongest during autumn and winter. It was previously assumed that wind speeds at night were too low for the kite to fly. However, if a cut-in wind speed of 9 m/s is assumed, a kite could indeed fly at night on Mars. This is consistent with the diurnal variations found in literature [52].

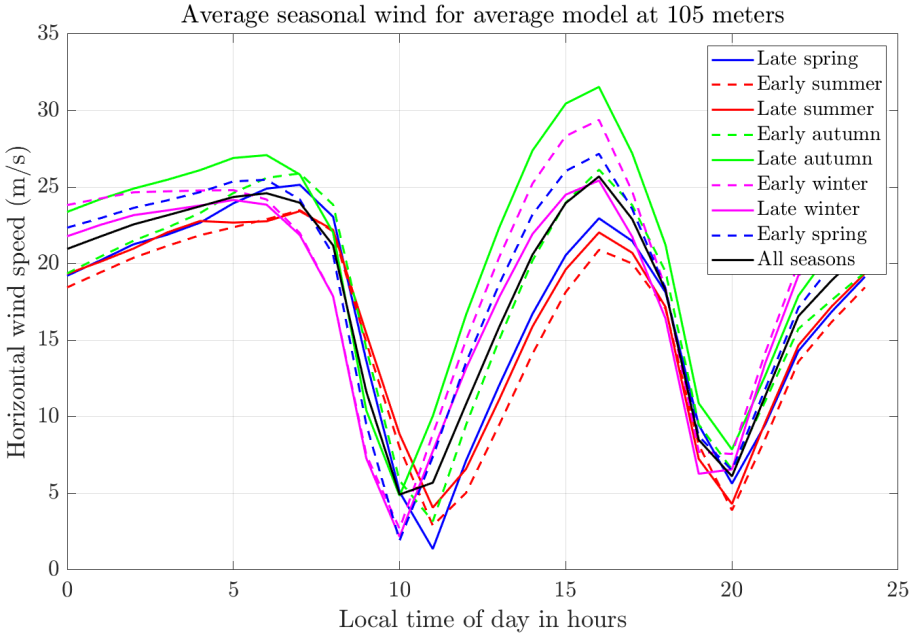

Figure 4.16: Average daily wind speeds at 105-meter altitude

Figure 4.16 and 4.17 indicate that a kite will not be able to perform a pumping cycle during two short periods, as indicated by the two sharp drops in wind speed.

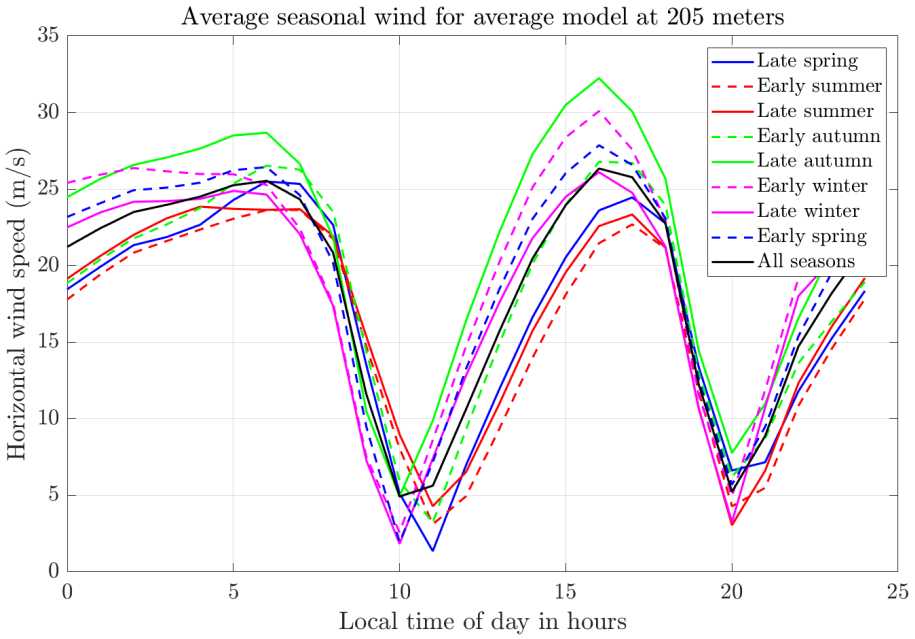

Figure 4.17: Average daily wind speeds at 205-meter altitude

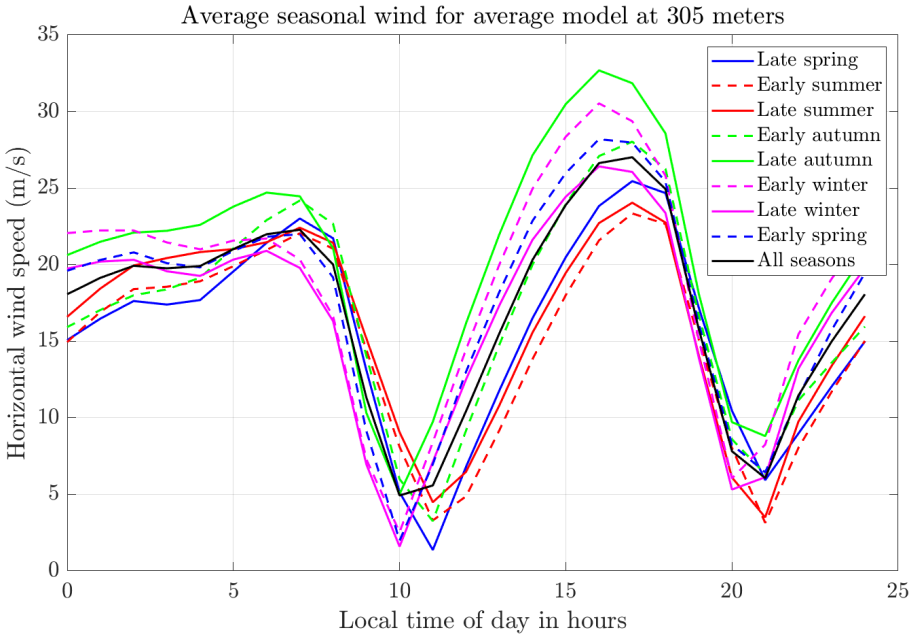

Figure 4.18: Average daily wind speeds at 305-meter altitude

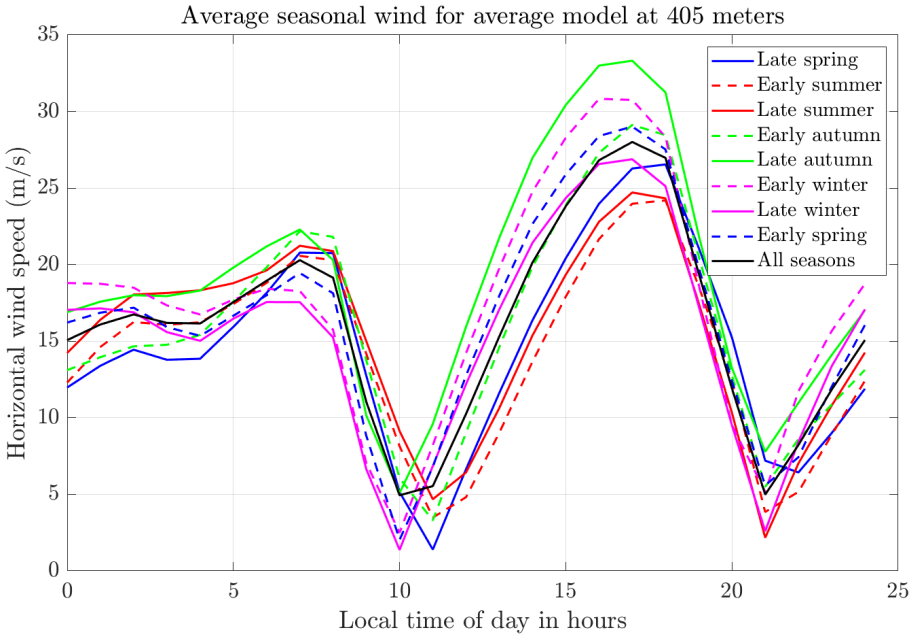

Figure 4.19: Average daily wind speeds at 405-meter altitude

Figure 4.20 indicates that in the morning the best wind resource is found at 200 meters altitude. During noon, all wind speeds above 5 meters are roughly the same, and the highest wind speeds occur at the highest elevations during the evening.

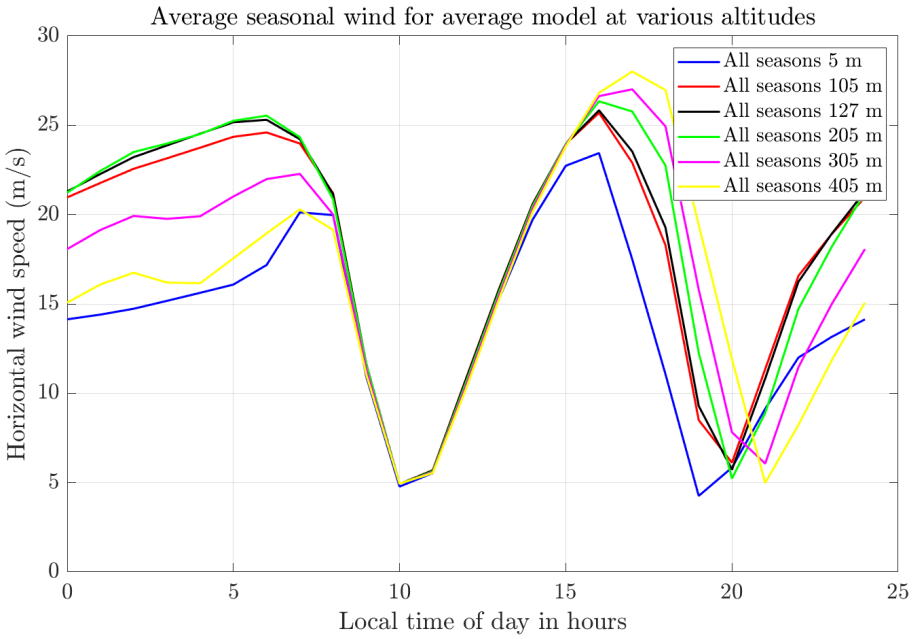

Figure 4.20: Average daily wind speeds at various altitudes

We know the average wind speed for every season, at each hour of the day at 5, 105, 205, 305, and 405 meters. Using these averaged velocities, a fourth-order polynomial equation can be fitted to average velocities at 5 different altitude points for each season, which can be used as seasonal vertical wind velocity profiles. These polynomial functions ”vertical wind profiles” can be used to predict wind speeds at any altitude between 5-405 meters for every season, as seen in Figure 4.21. Note that the plot does not consider altitudes below 5 m or above 405 m. The initial condition [x,y] = [0,0] intercept

was not considered when constructing the polynomial fitted curves. The shape of these vertical wind profiles is coherent with those found in low-level atmospheric jets [52] [61].

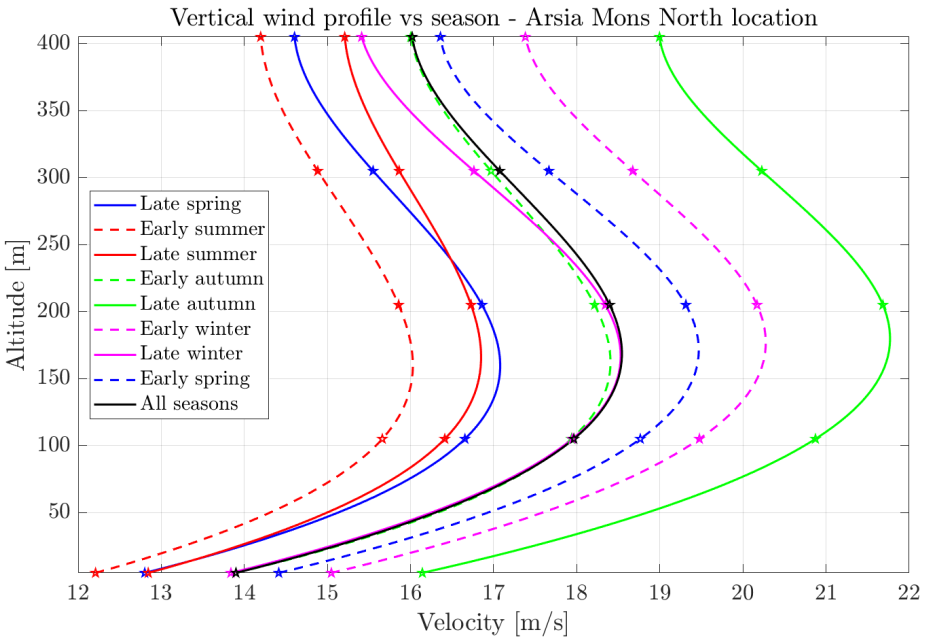

Figure 4.21: Vertical Average Wind Speeds vs Height vs Seasons

Figure 4.21 indicates that the highest average wind speeds are not encountered at the highest elevation, but instead somewhere between an altitude of 150 and 175 meters.

Wind Speed Probability Density

The collected data is further examined through the construction of the Weibull probability density function (PDF) for various altitudes and solar longitudes. This data representation is relevant not only for a better understanding of the wind resource patterns but is also an input for the performance model of the pumping kite system described in the next chapter 6. As the kite power output is heavily dependent on wind speeds, the likelihood of various velocities to be present at a set time and place must be known. The distribution of the wind speed for a given time period can be expressed using the Weibull distribution function, where v_m is the scaling parameter and *k* is the shape parameter. Using the *"fitdist(dataset,'Weibull')"* function in Matlab yields the scaling and shape parameters for every seasonal dataset.

$$g_w\left(v_w\right) = \frac{k}{v_m}\left(\frac{v_w}{v_m}\right)^{k-1} e^{-\left(\frac{v_w}{v_m}\right)^k} \tag{4.1}$$

In Figure 4.22, 4.23, 4.24, 4.25 and 4.26 the Weibull PDFs of the wind speeds can be seen for multiple seasons at five different altitudes above the surface, 5, 105, 205, 305, and 405 meters. Figure 4.27 is included so as to better compare the Weibull PDFs of annual average wind speeds at the five altitudes, as previously mentioned. The data for these graphs is the same data used to create the averages in subsection 4.4.2, so every half a season is represented by 45 Martian days (actually 45 degrees of solar longitude), consisting of 25 data points in time and 25 data points in solar longitude, which gives every seasonal Weibull probability density function a total of 625 velocity data points. The "all seasons" PDF is a combination of all seasons, which contains a total of 5000 velocity data points.

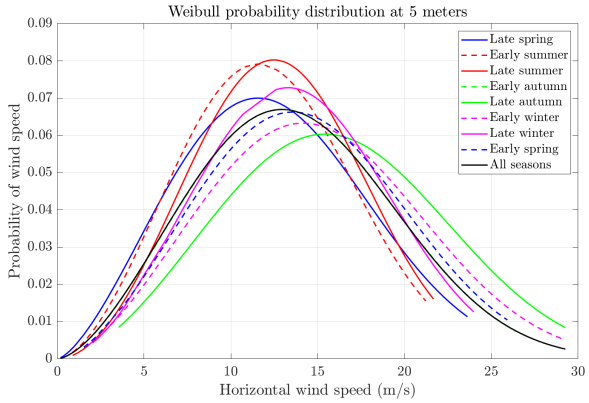

Figure 4.22: Probability density of wind speeds for different seasons at 5 m altitude

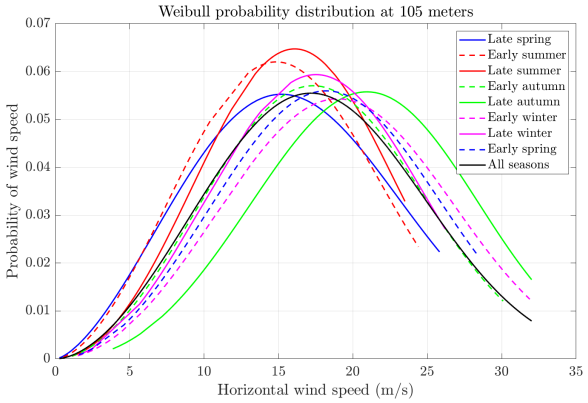

Figure 4.23: Probability density of wind speeds for different seasons at 105 m altitude

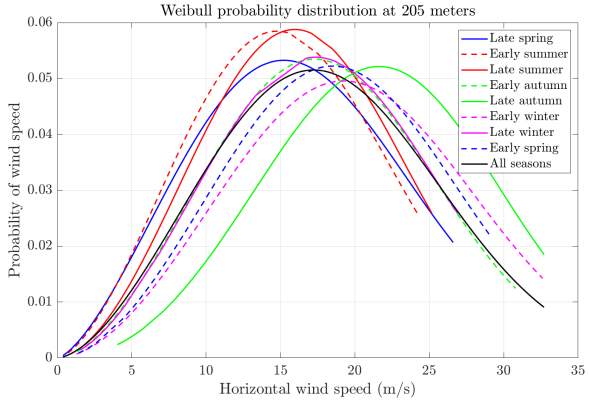

Figure 4.24: Probability density of wind speeds for different seasons at 205 m altitude

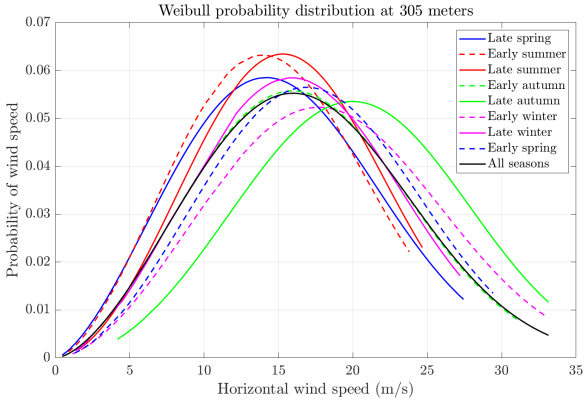

Figure 4.25: Probability density of wind speeds for different seasons at 305 m altitude

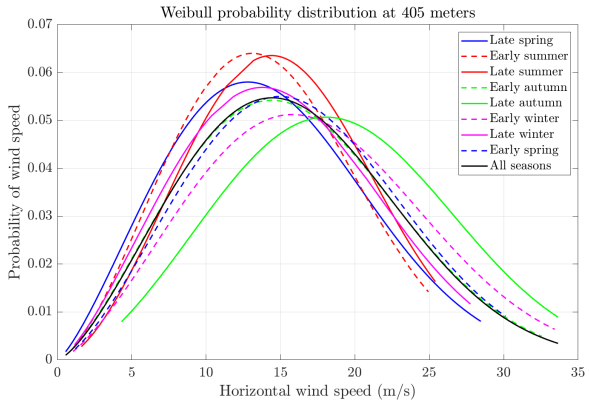

Figure 4.26: Probability density of wind speeds for different seasons at 405 m altitude

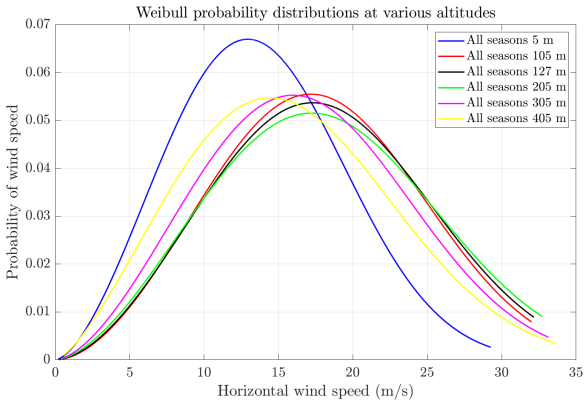

Figure 4.27: Probability density of wind speeds for different seasons at various altitudes

The average height of the traction phase called ”pattern height”, was computed to be 127 meters. Thus the wind speed data was also collected at pattern height. The scale coefficient (average wind speeds) and the shape coefficient of every part of the year are shown in Table 4.2.

	Scale (m/s)	Shape
Late Spring	18.754	2.495
Early Summer	17.726	2.668
Late Summer	18.573	2.941
Early Autumn	20.280	2.847
Late Autumn	23.691	3.314
Early Winter	22.067	2.952
Late Winter	20.270	2.950
Early Spring	21.261	2.913

Table 4.2: Probability density function parameters computed from MCD wind speed data

4.4.3. Atmospheric density

Figure 4.28 shows how the average atmospheric density changes over the year. The atmospheric density can vary as much as 20%. The density appears to decrease in the summer and autumn. The local temperature will increase during the summer, which will cause the atmosphere to become less dense.

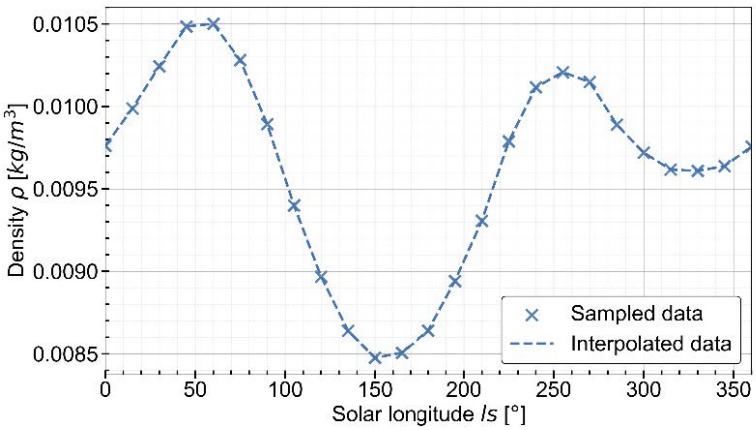

Figure 4.28: Average sol density for a Martian year at Arsia North. Evaluated from the MCD [53]

4.4.4. Solar Flux

The hourly averaged solar flux to the surface throughout the year is shown in Figure 4.29. Solar flux is nonzero from 07:00 to 16. The daily maximum solar flux occurs at 12:00 and is as high as 627 Q/m^2. This is the same time that wind speeds drop rapidly.

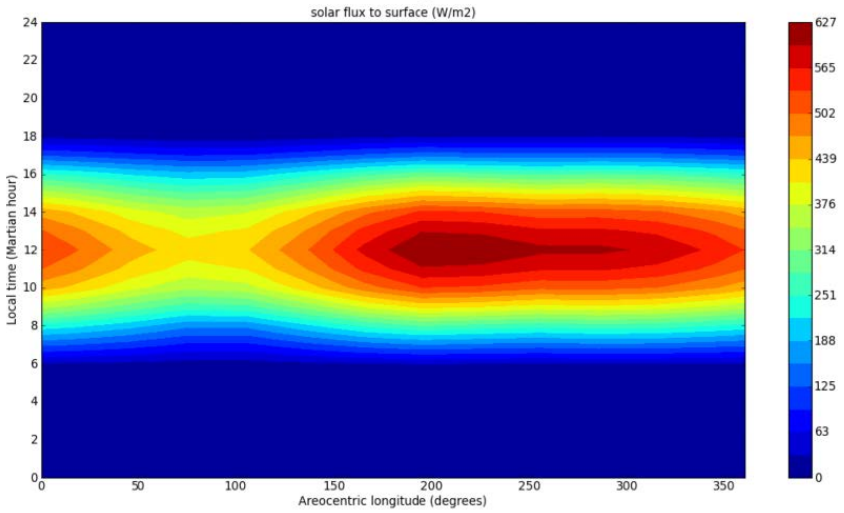

Figure 4.29: Solar flux to surface at Arsia North with solar longitude and local Martian time. Evaluated from the MCD [53]

4.4.5. Influence on the Subsystems and Operations

These results lead to a few considerations for subsystem design; the most important parameters for operation are, wind speed to be able to fly, cut-out speed, and maximum wind speed. From the data presented in this chapter, a number of important parameters can be seen. First is the portion of time that the wing cannot produce due to too little wind or too high wind. At very low wind speeds, the wing will not produce enough lift to produce a meaningful resultant force while at too high speeds, the aerodynamic force will exceed the maximum force that can be sustained by the structure and tether. Additionally, in subsection 4.4.1 it became apparent that especially during spring and winter the wind speeds are relatively low, which means that during the other seasons this deficit needs to be accounted for. This results in the need for high power generation during the seasons when the wind is abundant thus resulting in a high peak power generation.

Furthermore, in subsection 4.4.1 it became clear that during almost every season there are periods of time where the wing most likely won't be able to fly due to the insufficient wind speeds. Thus at these times, the kite needs to land. With this many landing and launching operations, a robust landing and launching system must be created. Furthermore, the most power will be generated during periods of very high wind speeds, to make optimal use of these high wind speeds, the system must be able to withstand high aerodynamic loads which leads to a robust structure made of materials with a high strength to weight ratio.

4.4.6. Verification of Data Acquisition

The data in the MCD is acquired from Fortran subroutines, these subroutines are called in a separate file which creates a text file with the desired outputs. The desired outputs, in this case, are solar longitude, local time of day, altitude, and horizontal wind speeds. One text file is created for each season at each particular altitude. Here we consider 5 altitudes and 8 seasons, which results in 40 different text files. Each text file contains 25 data points for time and 25 data points for solar longitude, which results in 625 velocity data points per text file and 5000 velocity data points for the entire year. This same data was used for both subsection 4.4.2 and Figure 4.4.2. This data can also be used for the performance model where the data for an entire year is used to determine the yearly power production.

Thus to check whether the database got the right output, the only thing that needs to be checked is whether or not the text files have the right amount of velocity data points at the correct solar longitude and altitude. The data file needs to consist of $25 \cdot 25 = 625$ velocity points, and have the correct solar longitude and altitude values. These parameters were periodically evaluated and found to be correct.

4.4.7. Sensitivity Analysis

The data produced by the MCD is generated using a seed to determine the random numbers necessary for the creation of large and small-scale variabilities. For this analysis, only one seed was used to generate the data. This can have several implications. The fact that random numbers are generated might lead to a result that lies either on the low end or the high end of the possible outcomes. It is also possible that these small-scale variabilities only have a marginal impact when looking at large amounts of data such as on a yearly scale, but this has not been investigated. Even so, these small impacts in terms of wind speed, density, and temperature could impact the performance of the system. As a recommendation for future endeavours, it is recommended to extend the amount of data gathered from the MCD by taking data for multiple years by changing the seed used for the random number generation.

5

System Characteristics

5.1. Scaling study results

In this section, the scaling methodology proposed in chapter 3 is used to scale Kitepower's V3 kite parameters [62]. An average atmospheric density of 0.01 kg/m^3 is used. A wind speed scaling factor 2 and 2.29 was used to compute the scaling factors needed to design a Mars kite. Notably, the planform area will need to be approximately 10 - 15 times larger than the V3 kite. However, the tether force is only half of what would be used on Earth. This means that the kite membrane can be relatively thinner to withstand the aerodynamic forces needed to produce an equivalent amount of power. A landing easiness of less than 1 means that it would be harder to launch and land the kite on Mars. A turning capability is greater than 1 which means that the Mars kite would have to have more effective control surfaces to achieve the same relative turning radius as the Earth kite.

Input Parameter	Scaling factor
Wind Speed Scaling	2
Density	0.010

Scaling Parameter	Scaling factor
Area	15
Tether Force	0.5
K planform	3.9
K thickness	0.1
Mass	1.9
Gravitational Force	0.7
Landing Easiness	0.7
Strain	1.5
Mach Number	2.8
Reynolds Number	0.1
Turning Capability	4.0
Gravitational Importance on turning	1.5
Tether Diameter	0.7

Table 5.1: Summary Statistics based on Arsia North and a wind speed factor of 2

Input Parameter	Scaling factor
Wind Speed Scaling	2.29
Density	0.010

Scaling Parameter	Scaling factor
Area	10
Tether Force	0.4
K planform	3.2
K thickness	0.1
Mass	1.4
Gravitational Force	0.5
Landing Easiness	0.8
Strain	1.2
Mach Number	3.2
Reynolds Number	0.1
Turning Capability	5.2
Gravitational Importance on turning	1.2
Tether Diameter	0.7

Table 5.2: Summary Statistics based on Arsia North and a wind speed factor of 2.29

5.2. Design Selection

A rigid or semi-rigid wing design implies the presence of both rigid and foldable elements in the wing. As the new pumping kite has an area of 200 m^2 the dimensions of the rigid elements would be way greater than previously anticipated which is not in line with the package design. Therefore, a leading-edge inflatable kite is sized for this system.

5.3. Aerodynamic Characteristics

The following is the design for Kitepower's V3 20-kW demonstrator kite. The generator has a nominal power of 18 kW and produces an average electrical power of about 7 kW in good wind conditions [63]. This power is sufficient for about 7 Dutch households [14]. The sizing and performance of the kite power system are evaluated using two performance models [47] and [48].

Kitepower's V3 kite area is 19.75 m^2. Assuming a wind speed scaling factor equal to 2, the Mars kite planform area would have to be 15 times larger than the V3 kite and the kite mass would be 1.9 times larger, seen in Table 5.3. If a wind speed scaling factor of 2.29 is assumed, the area scales with a factor of 10 and the kite mass scales with a factor of 1.38, as seen on Table 5.4. Lastly, if a wind speed scaling factor of 2.52 is assumed, the area scales with a factor of 7.5 and the kite mass scales with a factor of 1.087, as seen on Table 5.5.

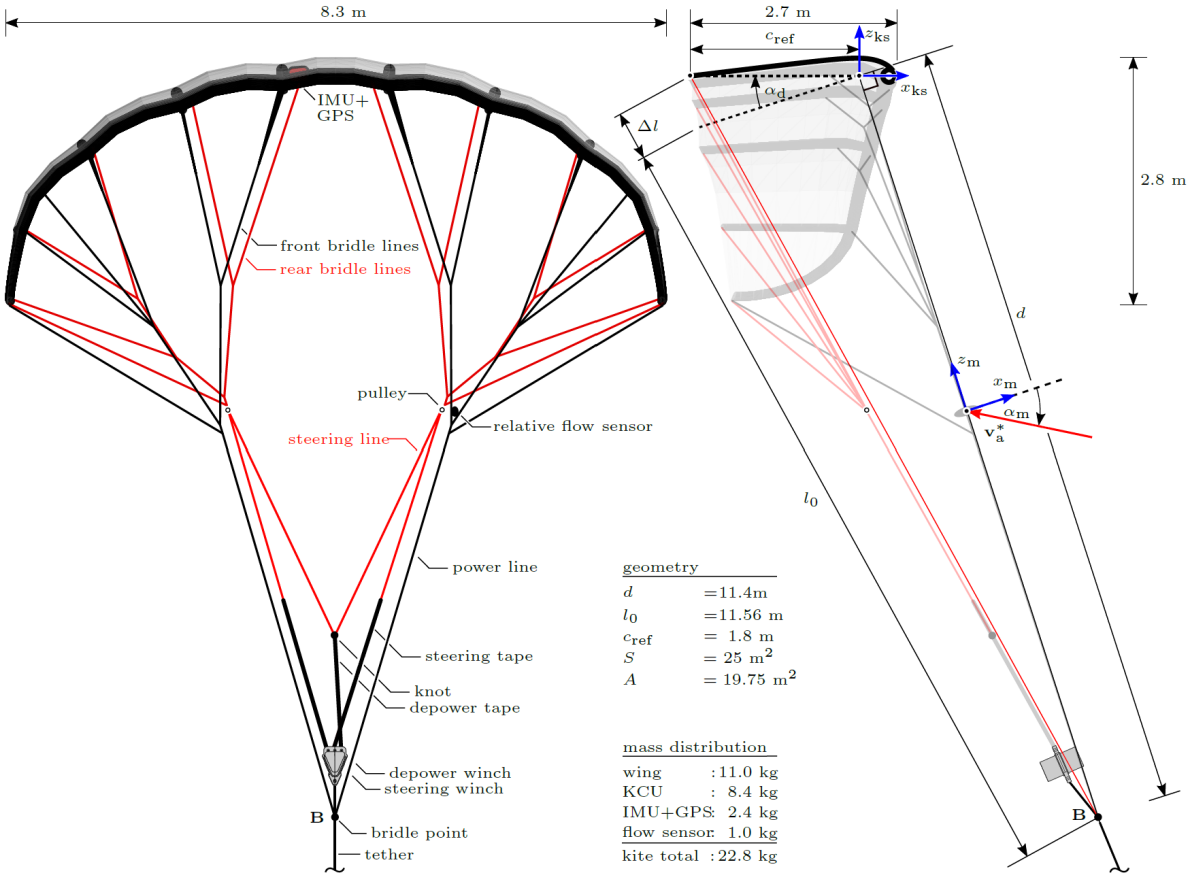

Figure 5.1: Kitepower's V3 kite design [62]

Parameter	Scaling Factor [-]	V3 Kite	Mars Kite
Area [m^2]	15	19.75	296.25
Kite Mass [kg]	1.936	22.8	44.14
Tether Diameter [mm]	0.707	10	7.07

Table 5.3: Scaling results for 300 m^2 Mars kite

Parameter	Scaling Factor [-]	V3 Kite	Mars Kite
Area [m^2]	10	19.75	197.5
Kite Mass [kg]	1.38	22.8	31.46
Tether Diameter [mm]	0.661	10	6.6

Table 5.4: Scaling results for 200 m^2 Mars kite

Parameter	Scaling Factor [-]	V3 Kite	Mars Kite
Area [m^2]	7.5	19.75	148.13
Kite Mass [kg]	1.087	22.8	24.78
Tether Diameter [mm]	0.630	10	6.3

Table 5.5: Scaling results for 150 m^2 Mars kite

5.3.1. Aerodynamics Performance Coefficients and Tether Parameters

The following aerodynamic coefficients and tether inputs will be used in order to compare the different versions of the performance models.

Originally, the 300 m^2 kite was computed by the scaling study, however, using two kites was deemed a necessity in order to increase the reliability of the system. Thus, using two 150 m^2 was considered. Then after running a time series QSM mass simulation on a 150 m^2 kite, explained later in chapter 6, the cut-in wind speed was found to have increased from 9 m/s to 15 m/s. This reduces the energy production of the AWE system during periods of the year with relatively lower average wind speeds, such as in the late summer when the average wind speed is 18.75 m/s. Therefore, in order to compensate for this, a 200 m^2 kite is considered. In theory, this will overproduce energy so a larger portion of the energy can be diverged to supply energy to the short-term energy storage.

The simulation inputs in Table 5.6 and Table 5.7 are used for comparing the Luchsinger model, the simplified QSM, and the time series QSM. These values were gathered from [62], except for the tuned kite drag coefficient. Instead, a lift-to-drag ratio of 5 and 1 was used during the reel-out and reel-in phases, respectively.

Note that only the Luchsinger and simplified QSM implement a reel-in elevation angle, while the time series QSM does not. Additionally, attempts were made to incorporate power limits in the time series QSM but were not successful. Nevertheless, the power limit is reached at wind speeds higher than those observed at Arsia North.

	Reel-out	Reel-in
$C_{L,\,ref}$	0.71	0.39
C_D	0.142	0.39
$C_{D,\,tether}$	1.1	1.1
L/D	5	1
Elevation	25°	60°
Azimuth	0°	0°
Course	90°	180°

Table 5.6: Aerodynamic values used as inputs for the Luchsinger and QSM simulations

Kite Area [m^2]	200
Kite Weight [kg]	31.5
Power Limit [kW]	84
Tether force	
- min.	0.1 kN
- max.	5.1 kN
Tether length	
- min.	200 m
- max.	400 m
Tether Density	724 kg/m^3

Table 5.7: Power limits and tether values used as inputs for the Luchsinger and QSM simulations

Table 5.8 and Table 5.9 are used as model input when trying to match power curves with experimental data and when validating the scaling methodology in sections section 7.2 and section 7.3 respectively. These values were gathered from [62].

	Reel-out	Reel-in
$C_{\text{L, ref}}$	0.71	0.39
$C_{\text{D, tuned}}$	0.18	0.12
$C_{\text{D, tether}}$	1.1	1.1
Elevation	25°	
Azimuth	0°	0°
Course	90°	180°

Table 5.8: Aerodynamic values used as inputs for comparing the models with experimental data and validating the scaling model

Kite Area [m^2]	300
Kite Weight [kg]	44.14
Power Limit [kW]	$-$
Tether force	
- min.	0.1 kN
- max.	7.2 kN
Tether length	
- min.	200 m
- max.	400 m
Tether Density	724 kg/m^3

Table 5.9: Power limits and tether values used as inputs for comparing the models with experimental data and validating the scaling model

5.3.2. Airfoil Choice

The V3 kite airfoil can not be modified because the airfoil is essentially a cylindrical leading edge with a thin membrane across the top side of the kite. However, future work should investigate using a ram-air kite, which can tailor its airfoil shape. The effect of low Reynolds numbers is not within the scope of this thesis.

6

Performance Analysis Models

6.1. Power Performance

The kite sizing greatly depends on the habitat location and the corresponding in situ wind resource. Nevertheless, as the purpose of the kite system is to power a habitat, the expected daily power demand patterns are a leading factor in the engineering process of the renewable energy system. While the power demand requirements are extremely mission-specific, the pumping cycle kite power sizing analysis remains unchanged.

In the following section, a short description of the system's operations and architecture is presented. Next, the theoretical model to optimise kite performance is discussed. Lastly, the system sizing process and results to meet the 10 kW power demand at the Arsia North is presented.

6.1.1. System operations and architecture

The operational principle of a pumping kite is visualised below in Figure 6.1 where the idealised flight trajectory in a wind reference frame is visualised. In general, the pumping cycle of a kite can be divided into three distinctive operational phases as depicted; first, from t_0 to t_A is the retraction phase for which a subscript in is used in the below analysis. Next, from t_A to t_B is the transition phase of the cycle after which the traction phase takes place from t_B to t_C. The traction phase is denoted as out and the transition phase is denoted as $trans$ is the analysis below. β is the elevation angle, which is the angle between the ground and the tether.

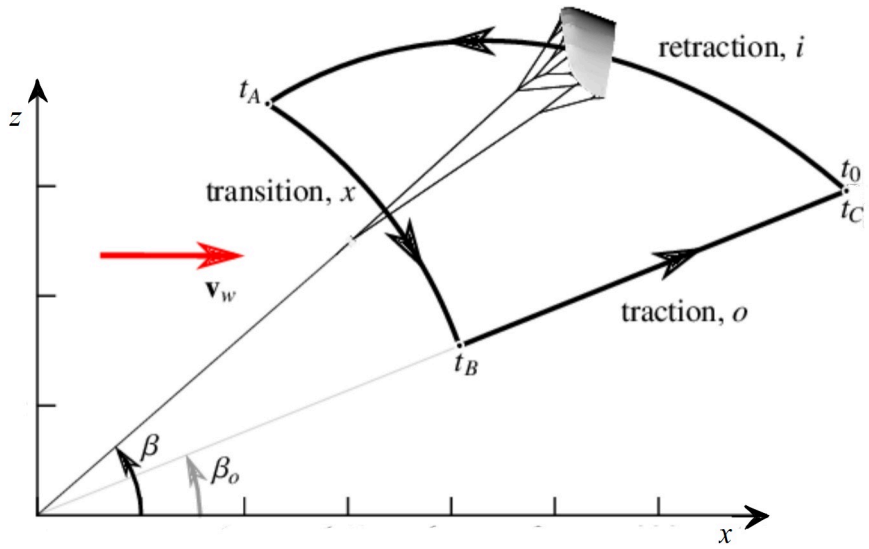

Figure 6.1: Idealised flight path trajectory of a pumping kite. Adapted from [64]

During the traction phase, the kite is considered to be in a ”powered” state. An L/D ratio between 3-5 is usually set to the kite properties. The tether is reeled-out and mechanical power is produced. The reel-out energy output is dependent on the power generated during the traction phase and the time for which the kite reaches the maximum tether length. Higher power levels and longer energy production periods are desired. During the retraction phase, the tether is reeled-in and mechanical power is consumed. Similarly, the energy consumed during the reel-in phase is a function of the power level and the time for which the kite reaches the minimum tether length. Conversely, a shorter reel-in time is sought as well as lower power levels. Simulating every point along the pumping cycle means that the transition path between the maximum and minimum elevation angles is resolved. The Luchsinger and QSM Steady State Analysis does not model or account for the transition phase. The objective of the transition phase is to fly back to the lower elevation angle and to safely increase the tether force to the tether force during the traction phase[48].

The models specify the wind speed that the pumping cycle is evaluated at and its associated probability density function. Since the power output of the traction phase is ruling for the net energy produced, the mid-altitude of that phase is used for the evaluation of the wind resource.

$$z_o = \frac{1}{2}\left(z\left(t_B\right) + z\left(t_C\right)\right) \sin \beta_{out} \tag{6.1}$$

Please note that the typical crosswind flight manoeuvres during the traction phase are not explicitly modelled. Instead of resolving every point along the figure of eight trajectories, which would be computationally expensive, a characteristic point is defined by a constant elevation and azimuthal angle Figure 6.2. This is a single characteristic flight state.

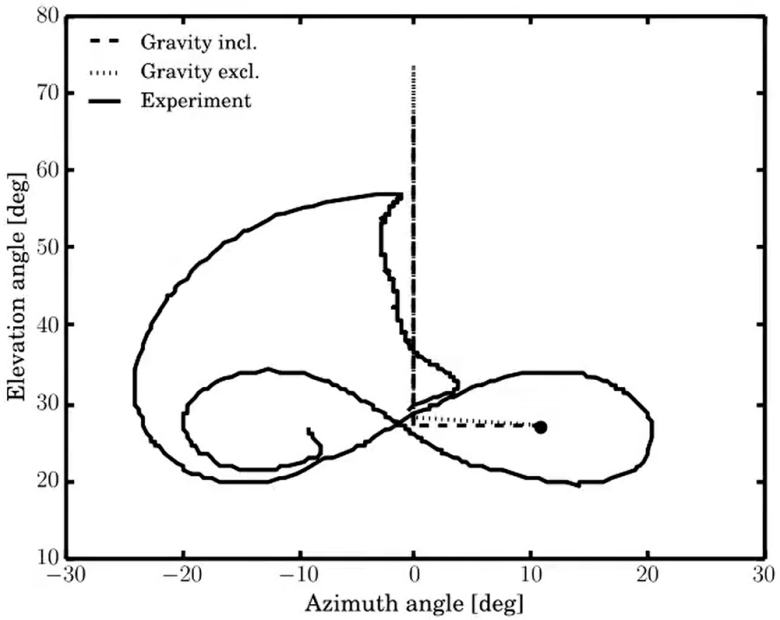

Figure 6.2: Kite position elevation and azimuth angles over a full cycle from experimental data. The dot symbol in the center of the figure eight lobe represents the characteristic constant azimuth and elevation angles that are used for modelling the traction phase. The vertical line represents the modelling of the retraction phase.

Mean Cycle Power

The total cycle power is computed by summing the average energy of each phase and dividing it by the total time of the pumping cycle, as seen below.

$$P_m = \frac{P_{out}t_{out} + P_{in}t_{in} + P_{trans}t_{trans}}{t_{out} + t_{in} + t_{trans}} \tag{6.2}$$

Averaged power output per sol
Following, the average power produced for a certain period is evaluated. The periods of interest for which the produced power is averaged are the longest period of time for which the environment data remains the same. As there is a significant variation in average atmospheric density throughout a Martian year, the averaged power evaluation is made on a sol-to-sol basis. Using the three-phase strategy, one can obtain power output per sol P_s through integrating the electrical cycle power times its probability over a velocity range, as also formulated in the equation below.

$$P_s = \int_{v_{w,i}}^{v_{n,T}} P_c(v_w) g_W(v_w)\, dv_w + \int_{v_{n,T}}^{v_n^p} P_c(v_w) g_W(v_w)\, dv_w + \int_{v_{n,P}}^{v_{w,f}} P_c(v_w) g_W(v_w)\, dv_w \tag{6.3}$$

For the above relation, it is already discussed that $P_{c,e}$ depends on the density so it would have a new value for each density instance that is simulated. The Weibull probability of a certain velocity $g_w\,(v_w)$ has as many instances as Weibull parameter sets evaluated; in this case, there are sixteen instances throughout the Martian Year. The four periods for each of Mars's four seasons as given in Appendix A. Left to be discussed in the above equation are the integral boundaries and the cosine term.

First, the upper boundary of the above integral, $v_{cut_{out}}$, denotes the highest wind velocity of interest for this on-design simulation; this is either the maximum wind velocity at which the kite is operational or the wind velocity at which the Weibull probability rounds to zero. Similar logic is applied to the evaluation of the lower boundary of the integral, $v_{cut_{in}}$. Through this parameter, the simulations can be started at a velocity for which the aerodynamic force on the wing is large enough to counteract the gravitational forces on the kite and tether. Initially, a $v_{cut_{in}} = 9$ m/s was considered, but later the QSM with mass indicated $v_{cut_{in}} = 15.5$ m/s was more realistic. Attempting to input lower wind speeds would cause the simulations to fail.

6.1.2. Models

Two different models were used to quantify the performance of various kite sizes, namely, the Luchsinger Model and the Quasi-Steady Model (QSM). The reason for using two performance models is to be able to validate the results. Additionally, the QSM is able to account for the effects of kite and tether mass on the mean cycle power. Both of these models assume that the tether is straight and the aerodynamic properties of the kite are constant per phase. Furthermore, both models assume a constant wind field.

Luchsinger Performance Model

The Luchsinger kite performance analysis is used for estimating the net power generated by the kite over a whole cycle [47]. The net power produced is equal to the power generated during the reel-out phase minus the power consumed in the reel-in phase. Notably, this does not include the transition phase. Besides, the ambient wind velocity, the power produced is dependent on the reel-out velocity, v_{out}, while the power consumed is dependent on the corresponding reel-in velocity, v_{in}. Those two operational velocities can be optimised in order to achieve the maximum produced power possible. The maximum cycle power as a function of operational parameters for 3 different operational settings is presented. To make the analysis applicable for any wind conditions, the dimensionless variables $\gamma_{in} = \frac{v_{in}}{v_w}$ and $\gamma_{out} = \frac{v_{out}}{v_w}$ are defined.

The aerodynamic force analysis of the kite is based on the apparent wind velocity that it experienced. The derivation of the apparent velocity during the reeling out cycle is derived in [47] and presented in the following Equation 6.4; note that it considers only cases for which $C_L/C_D \gg 1$.

$$v_{a,out} = v_w \left(\cos\beta_{out} - \gamma_{out}\right) \frac{C_L}{C_D} \tag{6.4}$$

Moreover, the tension of the tether T is approximately equal to the lift force on the kite as seen in the equation below

$$T \simeq L = \frac{1}{2}\rho v_a^2 A C_L \tag{6.5}$$

Combining the two expressions in Equation 6.4 and Equation 6.5, the tether force can be written as:

$$T_{out} = \frac{1}{2}\rho v_w^2 A \left(\cos\beta_{out} - \gamma_{out}\right)^2 F_{out} \tag{6.6}$$

Likewise, the apparent wind velocity during the retraction phase of the cycle is derived in [47] and presented below in Equation 6.7.

$$v_{a,in} = \sqrt{v_w^2 + 2v_w v_{in}\cos\beta_{in} + v_{in}^2} \tag{6.7}$$

From that expression and the approximation of the tether force to the aerodynamic ones, the experienced load in the tether during the reel-in phase can be written as

$$T_{in} = \frac{1}{2}\rho v_w^2 A \left(1 + 2\gamma_{in}\cos\beta_{in} + \gamma_{in}^2\right) F_{in} \tag{6.8}$$

Now that the tether forces during the phases of interest are known, the cycle mechanical energy can be evaluated. The mechanical energy of a phase is equal to the tether force times the length change of the tether l_c. Therefore, the cycle energy can be expressed as

$$\begin{aligned} E_c &= \left(T_{out} - T_{in}\right) l_c = \\ &= \frac{1}{2}\rho v_w^2 A \left(\left(\cos\beta_{out} - \gamma_{out}\right)^2 F_{out} - \left(1 + 2\gamma_{in}\cos\beta_{in} + \gamma_{in}^2\right) F_{in}\right) l_c \end{aligned} \tag{6.9}$$

The cycle power can be calculated by dividing the cycle energy by the cycle time which can be obtained by considering the following expression in

$$t_c = \frac{l_c}{v_{out}} + \frac{l_c}{v_{in}} = \frac{l_c}{v_w}\left(\frac{\gamma_{out}\gamma_{in}}{\gamma_{out} + \gamma_{in}}\right) \tag{6.10}$$

Hence, combining Equation 6.9 and Equation 6.10, the normalised cycle power f_c is found to be equal to

$$\frac{P_c}{P_w A F_{out}} = f_c = \left(\left(\cos\beta - \gamma_{out}\right)^2 - \frac{F_{\text{in}}}{F_{\text{out}}}\left(\gamma_{\text{in}}^2 + 2\cos\beta\gamma_{\text{in}} + 1\right)\right)\left(\frac{\gamma_{\text{out}}\,\gamma_{\text{in}}}{\gamma_{out} + \gamma_{\text{in}}}\right) \tag{6.11}$$

where the P_w parameter denotes the power density of the wind given by

$$P_w = \frac{1}{2}\rho v_w^3 \tag{6.12}$$

In order to obtain the maximum cycle power for different traction velocities, it must be evaluated when the derivative of the normalised force is equal to zero

$$\frac{d}{d\gamma_{out}}\frac{P_c}{P_w A F_{out}} = \frac{d}{d\gamma_{out}}\left(\cos\beta_{out} - \gamma_{out}\right)^2 \gamma_{out} = 0 \quad \leftrightarrow \quad \gamma_{out} = \frac{1}{3}\cos\beta_{out} \tag{6.13}$$

Therefore, if the retraction power is idealised to be zero, the maximum power cycle can be expressed as

$$P_c^{\text{max}} = P_w A F_{\text{out}}\,\frac{4}{27}\cos^3\beta_{\text{out}} \tag{6.14}$$

In reality, this ideal scenario is not achievable and the actual cycle power needs to be evaluated while considering system force and power limitations. The performance constraints originate from the maximum tension force that the tether can withstand, and the maximum mechanical power that the generator can withstand. The previous derivations do not consider the power and force limits, hence, it holds true while the tether force is less than the maximum and the generator produces less power than the nominal value.

Next, the maximum cycle power as a function of operational parameters for three different operational settings is presented. First, the actual maximum cycle power for which the system operates

under no constraints is presented as following the derivation above. Afterwards, the power limit derivation assumes that the maximum tether force is already obtained. A detailed derivation is presented in [47]. However, the derivation for the operational region at which the nominal tether force is reached but the nominal electrical output is not is obtained without the consideration of the elevation angle in [47]. By following the steps of the same derivation, the maximum cycle power for that region is presented. Lastly, an overview of how to combine all the results in a single operation strategy is presented.

No force or power constraints
First, to obtain the optimal produced power when there are no imposed limitations from the tether and the ground station generator, Equation 6.11 the normalised cycle power f_c needs to be maximised. Here, the dimensionless operational variables γ_{in} and γ_{out} can be evaluated be through satisfying the following mathematical expression which considers any positive force factors, $F_{in}, F_{out} > 0$:

$$f_c = \max_{\gamma_{out},\gamma_{in}} \left\{ \left((\cos\beta - \gamma_{out})^2 - \frac{F_{in}}{F_{out}} \left(\gamma_{in}^2 + 2\cos\beta\gamma_{in} + 1 \right) \right) \left(\frac{\gamma_{out}\gamma_{in}}{\gamma_{out} + \gamma_{in}} \right) \right\} \tag{6.15}$$

where the dimensionless force factor F_{out} and F_{in} are defines as

$$F_{out} = \frac{C_{\mathrm{L,out}}^3}{C_{\mathrm{D,out,eff}}^2} \qquad F_{\mathrm{in}} = C_{D_{\mathrm{in,eff}}} \tag{6.16}$$

Where $C_{\mathrm{D,out,eff}}$ and $C_{\mathrm{D,in,eff}}$ are the effective drag coefficients that account for the kite drag and the tether drag.

Power constraints
The above dimensionless force derivation is applicable when neither the nominal power generation of the ground station nor the nominal tension force in the tether has not been reached. Nevertheless, at a certain wind speed v_n, the airborne kite system reached its nominal power output, P_{out}^n. It is assumed that the nominal tether force T_{out}^n is also reached at the examined velocity v_n. Therefore, as those two limits are reached for $v_w > v_n$, the power produced during the reel-out phase and the corresponding tether force and reel-out velocity must remain constant. This leaves only the reel in velocity as a variable to be optimized in this case. Similarly to the above analysis, the derivation for the dimensionless power factor, f_c, with the imposed generator power and tether force limitations, results in an expression to be maximised [47]

$$\begin{aligned} f_c^P = \max_{\gamma_{in}} \Bigg\{ \Bigg(& \frac{1}{\mu_P^2} \left(\cos\beta_{out} - \gamma_{out}^{n,P} \right)^2 \\ & - \frac{F_{in}}{F_{out}} \left(\gamma_{in}^2 + 2\cos\beta_{in}\gamma_{in} + 1 \right) \Bigg) \left(\frac{\gamma_{out}^{n,P}\gamma_{in}}{\gamma_{out}^{n,P} + \mu_P\gamma_{in}} \right) \Bigg\} \end{aligned} \tag{6.17}$$

In the above equation the dimensionless velocity parameter, μ, defines the ratio of the experienced and the nominal wind velocities which is greater than 1. This nominal wind velocity, $v_{n,p}$ is the wind velocity at which the nominal power is experienced.

$$\mu_P = \frac{v_w}{v_{n,P}} > 1 \tag{6.18}$$

Tether force constraints
A key assumption in the derivation above is that the tether force limit is reached at the same nominal wind velocity at which the nominal power is reached. However, an alternative control strategy is to increase the reel-out velocity above its optimal value while the tether force remains constant; this results in an increased generated power during the reel-out phase [47]. Therefore, two different nominal velocities are considered, $v_{n,T} = v_{n,P}$ for the derivations shown below. The derivation follows the method outlined in [47], but the influence of the elevation angle is included.

First, the tether force is evaluated through the previous Equation 6.6 and the limitation of the nominal tether force definitive of this operational region, is imposed through $T_{out} = T_{out}^n$. From this, the relation in the below Equation 6.19 is obtained.

$$T_{out} = \frac{1}{2}\rho v_w^2 A \left(\cos\beta_{out} - \gamma_{out}\right)^2 F_{out} = T_{out}^n = \frac{1}{2}\rho v_n^2 A \left(\cos\beta_{out} - \gamma_{out}^{n,T}\right)^2 F_{out} \tag{6.19}$$

Through this equality an expression for the operational traction dimensionless velocity γ_{out} based on its nominal value is derived as presented in Equation 6.20.

$$\gamma_{out} = \cos\beta_{out} - \frac{\cos\beta_{out} - \gamma_{out}^{n,T}}{\mu_T} \tag{6.20}$$

In the above equation μ_T is defined as in the above Equation 6.18, but with nominal wind velocity at which the maximum tether force is reached $v_{n,T}$.

$$\mu_T = \frac{v_w}{v_{n,T}} > 1 \tag{6.21}$$

After the traction settings are known, the retraction settings are examined. Notably, the tether force during the retraction phase is much smaller than during the traction phase. As such, the nominal tether force limit is not imposed. Therefore, the equation given Equation 6.8 holds true during the retraction phase. Next, with these parameters known, the cycle time of the pumping cycle can be evaluated as in Equation 6.10. Substituting Equation 6.20 into Equation 6.10, the cycle time t_c is considered as

$$\begin{aligned} t_c &= \frac{l_c}{v_w}\left[\frac{\gamma_{\text{in}} + \cos\beta_{\text{out}} - \frac{\cos\beta_{\text{out}} - \gamma_{\text{out}}^n}{\mu_T}}{\gamma_{\text{in}}\left(\cos\beta_{\text{out}} - \frac{\cos\beta_{\text{out}} - \gamma_{\text{out}}^n}{\mu_T}\right)}\right] \\ &= \frac{l_c}{v_w}\left[\frac{\gamma_{\text{in}}\,\mu_T + \mu_T\cos\beta_{\text{out}} - \cos\beta_{\text{out}} + \gamma_{\text{out}}^n}{\gamma_{\text{in}}\left(\mu_T\cos\beta_{\text{out}} - \cos\beta_{\text{out}} + \gamma_{\text{out}}^n\right)}\right] \end{aligned} \tag{6.22}$$

Next, the cycle energy E_c in the retraction phase is expressed as

$$\begin{aligned} E_c &= \left(T_{\text{out}}^n - T_{\text{in}}\right) l_c = \\ &= \frac{1}{2}\rho v_w^2 A\left(\frac{1}{\mu_T^2}\left(\cos\beta_{\text{out}} - \gamma_{\text{out}}^{n,T}\right)^2 F_{\text{out}} - \left(1 + 2\gamma_{\text{in}}\cos\beta_{\text{in}} + \gamma_{\text{in}}^2\right) F_{\text{in}}\right) l_c \end{aligned} \tag{6.23}$$

Now that the cycle time and cycle energy are computed, the cycle power can be expressed as

$$\begin{aligned} P_c = P_w A F_{\text{out}}\Bigg[&\left(\frac{1}{\mu_T^2}\left(\cos\beta_{\text{out}} - \gamma_{\text{out}}^{n,T}\right)^2 - \frac{F_{\text{in}}}{F_{\text{out}}}\left(\gamma_{\text{in}}^2 + 2\cos\beta_{\text{in}}\,\gamma_{\text{in}} + 1\right)\right) \\ &\left(\frac{\gamma_{\text{in}}\left(\mu_T\cos\beta_{\text{out}} - \cos\beta_{\text{out}} + \gamma_{\text{out}}^{n,T}\right)}{\mu_T\gamma_{\text{in}} + \mu_T\cos\beta_{\text{out}} - \cos\beta_{\text{out}} + \gamma_{\text{out}}^{n,T}}\right)\Bigg] \end{aligned} \tag{6.24}$$

For the retraction phase, the maximum dimensionless power is computed as

$$\begin{aligned} f_c^T = \max_{\gamma_{in}}\Bigg\{&\left(\frac{1}{\mu_T^2}\left(\cos\beta_{out} - \gamma_{out}^{n,T}\right)^2 - \frac{F_{in}}{F_{out}}\left(\gamma_{in}^2 + 2\cos\beta_{in}\gamma_{in} + 1\right)\right) \\ &\left(\frac{\gamma_{in}(\mu_T\cos\beta_{out} - \cos\beta_{out} + \gamma_{out}^{n,T})}{\mu_T\gamma_{in} + \mu_T\cos\beta_{out} - \cos\beta_{out} + \gamma_{out}^{n,T}}\right)\Bigg\} \end{aligned} \tag{6.25}$$

Now that the maximum cycle power can be found for different wind speeds by evaluating the optimum normalised reel in and out velocities.

Luchsinger three region strategy

The cycle power of a pumping kite system is evaluated by dividing the wind spectrum in three different phases: low wind speeds $0 \leq v_w \leq v_{n,T}$, medium wind speeds $v_{n,T} \leq v_w \leq v_{n,P}$, and high wind speeds $v_w \leq v_{n,p}$. For the low wind speeds, neither the tether force nor the power limits are reached, hence, Equation 6.15 is used. For medium wind speeds, the tether force cannot be increased further but the power limit is not yet reached, hence Equation 6.25 is used. Lastly, for high wind speeds, both the tether force and the power limits are reached, hence, Equation 6.17 is used to evaluate the value of γ_{in}. Through this strategy, the operational envelope of the pumping kite can be evaluated.

Quasi-Steady Performance Model

The kite's motion is approximated as a transition through a series of steady states [62]. The QSM uses an idealised flight path of the kite, consisting of three phases: the reel-in, transition, and reel-out. The cross-wind manoeuvres of the kite are not resolved and the average performance in the reel-out phase is approximated using a constant elevation, azimuth, and course angle [62].

There are several assumptions that reduce the complexity of the computational approach in order to reduce the computation cost of the simulations. The QSM is limited to large kites with large surface-to-mass ratios. The timescale of dynamic processes for large kites is generally very short compared to the timescales of typical flight manoeuvres or complete pumping cycles. Therefore, the flight operation is dominated by the balance of aerodynamic, tether and gravitational forces and can be approximated as a transition through quasi-steady flight states [48]. Additionally, the tether is assumed to be inelastic and is represented as a straight line in the model. However, if the mass is accounted for, the effect of sagging due to distributed gravitational loading is taken into account. As mentioned before, the aerodynamic coefficients of the kite are assumed to be constant throughout each phase.

The QSM can be implemented in different ways. The complexity and fidelity of the model are increased gradually through out this section. The QSM represents the kite as a point mass. Unlike the Luchsinger model, QSM can account for the transition phase.

A detailed explanation of the basic modelling framework is explained in [48]. As shown in Figure 6.3 the position of the kite is described by the radial distance r, the polar angle θ and the azimuth angle ϕ. The direction of flight in the local tangential plane τ is described by the course angle χ.

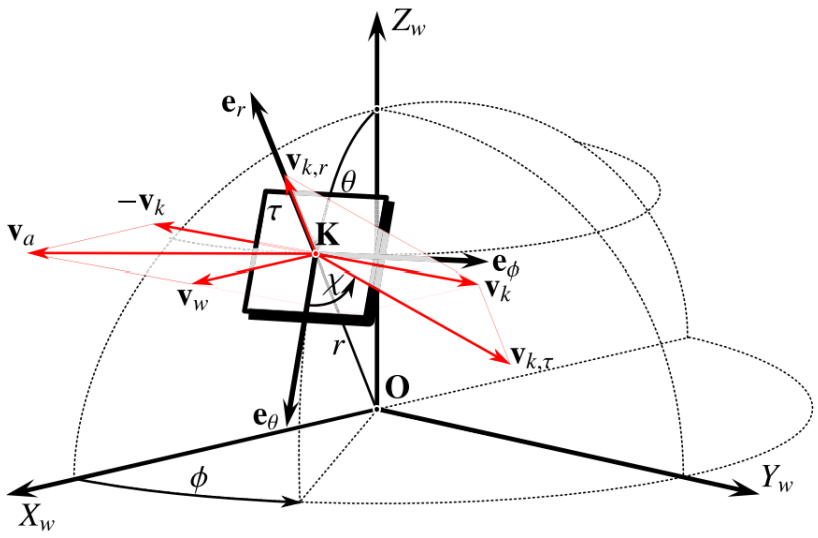

Figure 6.3: QSM coordinate system [65]

[48] explains that the apparent wind velocity in spherical coordinates can is described as

$$\mathbf{v}_a = \begin{bmatrix} \sin\theta\cos\phi \\ \cos\theta\cos\phi \\ -\sin\phi \end{bmatrix} v_w - \begin{bmatrix} 1 \\ 0 \\ 0 \end{bmatrix} v_{k,r} - \begin{bmatrix} 0 \\ \cos\chi \\ \sin\chi \end{bmatrix} v_{k,\tau} \tag{6.26}$$

where $v_{k,r}$ and $v_{k,\tau}$ represent the radial and tangential contributions to the kite velocity, respectively. Here we introduce to reeling factor (left) and tangential velocity factor (right)

$$f = \frac{v_{k,r}}{v_w} \qquad \lambda = \frac{v_{k,\tau}}{v_w} \tag{6.27}$$

The lift and drag forces contributed by the wing are computed as

$$L = \frac{1}{2}\rho C_L v_a^2 S \qquad D_k = \frac{1}{2}\rho C_{D,k} v_a^2 S \tag{6.28}$$

Where C_L and $C_{D,k}$ are the aerodynamic lift and drag coefficients, respectively. Additionally, S is the planform area of the kite. The total aerodynamic drag D if the AWE system is then estimated as

$$D = D_k + D_t \tag{6.29}$$

The tether drag is expressed as

$$D_t = \frac{1}{8}\rho d_t r C_{D,c} v_a^2 \tag{6.30}$$

Where d_t is the tether diameter, r the tether length, $C_{D,c}$ the drag coefficient of a cylinder in cross flow and v_a is the apparent wind velocity of the kite [48]. The total aerodynamic drag coefficient of the airborne system components is computed as

$$C_D = C_{D,k} + \frac{1}{4}\frac{d_t r}{S} C_{D,c} \tag{6.31}$$

Steady State Analysis
In order to identify the lift and drag coefficient of the kite, a steady kite model is used. The prescribed coefficients and wind speeds are used as inputs for a steady system model to approximate the instantaneous kite velocity. Notably, this only evaluates the instantaneous states and does not resolve how they evolve over time.

Analytic Model Without the Effect of Mass
When the mass is not considered, the radial and tangential components of the apparent wind velocity and the lift and drag components of the aerodynamic force are related as follows

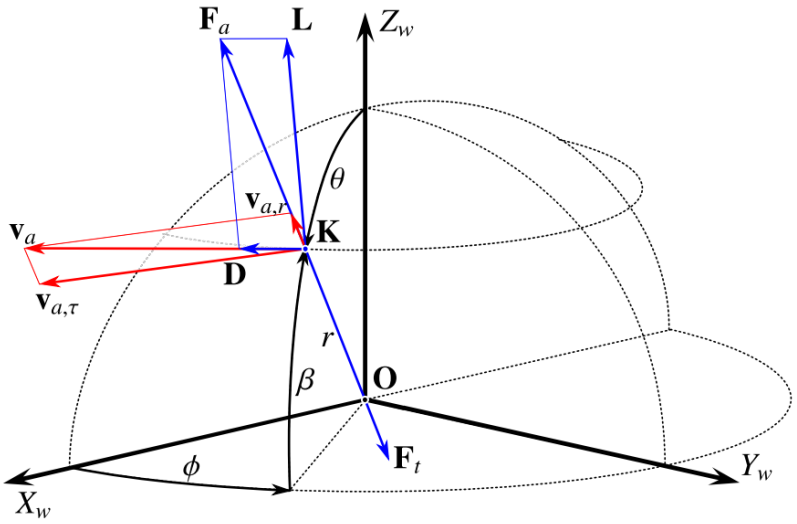

Figure 6.4: Geometrical similarity of the force and velocity diagrams. $\mathbf{V}_a$ and $\mathbf{F}_a$ are decomposed in the plane spanned by the two vectors. **D** is aligned with $\mathbf{V}_a$, whereas $\mathbf{V}_{a,r}$ is aligned with $\mathbf{F}_a$ when assuming a straight tether and a negligible effect of mass. [65]

The kinematic ratio, κ, is the ratio of the relative velocity components and is expressed as

$$\kappa = \frac{v_{a,\tau}}{v_{a,r}} = \frac{L}{D} \tag{6.32}$$

The non-dimensional apparent wind velocity is computed by

$$\lambda = a + \sqrt{a^2 + b^2 - 1 + \left(\frac{L}{D}\right)^2 (b - f)^2} \tag{6.33}$$

Where the trigonometric coefficients can be solved as

$$\begin{aligned} a &= \cos\theta \cos\phi \cos\chi - \sin\phi \sin\chi \\ b &= \sin\theta \cos\phi \end{aligned} \tag{6.34}$$

Notable, the quasi-steady motion of a massless kite is governed by the equilibrium of the tether force and resultant aerodynamic force.

$$\mathbf{F}_t + \mathbf{F}_a = 0 \tag{6.35}$$

By inserting the lift and drag equations from Equation 6.28 into the Equation 6.35 results in

$$F_t = \frac{1}{2}\rho C_R v_a^2 S \tag{6.36}$$

Where the resultant aerodynamic force coefficient is expressed as

$$C_R = \sqrt{C_D^2 + C_L^2} \tag{6.37}$$

The normalised tether force in [48] is defined as

$$\frac{F_t}{qS} = C_R \left[1 + \left(\frac{L}{D}\right)^2\right] (\sin\theta \cos\phi - f)^2 \tag{6.38}$$

The traction power is determined as the product of tether force and reeling velocity.

$$P = F_t v_t = F_t f v_w \tag{6.39}$$

Expressing the tether force by Equation 6.38 results in

$$\zeta = \frac{P}{P_w S} = C_R \left[1 + \left(\frac{L}{D}\right)^2\right] f(\sin\theta \cos\phi - f)^2 \tag{6.40}$$

P_w denotes the wind power density at the altitude of the kite

$$P_w = \frac{1}{2}\rho v_w^3 \tag{6.41}$$

Analytic Model including the effect of mass

The apparent wind velocity and the decomposition of the aerodynamic force into lift and drag components can be seen in Figure 6.5.

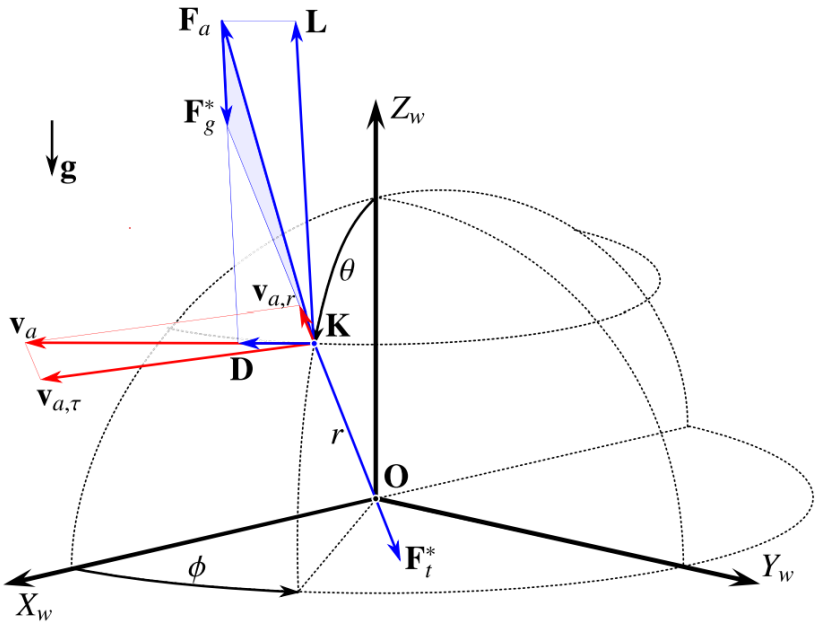

Figure 6.5: Steady force equilibrium considering the effect of gravity [48].

The gravitation force causes a misalignment of the aerodynamic force and the tether force. Therefore, the geometric similarity of the force and velocity diagrams does not hold anymore. As a result, the kinematic ratio can not be expressed by the lift-to-drag ratio. Therefore, the non-dimensional apparent wind velocity can be formulated as

$$\frac{v_a}{v_w} = (\sin\theta\cos\phi - f)\sqrt{1 + \left(\frac{v_{a,\tau}}{v_{a,r}}\right)^2} \tag{6.42}$$

and the tangential kite velocity factor is now expressed as

$$\lambda = a + \sqrt{a^2 + b^2 - 1 + \left(\frac{v_{a,\tau}}{v_{a,r}}\right)^2 (b - f)^2} \tag{6.43}$$

Lastly, the magnitude of the resultant aerodynamic force F_a can be formulated using Equation 6.42

$$\frac{F_a}{qS} = C_R\left[1 + \left(\frac{v_{a,\tau}}{v_{a,r}}\right)^2\right](\sin\theta\cos\phi - f)^2 \tag{6.44}$$

QSM Control Strategies

The position of the kite is updated by a finite difference scheme

$$\mathbf{r}(t + \Delta t) = \mathbf{r}(t) + \mathbf{v}_k(t)\Delta t \tag{6.45}$$

Before the nominal tether force is reached, the combination of reel-out and reel-in factors are optimised to maximise the mean cycle power found using SciPy's minimize function that is part of the optimization package in Python. With the optimal reeling factors, the power, the tether force and the reeling speed are computed. The reeling factor is the control setting for both reel-out and reel-in. Once the maximum tether force is experienced, the "tether_force_ground" is used as the control setting for the traction phase. Using the maximum tether force, the aerodynamic force is computed. This is then used to compute the lift-to-drag ratio and then compared to the actual lift-to-drag ratio. The iterative procedure used to solve for the unknown kinematic ratio, the reeling speed and corresponding aerodynamic force is explained in detail in [48]. Then the power is computed as a product of the tether force and reeling speed.

The QSM Steady State Analysis and Luchsinger model could impose power limits by simply prescribing the maximum power and tether force, which also imposes the reeling speed. While the implementation of power limits for the time series QSM simulation was attempted, the efforts did not work.

7

Performance Analysis Results

7.0.1. Luchsinger vs. QSM Steady State Analysis

The Luchsinger model [47] and the higher fidelity QSM [48] are used to simulate the performance of an AWE kite. In order to better compare the performance difference between the models, mass is not considered. The instantaneous performance (for a single point in time) during a traction and retraction phase is computed. This assumes that evaluating a single point gives a reasonable representation of the whole reeling phase. Both models neglect the transition phase. A 200 m^2 kites is considered for this analysis.

Each performance curve has three regions of control, (1) no limits, (2) tether limit, and (3) tether plus power limit. The power curves in Figure 7.1 are first in close agreement and then diverge at higher wind speeds. This is thought to occur due to the difference in how each model computes its aerodynamic forces and optimises its reeling factors. The Luchsinger model optimized the reeling factors based on maximising normalized cycle power, f_c, equations. The QSM instead finds the combination of reel-out and reel-in factors that maximise the mean cycle power P_c. Once the nominal tether force has been reached, the Luchsinger model simply optimises a different derivation of the normalised cycle power f_c and only the reel-in factor is varied. The QSM uses the nominal tether force to find the aerodynamic force from the kite, which begins the iteration procedure to find the true kinematic ratio and reeling factor, which together with the tether force computes the power. These different approaches are thought to lead to slightly different optimal results. Furthermore, the tether force is computed under slightly different assumptions. The Luchsinger model assumes that the tether force is directly dependent on the lift coefficient C_L of the kite. The QSM computes the tether force as a function of the total or resultant aerodynamic coefficient C_R. This leads to higher tether forces for the QSM, which is seen in Figure 7.3.

Power curves are constructed to characterize the mean cycle power per wind speed of the kite. The red (QSM) and blue (Luchsinger) vertical lines indicate the transition points between regions. The tether forces, reeling speeds and power during different phases of flight are shown in this section.

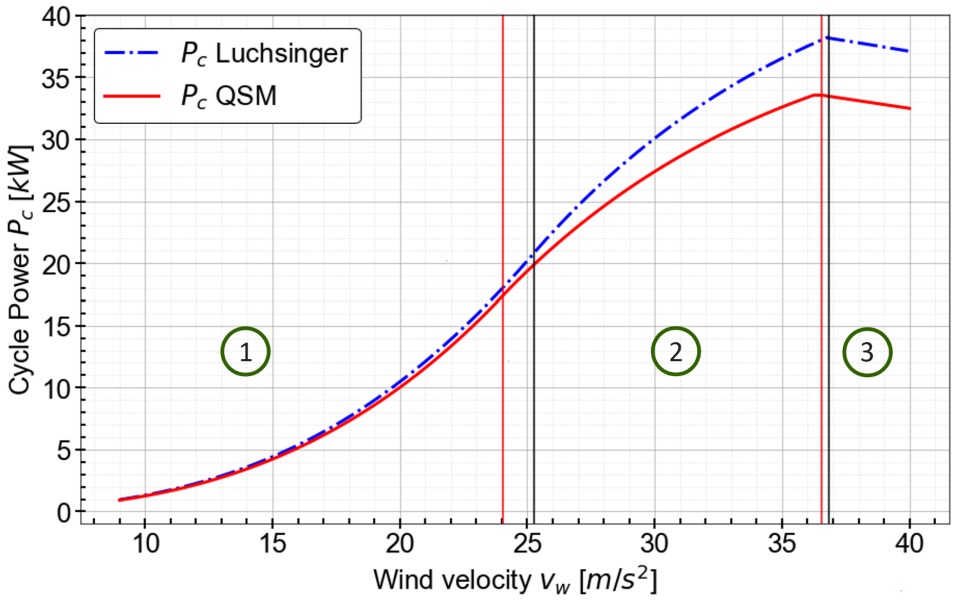

Figure 7.1: Mean cycle power curve comparison between the Luchsinger and QSM Steady State Analysis. Each performance curve has three regions of control, (1) no limits, (2) tether limit, and (3) tether plus power limit. The red (QSM) and blue (Luchsinger) vertical lines indicate the transition points between regions.

Figure 7.2 shows that the tether forces for reel-out match closely, with the QSM reaching the nominal tether force at a slightly lower wind speed. The tether force during the reel-in phase was in close agreement until reaching the maximum tether force. Additionally, in Figure 7.2 it is worth noting that the power during the reel-in phase is actually negative. It was flipped for plotting purposes.

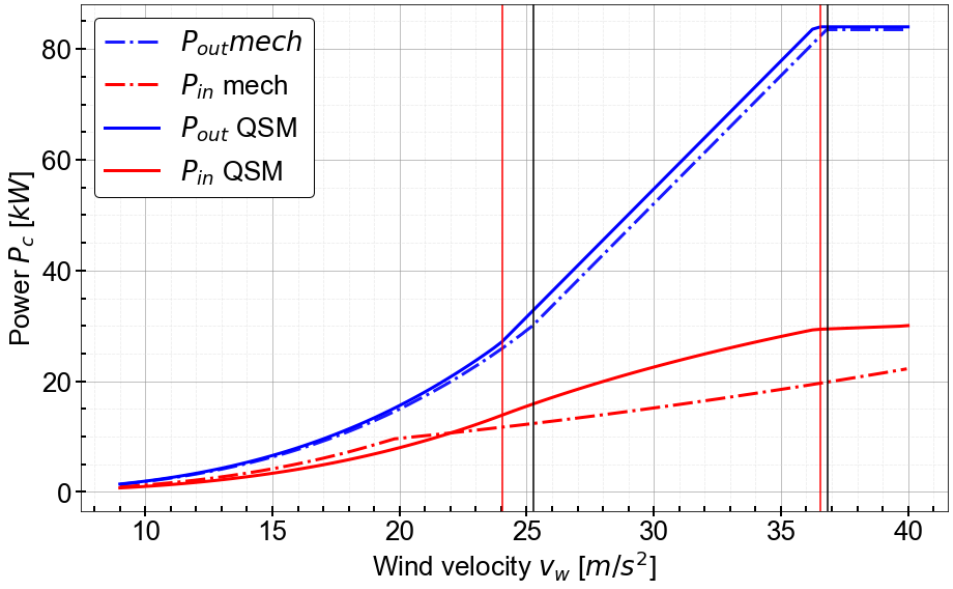

Figure 7.2: Power-in and power-out curve comparison between the Luchsinger and QSM Steady State Analysis

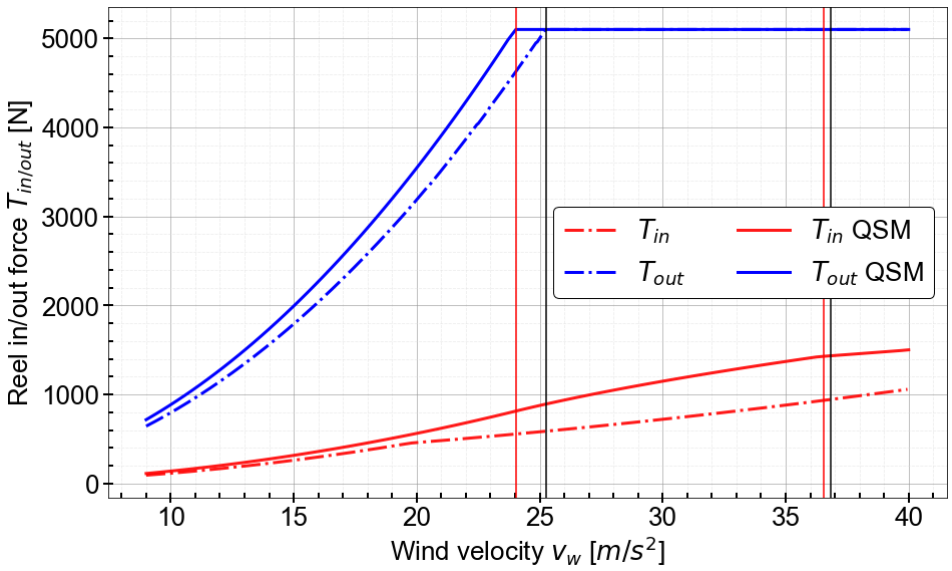

Figure 7.3: Force curve comparison between the Luchsinger and QSM Steady State Analysis

Figure 7.4 shows that the difference in reel-in speed was larger at lower wind speeds and smaller at higher wind speeds. Additionally, it is worth noting that the reeling factor and reeling velocity during the reel-in phase are actually negative. It was flipped for plotting purposes.

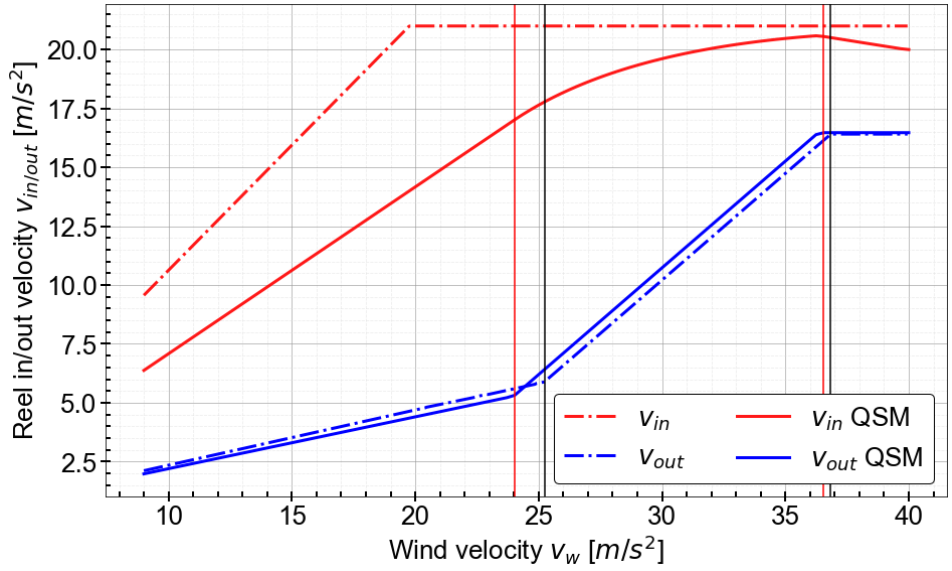

Figure 7.4: Reeling speed comparison between the Luchsinger and QSM Steady State Analysis

7.0.2. QSM Steady State Analysis vs. QSM

The output for the QSM Steady State Analysis in subsection 7.0.1 will now be compared to the results from a time series simulation where aerodynamic steady states are computed using the QSM for many points throughout the pumping cycle. The distance covered by the point particle is solved as a transition through steady states using the finite difference method. Now the transition power, tether force and reeling speeds will be included.

This is considered to be very different from the Luchsinger and the QSM Steady State Analysis because the kite is instantaneously transported to the correct elevation angle at the beginning of each phase. Simulating every point along the pumping cycle means that the transition phase between the

traction and retraction elevation angles is resolved. After the total energy per phase is computed, they are summed and divided by the total pumping cycle time to compute the mean cycle power. The average powers, average tether forces and average reeling speeds for each phase are shown in subsection 7.0.2.

Figure 7.5 shows how the QSM computes a lower power curve than the QSM Steady State Analysis. Figure 7.6 is similarly lower than the QSM Steady State Analysis, but higher than than the QSM from Figure 7.5. This indicates that the transition phase actually produces energy. The reader might ask themselves, why does the QSM Steady State Analysis produce a higher mean cycle power than the time series QSM if their average power during reel-in and reel-out is about the same? The reason for this is thought to be because the reel-in velocity for the time series QSM is lower than the QSM Steady State Analysis reel-in velocity, as can be seen in Figure 7.9. This means that the time spent in the reel-in phase is increased for the time series QSM. Equation 6.2 indicates that increasing the reel-in time will reduce the mean cycle power.

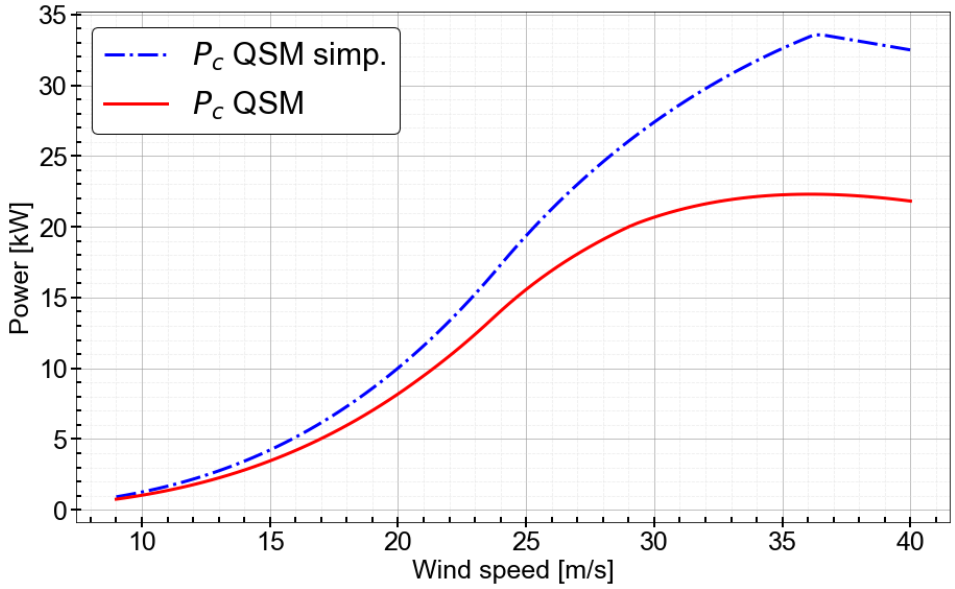

Figure 7.5: Mean cycle powers computed using the QSM Steady State Analysis (QSM simp.) and normal QSM, without including the transition energy.

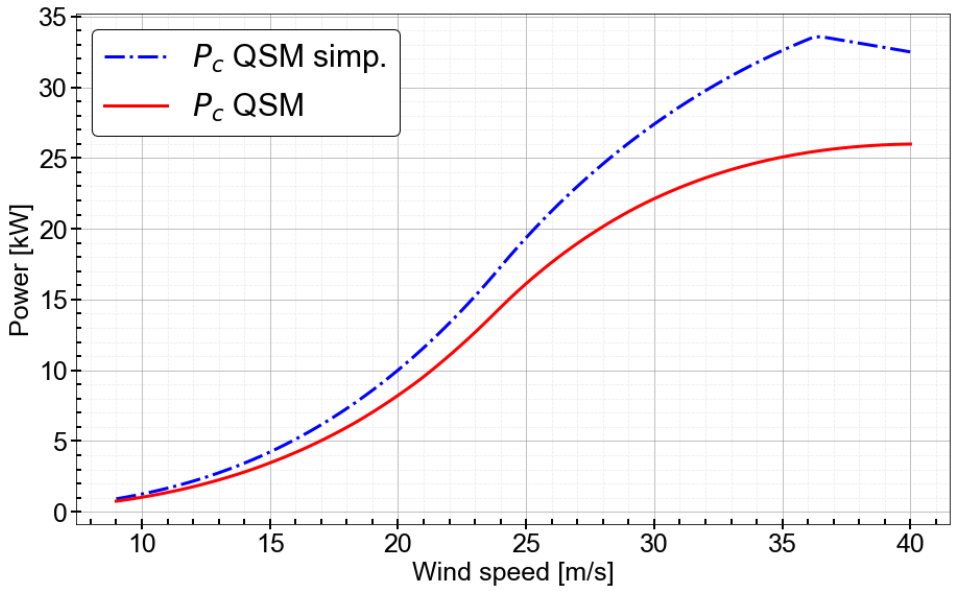

Figure 7.6: Mean cycle powers computed using the QSM Steady State Analysis (QSM simp.) and normal QSM, while including the transition energy.

Additionally, in Figure 7.7 it worth noting that the power during the reel-in phase is actually negative. It was flipped for plotting purposes. Furthermore, the implementation of a power limit for the QSM was not possible. However, the probability of wind speeds exceeding 33 m/s is considered to be zero. Therefore, the third region is not of interest here.

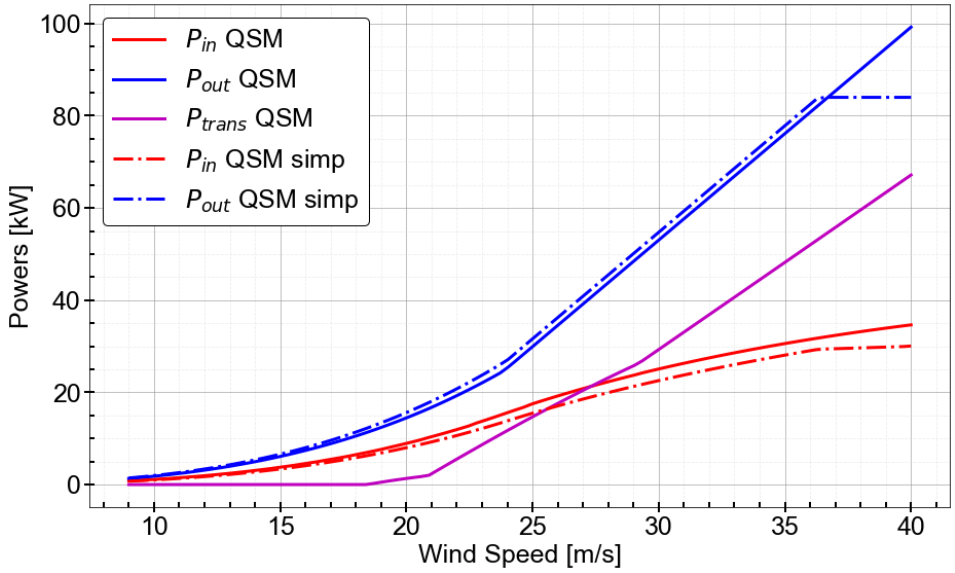

Figure 7.7: Power curve comparison during reel-in, reel-out and transition using the QSM Steady State Analysis (QSM simp.) and normal QSM

In Figure 7.8 the tether force computed by the QSM is higher than the QSM Steady State Analysis tether force. This occurs because the reel-in speed computed by the QSM in Figure 7.9 is lower than the QSM Steady State Analysis reel-in speed. Ultimately, in Figure 7.7 the reel-in speeds and tether forces both combine to compute reel-in power and are in close agreement. Additionally, it is worth noting that the reel-in velocity is actually negative. It was flipped for plotting purposes.

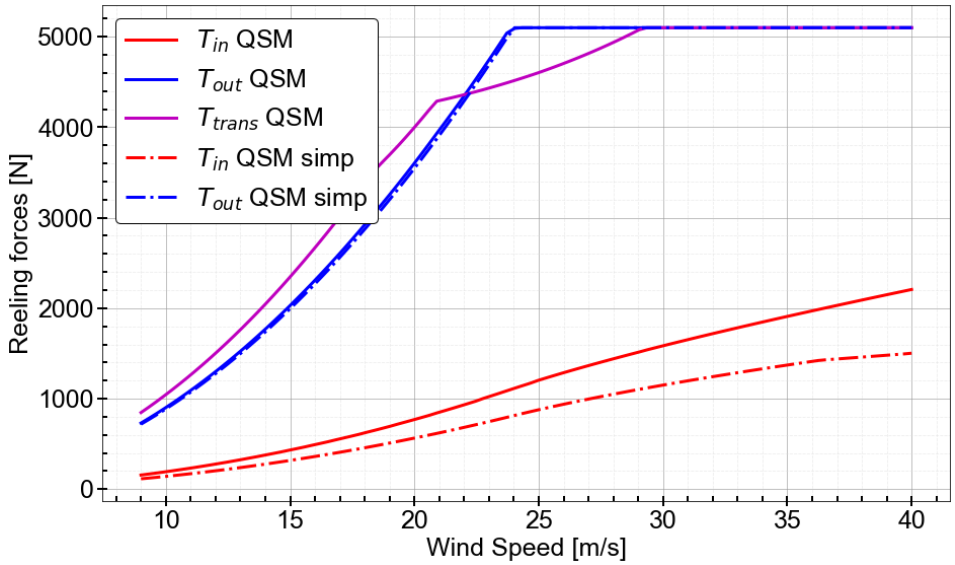

Figure 7.8: Force curve comparison during reel-in, reel-out and transition using the QSM Steady State Analysis (QSM simp.) and normal QSM

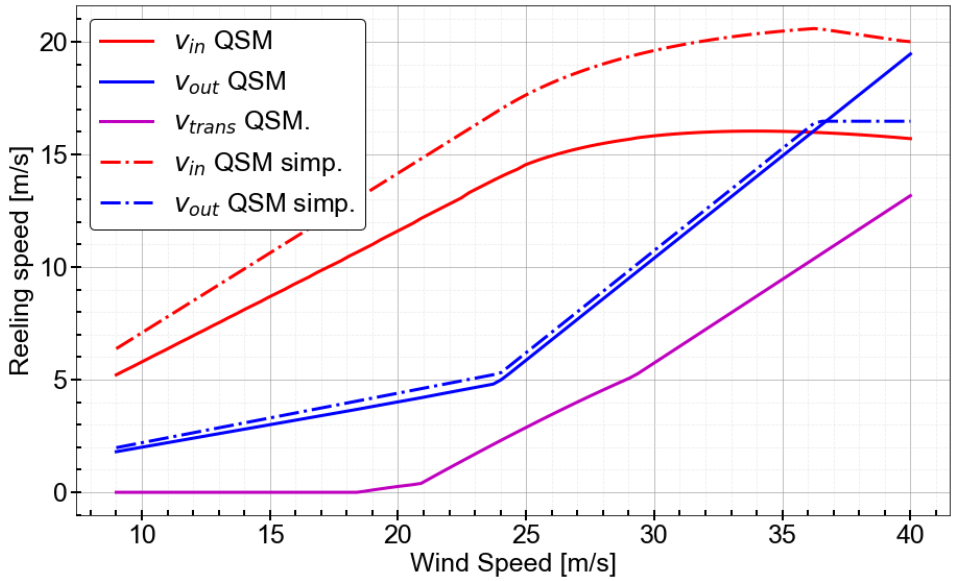

Figure 7.9: Reeling speed comparison during reel-in, reel-out and transition using the QSM Steady State Analysis (QSM simp.) and normal QSM

The next level of complexity is to include the mass of the kite and tether. Generally, mass introduces sag to the tether.

7.0.3. QSM vs. QSM with mass

Now the QSM will consider the mass of the kite and tether. The kite and tether values are listed in section 5.3. In Figure 7.10 it is evident that adding mass had the effect of increasing the mean cycle power production and increasing the cut-in wind speed. As can be seen in Figure 7.11, the mass has a significant effect on the positive power contribution from the transition phase. At higher wind speeds, the transition tether force is the same, but the transition reeling speed is higher for the QSM with mass. This results in a higher transition power for the QSM with mass.

A detailed presentation of the forces governing the fight operation of a kite including the gravita-

tional and inertial effect is provided in Refs.[65][66]. Accounting for gravity will affect the average traction power. This is because, in upward flying regions where the kinematic ratio becomes smaller, the quasi-steady flight velocity reduces. Consequently, the upward flying regions of the figure of eight trajectories require more time than the flying in the downwards flying regions. Due to this, the time average course angle can be expected to have an upward component as a result of accounting for mass [62].

The benefits of the transition power are questionable because there are discrepancies between the simulations and reality. In the QSM, the kite is allowed to reel out during the transition phase, yielding a positive power output of the system. However, in reality, the power output is virtually zero during the transition phase [62].

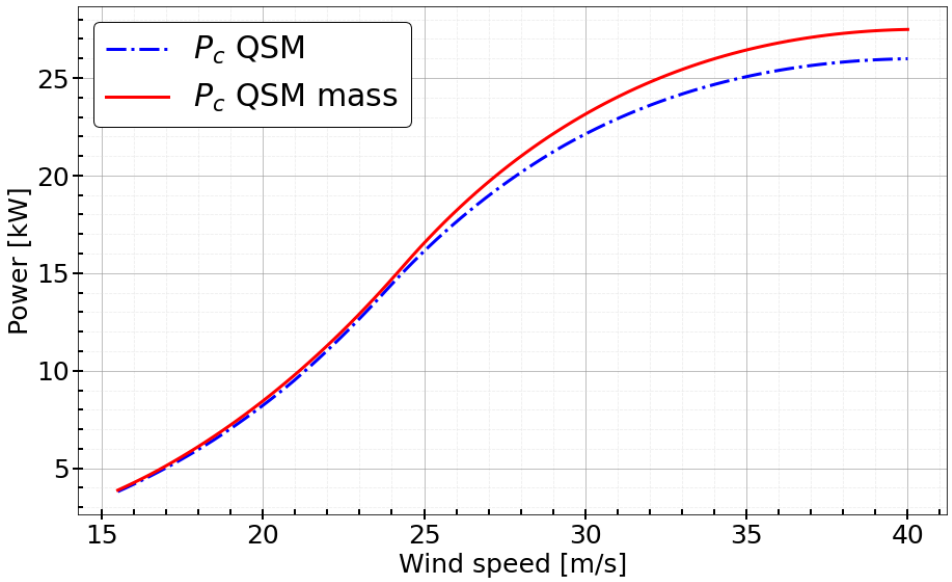

Figure 7.10: Mean cycle powers computed using the QSM with and without mass

A clear difference in the transition phase can be seen in Figure 7.11, where the mass increased the transition phase power output. The reason for that is the very high tether forces during the transition phase in Figure 7.12.

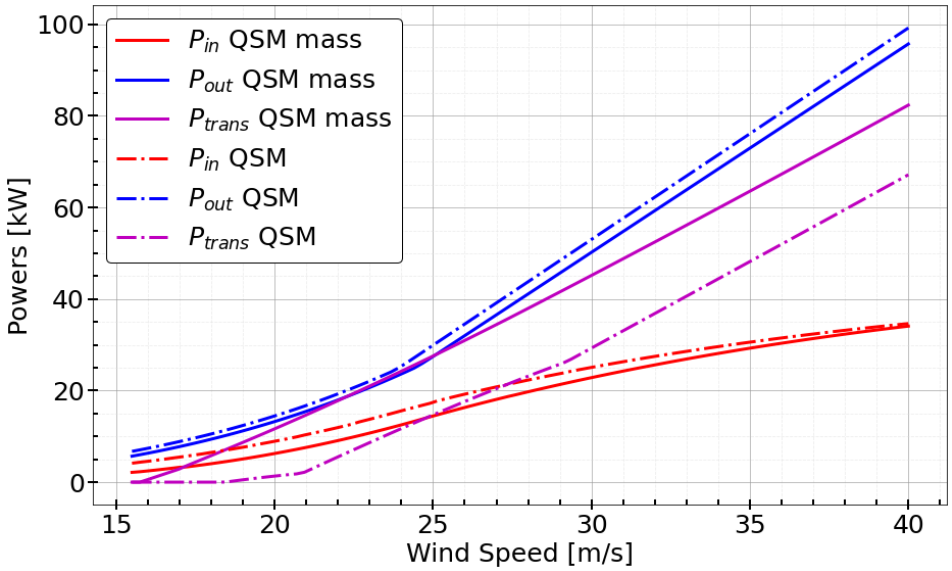

Figure 7.11: Power curve comparison during reel-in, reel-out and transition using the QSM with and without mass

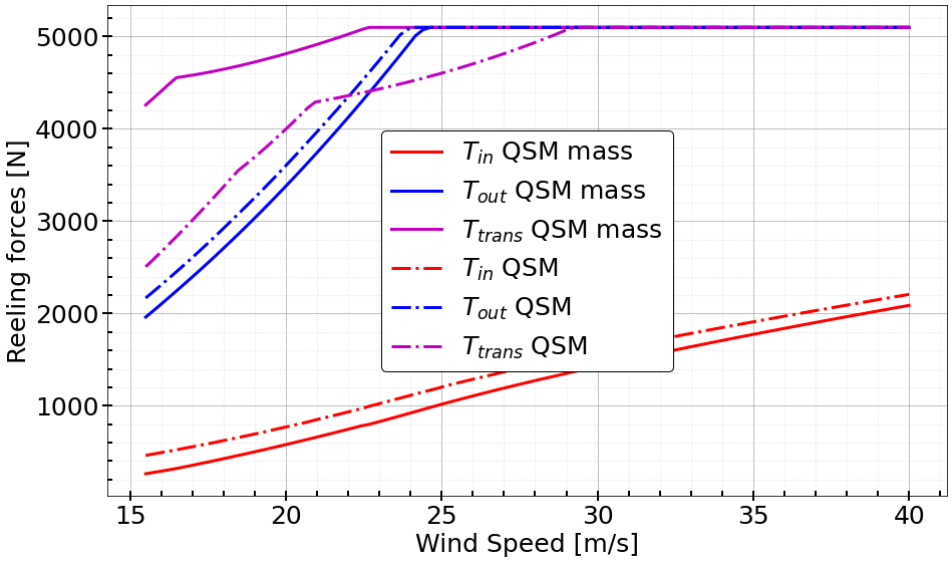

Figure 7.12: Force curve comparison during reel-in, reel-out and transition using the QSM with and without mass

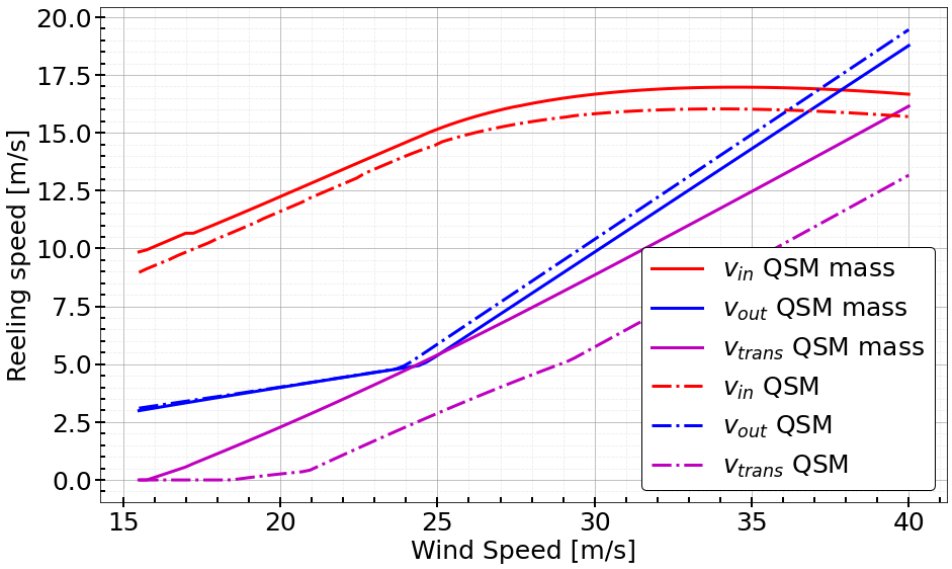

Figure 7.13: Reeling speed comparison during reel-in, reel-out and transition using the QSM with and without mass

7.1. Pumping cycle performance over time

Here the performance of the kite can be seen during a pumping cycle at 15.5 m/s. When not considering mass, the reeling speed and power are increased during the transition phase. In fact, the reeling speed and power spike briefly at the end of the traction phase in Figure 7.15.

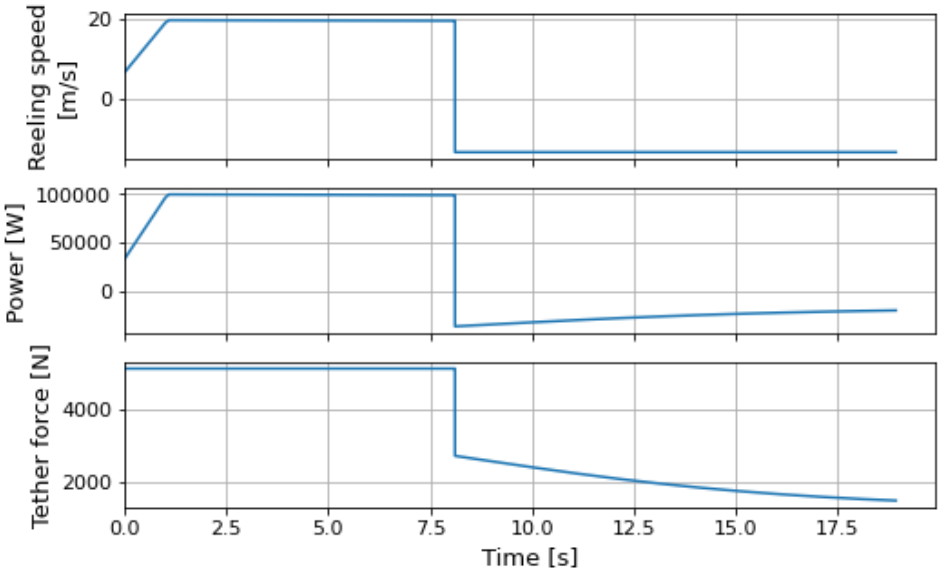

Figure 7.14: Pumping cycle simulation at 15.5 m/s considering no mass

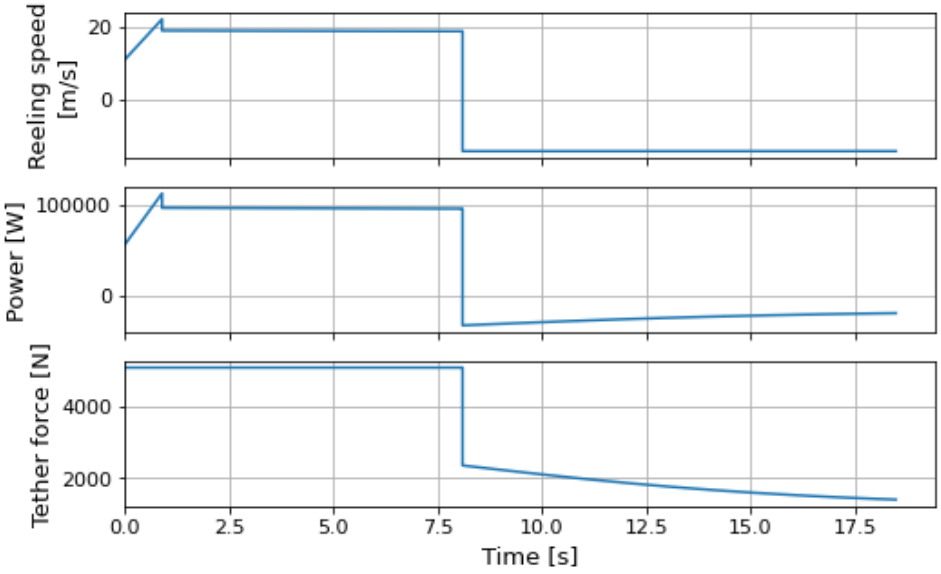

Figure 7.15: Pumping cycle simulation at 15.5 m/s considering mass

7.2. Experimental Data Verification

In order to validate my QSM, the performance of the Kitepower's V3 demonstrator kite was simulated with Earth conditions using the QSM (considering mass and transition phase) and compared against the experimental data extracted from [64]. The data is not expected to match perfectly because the wind speed recorded during the flight was at 10 m in height. However, the wind speed in the QSM is the wind speed at the kite's pattern height. Secondly, the V3 kite increases its elevation angle as a de-powering mechanism, while the QSM keeps the elevation angle constant. The QSM uses the inputs listed in Table 5.6 and Table 5.7. However, in this case, the atmospheric density is set to 1.225 kg/m^3 and the gravitational acceleration is set to 9.81 m/s^2 since this experimental data was collected on Earth.

The shape of the power curve computed by the QSM simulations appears to be similar to that of the experimental data. The same tether force limits were imposed so this similarity is expected. In order to get a better idea of what wind speeds the kite was experiencing during the experimental flight, a simple log law wind profile was assumed and the average height during the traction phase was take as the "scaled" wind speed. As can be seen in Figure 7.16, the power matches relatively closely.

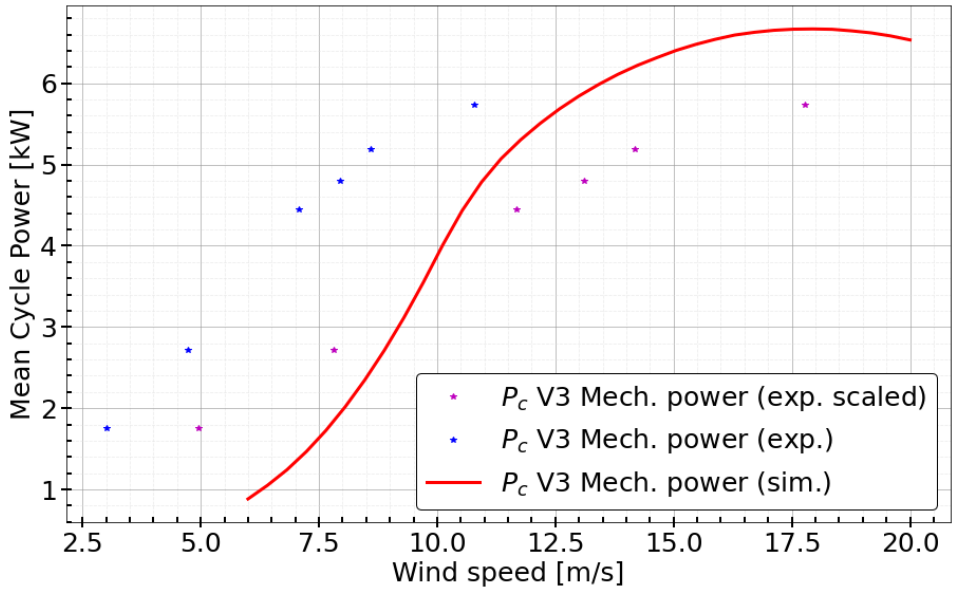

Figure 7.16: Mean cycle power for the V3 demonstrator kite experimental data vs QSM with mass

7.3. Scaling Study Verification

For the following section, the QSM time series considering mass was used to produce the following power curves. The Earth kite was modelled the same as Figure 7.16 and the scaled Mars kite as Figure 7.10 except that a 300 m^2 kite is modelled. This is because that is the original kite size computed in chapter 5. Note that the atmospheric density used for the Earth kite is 1.225 kg/m^3 and 0.01 kg/m^3 for the scaled Mars kite. According to the scaling study results in chapter 5, if the wind speed on Mars is twice that on Earth and the Mars kite is 15 times larger, then they should produce the same amount of power. However, the Earth kite's mean cycle power is 4 kW when the wind speed is 10 m/s, while the Mars kite produces the same power at 17.5 m/s. The difference between the desired double wind speed of 20 m/s and the actual wind speed is 2.5 m/s or 12.5% error. Therefore, it can be said that the scaling study is accurate enough to use as a first-order approximation.

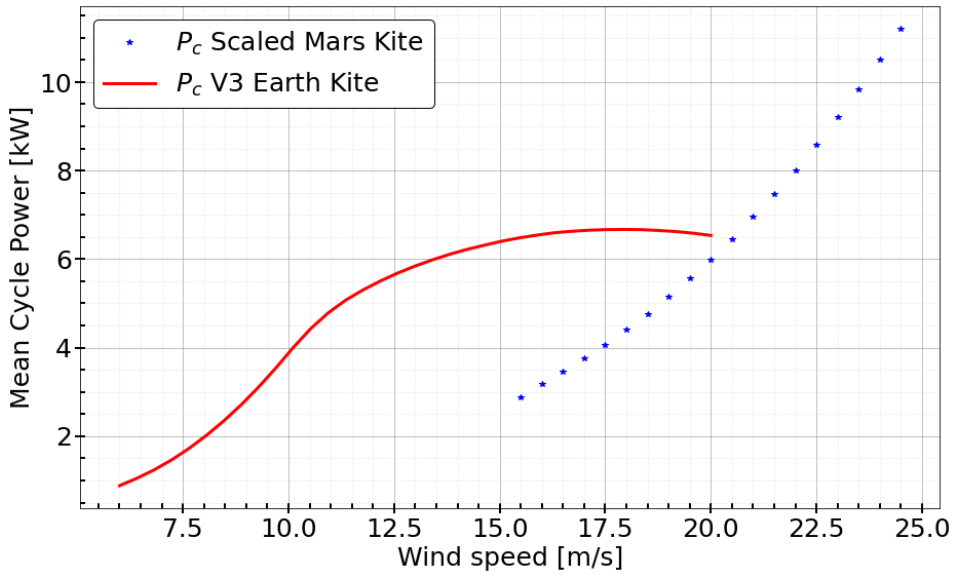

Figure 7.17: Mean cycle power for the V3 demonstrator Earth kite vs scaled Mars kite

8

Habitat Energy Model

This simplified habitat energy model is configured such that there is no long-term energy storage battery. While there still is a battery, it is relatively small and only used for buffering the short-term fluctuations in power production. Since there are four periods throughout the day where no wind energy is produced and the habitat requires a 10 kW continuous power supply, then a 40 kWh battery will be needed. This is equivalent to three Tesla Power 2 battery units weighing 342 kg [67], which we can use for the sake of comparison. Since there is no long-term energy storage battery being used in this model, the solar PV and AWE hybrid power plant must generate enough energy every day throughout the year. If the habitat needs 10 kW for 24 hours, then the hybrid power plant must generate at least 240 kWh per day.

Various configurations will be analysed using the habitat energy model which incorporates AWE, solar PV and energy storage. The solar panel area is computed using the habitat energy model, which is modified by the max solar condition value C_{solar}^{max}. If the needed power capacity, average Watt per area, conversion efficiencies, and line power losses are known then the required solar area can be computed. A detailed explanation of how the energy model works and how the solar PV area is computed can be seen in [20]. The mass of the solar PV is computed using a mass calculator developed by the first DSE. The solar PV mass is computed assuming the use of triple-junction GaInP/GaAs/Ge cells and use dual-axis support systems for sun tracking to reduce the incidence angle on the panels. Approximately, 80 percent of the mass of the solar subsystem was found to be about dual-axis support systems. Because the design of the solar subsystem is out of the scope of this thesis, the same subsystem design was used. However, this solar support system was previously needed by the first DSE because their location had much less solar flux. Arsia North is relatively close to Mars's equator. Therefore, in reality, such a complex and heavy solar support system should not be used. This would reduce the total power produced by a solar PV array, but also significantly reduce the mass of the solar subsystem. Future work should optimise the solar subsystem design to reduce the mass.

Throughout this section, only one kite size will be considered, namely, a 200 m^2 kite. By using the same method to compute the AWE system mass as [14], the mass was found to be 314 kg per AWE system. The number of kites and the maximum solar panel energy supply are varied. Four different cases are presented:

- Case 1 assumes that at any given day and period, the maximum solar energy supply is able to meet at most half of the energy demand. Two kites are considered and $C_{solar}^{max} = 0.5$
- To see the effect of increasing the max solar condition value C_{solar}^{max}, case 2 considers a $C_{solar}^{max} = 0.6$. Two kites are considered.
- Case 3 considers a $C_{solar}^{max} = 0.7$ in order to see if the energy deficit can be eliminated. Again, two kites are considered.
- Lastly, case 4 considers a $C_{solar}^{max} = 0$ in order to see if the energy deficit can be eliminated with kites alone. Three kites are now considered.

The adopted schedule of each sol is presented in Figure 8.1 below where on top of the timeline is the generated power of each period and below the line is the habitat demand [20].

	N_{kites}	AWE mass [kg]	C_{solar}^{max}	Solar Area [m^2]	Solar mass [kg]	Total mass [kg]
Case 1	2	628	0.5	32	388	1,016
Case 2	2	628	0.6	38	399	1,027
Case 3	2	628	0.7	49	409	1,037
Case 4	3	942	0	0	0	942

Table 8.1: Habitat Energy Model Inputs

	Total Solar Energy [kWh]	Total Wind Energy [kWh]	Total Battery Supply [kWh]	Deficit [kWh]
Case 1	16.7	214	93.3	8.2
Case 2	20	214	95.8	3.9
Case 3	23.4	214	98.3	0.8
Case 4	0	307.7	173.9	0

Table 8.2: Habitat Energy Model Outputs

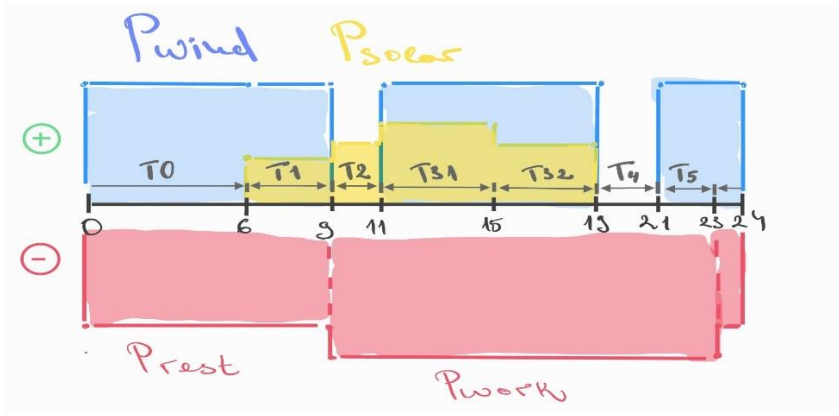

Figure 8.1: Sol energy schedule of habitat [20]

First, two 200 m^2 kites were used to produce energy. The maximum solar supply condition C_{solar}^{max} is set to 0.5, which means that for that sol and period; the secondary energy supply is able to meet half of the demand. According to Figure 8.2, the hybrid power plant can continuously provide a 10 kW power supply for most of the year. The energy deficit can be seen in the red shaded area in Figure 8.3.

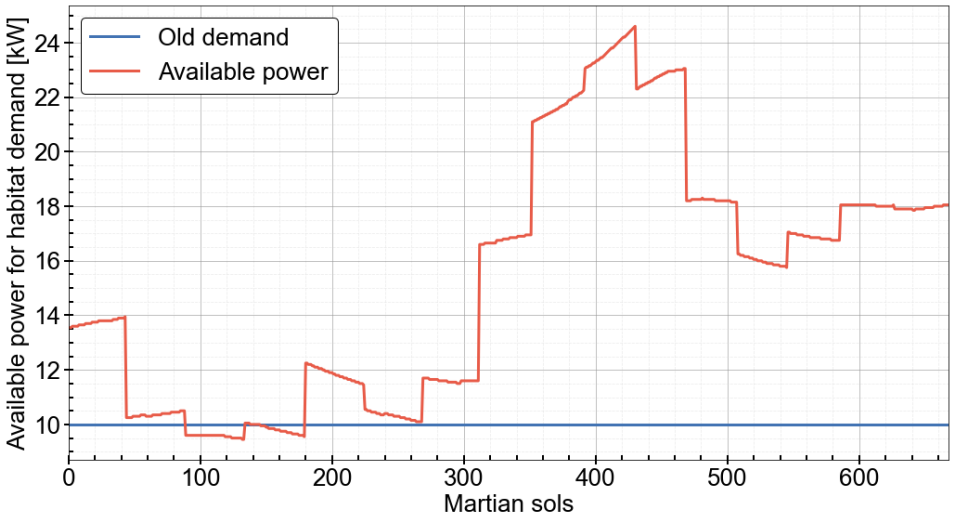

Figure 8.2: Available power for habitat demand $N_{\text{kite}} = 2$, $A_{\text{kite}} = 200$, $C_{\text{solar}}^{\text{max}} = 0.5$

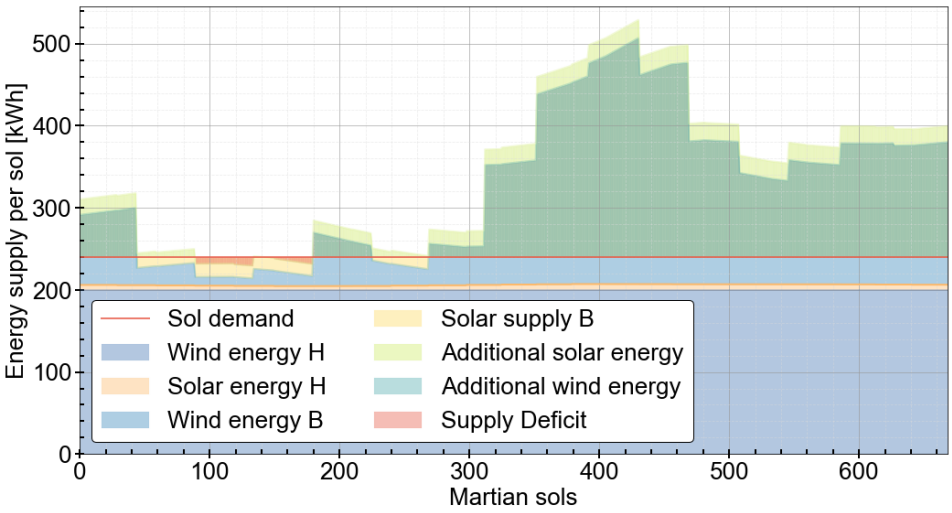

Figure 8.3: Energy supply per sol [kWh], $N_{kite} = 2$, $A_{kite} = 200$, $C^{max}_{solar} = 0.5$

Next, two 200 m^2 kites were used to produce energy, but the maximum solar supply condition C^{max}_{solar} is set to 0.6. This increases the amount of solar energy harvested, which can be most clearly seen in Figure 8.5 where the red-coloured area ”supply deficit” was reduced in size.

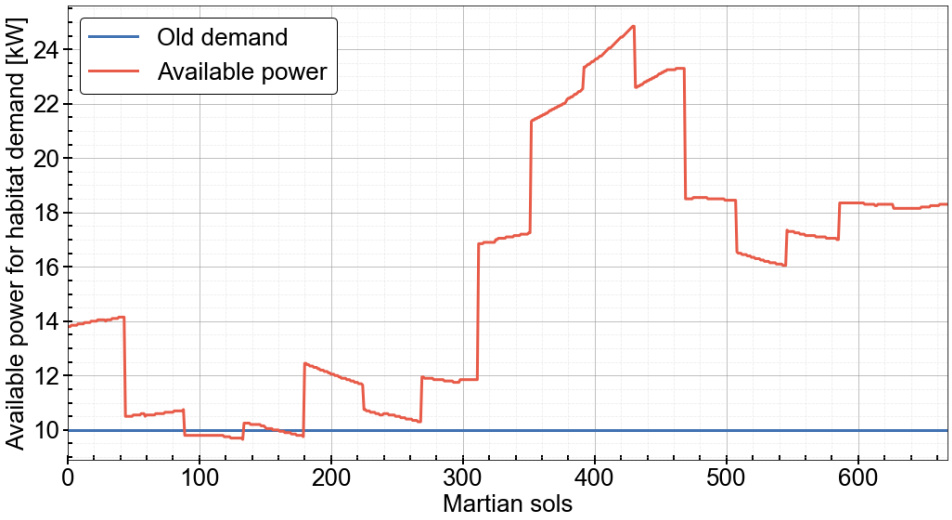

Figure 8.4: Available power for habitat demand $N_{kite} = 2$, $A_{kite} = 200$, $C^{max}_{solar} = 0.6$

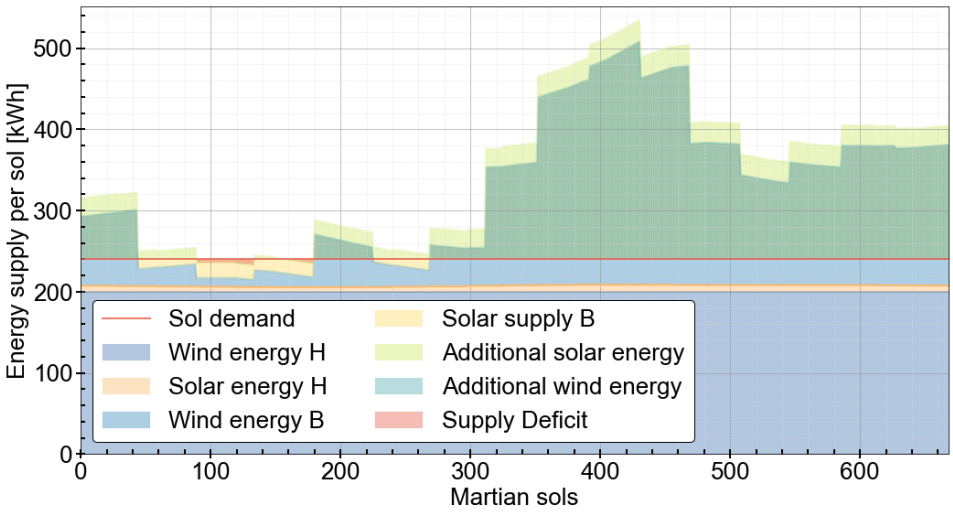

Figure 8.5: Energy supply per sol [kWh], $N_{kite} = 2$, $A_{kite} = 200$, $C^{max}_{solar} = 0.6$

Afterwards, two 200 m^2 kites were used to produce energy, but the maximum solar supply condition C^{max}_{solar} is set to 0.7. As can be seen in Figure 8.6 and Figure 8.7, the additional solar power supply is enough to meet the habitat power demand.

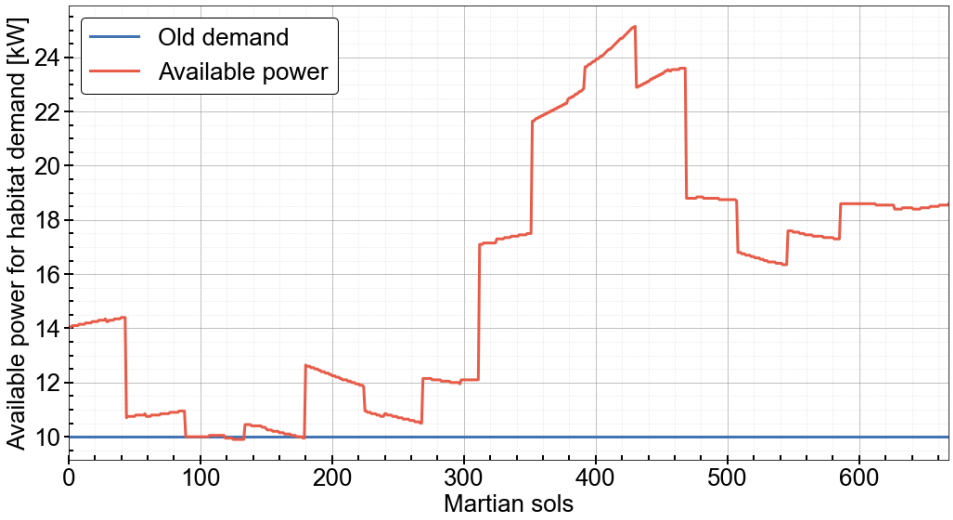

Figure 8.6: Available power for habitat demand $N_{kite} = 2$, $A_{kite} = 200$, $C^{max}_{solar} = 0.7$

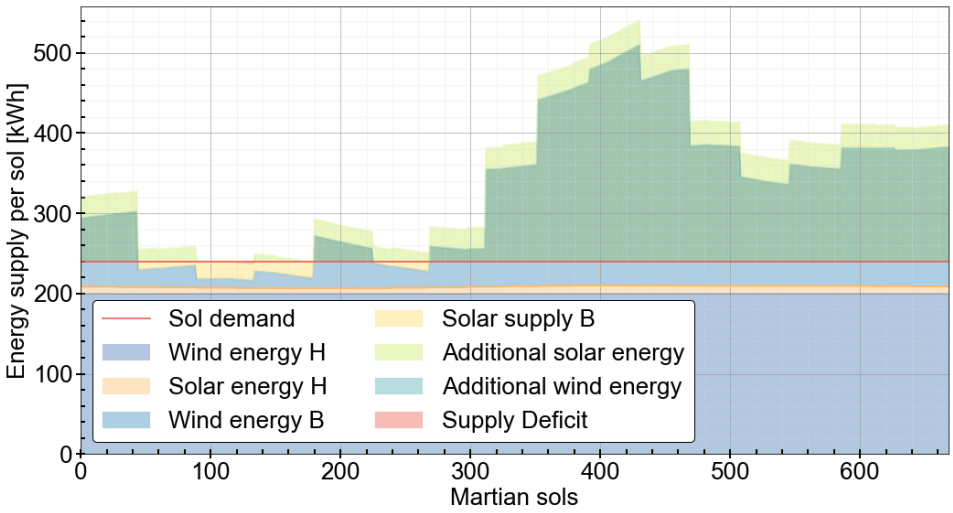

Figure 8.7: Energy supply per sol [kWh], $N_{kite} = 2$, $A_{kite} = 200$, $C^{max}_{solar} = 0.7$

Lastly, three 200 m^2 kites were used to produce energy, but the maximum solar supply condition C^{max}_{solar} is set to 0. This is equivalent to not having any solar power at all and solely relying on the AWE system for power generation. Figure 8.8 and Figure 8.9 show that the power and energy supply meets the power requirement. In fact, the design appears to be over-designed.

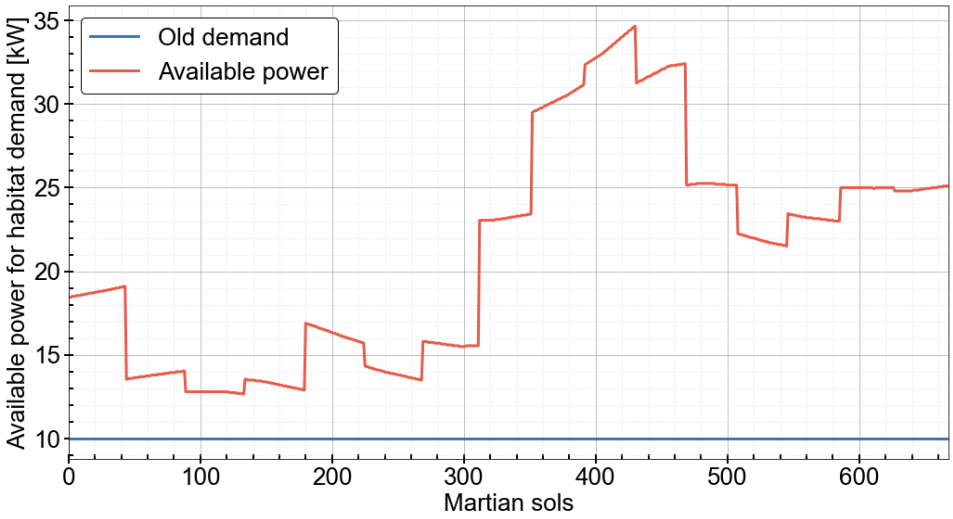

Figure 8.8: Available power for habitat demand $N_{kite} = 3$, $A_{kite} = 200$, $C^{max}_{solar} = 0$

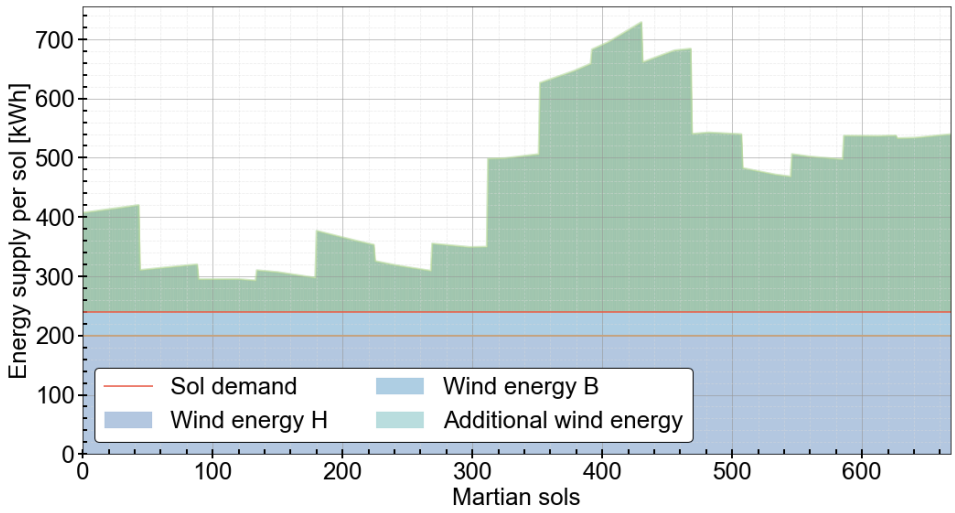

Figure 8.9: Energy supply per sol [kWh], $N_{kite} = 3$, $A_{kite} = 200$, $C_{solar}^{max} = 0$

By using the same method to compute the AWE system mass as [14], the mass was found to be 314 kg per AWE system. Although case 3 could work, adding more solar area is heavier than adding an equivalently powerful kite. Therefore, case 4 is considered to be the most optimal. However, more iterations must be done with larger kites in order to find the optimal configuration which lowers the overall hybrid power plant system mass, for example, using two 300 m^2 kites or using a combination of different kite planform areas. This option could be explored because the cut-in wind speed will increase as the area of the kite increases. Currently, the cut-in wind speed appears to be 15.5 with a 200 m^2 kite weighing 31.5 kg. So according to Figure 4.15, the average wind speeds at an altitude of 5 meters are higher than 15.5 during the late morning and afternoon. This means that the AWE would likely only be able to take off during these times. To work around this, the kite could be positioned downstream of the launch mast, and then reeled in. This would increase the apparent wind speed experienced by the kite and allow it to raise its altitude to reach higher wind speeds. It is also important to mention that the solar subsystem design was designed for another Mars location with much lower solar flux by the first DSE group. Therefore a new lightweight solar subsystem design could result in solar PV becoming more cost competitive and result in a different optimal design.

9

Conclusion

The main question of this project was whether an airborne wind energy system could generate the necessary energy to provide 10 kW of continuous power to a habitat throughout a Martian year. A basic wind resource assessment was carried out in two different locations and the better wind resource was chosen. 4 indicates that the average wind speed at pattern height can vary from 17.7-23.7 m/s, which according to Figure 7.10 corresponds with 5 - 14 kW. The dimensions of the kite were determined by using a scaling methodology in chapter 3. While [14] concluded a 50 m^2 kite would produce an average annual power output of 25 kW at Deuteronilus Mensae. This study concluded that a 200 m^2 kite would produce an average annual power output of 5.8 kW at Arsia North. Depending on the time of the year, the highest average wind speeds are experienced at an altitude between 150 - 175 meters, according to Figure 4.21.

A rigid or semi-rigid wing design implies the presence of both rigid and foldable elements in the wing. As the new pumping kite has an area of 200 m^2 the dimensions of the rigid elements would be way greater than previously anticipated which is not in line with the package design. Therefore, a leading-edge inflatable kite is considered to be the most optimal kite design for Mars as per transportation requirements. chapter 6 demonstrates how the hybrid power plant could rely solely on three 200 m^2 AWE kites and short-term energy storage to buffer supply throughout the periods of the day where there is no wind. Furthermore, the hybrid power plant could also be configured to rely less on kites and incorporate solar PV. Solar PV is thought to be heavier than adding another AWE system. Therefore, adding more kites is preferable to adding more solar in order to reduce launch costs. However, this is assuming the same solar PV tracking mounts as the first DSE. Designing a low-mass solar design will result in a different optimal hybrid power plant design because using solar PV would have less of a weight penalty. It was observed in Figure 7.10 that accounting for mass in the QSM resulted in a slightly higher mean cycle power due to a higher positive transition power. This thesis has shown that using a hybrid power plant which utilises three 200 m^2 kites and a 40 kWh battery could be used to continuously provide 10 kW to the habitat. AWE is especially well positioned for this opportunity since towered turbines won't work [17], solar energy alone would not be feasible due to long period global dust storms, and radioisotope thermoelectric generators are only an option until national Plutonium-238 stockpiles are exhausted [18]. AWE on Mars could potentially serve as a catalyst for increasing financial and technological support for the AWE sector here on Earth.

9.1. Future work

This thesis did not investigate the effects of the low Reynolds number flow (10^4) because too little is known about low-Reynolds airfoil performance in Martian conditions. Realistically, this will result in a slight reduction in performance due to issues with flow separation seen in laminar flow conditions. Further work should include more realistic polar curves computed by means of computational fluid dynamics.

The MCD does not model the vertical component of the wind realistically. This could affect the

performance of the AWE system. So future work should look into areas with low slope angles. The vertical wind profiles of each season should be incorporated into the models to produce power curves for different seasons. Then, the power per sol can be computed and this is used to compute the available power for habitat demand and energy supply per sol.

Notably, this thesis is not meant to give an optimal design, but instead, bolster AWE on Mars as a proof of concept. Thus, further work should be done on optimising the sizing of different components of a hybrid power plant. This could be done by iterating over different amounts of kites, solar areas, and energy storage capacity in order to minimize the weight of the system. Furthermore, a more realistic mass estimation for a solar subsystem near the equator should be considered.

Furthermore, the durability of the AWE system is not accounted for in this analysis. Durability for fabric wings such as LEI, foil and delta kites, is an issue. Performance is compromised soon and lifetime is usually around several hundred hours [22]. Individual developers have reported continuous operation of AWE systems over several days [23]. A Mars mission would require continuous operation for years. It is assumed that by the time humans go to Mars, AWE technology will have matured enough to be much more durable. Therefore, future work should focus on extending the lifetime of the kite and tether.

References

[1] Brian Dunbar. *Our place in the universe*. 2005. URL: https://www.nasa.gov/exploration/whyweexplore/Why_We_13.html.

[2] *Early Universe - Webb/NASA*. 2022. URL: https://webb.nasa.gov/content/science/firstLight.html.

[3] *The future of the space economy*. 2022. URL: https://www.nasdaq.com/space-economy.

[4] Eric Mack. *In 2022, the new space race will get more heated, crowded and dangerous*. Jan. 2022. URL: https://www.cnet.com/news/in-2022-the-new-space-race-will-get-more-heated-crowded-dangerous/.

[5] Mark Garcia. *NASA counts down to twenty years of human presence on station*. Oct. 2019. URL: https://www.nasa.gov/feature/nasa-counts-down-to-twenty-years-of-continuous-human-presence-on-international-space-station.

[6] *Artemis II*. 2022. URL: https://www.esa.int/Science_Exploration/Human_and_Robotic_Exploration/Orion/Artemis_II.

[7] Brian Dunbar. *Moon to Mars Overview*. June 2018. URL: https://www.nasa.gov/topics/moon-to-mars/overview.

[8] *NASA's FY 2020 budget*. 2020. URL: https://www.planetary.org/space-policy/nasas-fy-2020-budget.

[9] Sarah O'Brien. *Americans spend $56 billion on sporting events*. Sept. 2017. URL: https://www.cnbc.com/2017/09/11/americans-spend-56-billion-on-sporting-events.html.

[10] Victoria Masterson. *Relativity space is 3D-printing rockets to "make humanity multiplanetary"*. 2022. URL: https://www.weforum.org/agenda/2022/06/3d-printed-rockets-mars-tim-ellis-climate-change/.

[11] *Planetary protection*. 2022. URL: https://sma.nasa.gov/sma-disciplines/planetary-protection.

[12] *Planetary protection: Preventing microbes hitchhiking to space*. 2014. URL: https://www.esa.int/Enabling_Support/Space_Engineering_Technology/Planetary_protection_preventing_microbes_hitchhiking_to_space.

[13] David R. Williams. *Mars fact sheet*. 2021. URL: https://nssdc.gsfc.nasa.gov/planetary/factsheet/marsfact.html.

[14] Lora Ouroumova et al. "Combined Airborne Wind and Photovoltaic Energy System for Martian Habitats". In: *Spool* 8.2 (2021), pp. 71–85. DOI: spool.2021.2.6058.

[15] Leonard David. *NASA is mapping out plans for bigger, more capable Mars Helicopters*. July 2021. URL: https://www.space.com/nasa-designing-future-mars-helicopters.

[16] Christian Davenport. *NASA's Mars helicopter was supposed to fly five times. it's flown 28*. May 2022. URL: https://www.washingtonpost.com/technology/2022/05/13/nasa-ingenuity-mars-helicopter-perseverance/.

[17] Vera Schorbach and Tilo Weiland. "Wind as a back-up energy source for mars missions". In: *Acta Astronautica* 191 (2022), pp. 472–478. ISSN: 0094-5765. DOI: https://doi.org/10.1016/j.actaastro.2021.11.013. URL: https://www.sciencedirect.com/science/article/pii/S0094576521006093.

[18] Dan Leone — March 11 and Dan Leone. *U.S. plutonium stockpile good for two more nuclear batteries after Mars 2020*. Mar. 2015. URL: https://spacenews.com/u-s-plutonium-stockpile-good-for-two-more-nuclear-batteries-after-mars-2020/.

[19] Dilge Gül et al. *AWESOM: Airborne wind energy system on Mars*. Jan. 1970. URL: http://resolver.tudelft.nl/uuid:0298b063-7632-43f4-afa5-4065376df713.

[20] Henriette Bier. “Rhizome: Development of an Autarkic Design-to-Robotic-Production and -Operation System for Building Off-Earth Habitats (final report and movie)”. In: (May 2022). DOI: 10.4121/19867561.v1. URL: https://data.4tu.nl/articles/dataset/Rhizome_Development_of_an_Autarkic_Design-to-Robotic-Production_and_-Operation_System_for_Building_Off-Earth_Habitats_final_report_and_movie_/19867561.

[21] Matthew Lichter and Larry Viterna. “Performance and Feasibility Analysis of a Wind Turbine Power System for Use on Mars”. In: (Oct. 1999).

[22] Storm Dunker. “Ram-air wing design considerations for airborne wind energy”. In: *Airborne Wind Energy*. Springer, 2013, pp. 517–546.

[23] Jochem Weber, Melinda Marquis, and Aubryn Cooperman. *Airborne wind energy - NREL*. 2021. URL: https://www.nrel.gov/docs/fy21osti/79992.pdf.

[24] Simon D. Fraser. “Power System Options for Mars Surface Exploration: Past, Present and Future”. In: *Mars: Prospective Energy and Material Resources*. Ed. by Viorel Badescu. Berlin, Heidelberg: Springer Berlin Heidelberg, 2009, pp. 1–23. ISBN: 978-3-642-03629-3. DOI: 10.1007/978-3-642-03629-3_1. URL: https://doi.org/10.1007/978-3-642-03629-3_1.

[25] Shannah Withrow et al. “An Advanced Mars Helicopter Design”. In: Nov. 2020. DOI: 10.2514/6.2020-4028.

[26] Liz Kruesi. *Mars has two speeds of sound*. Apr. 2022. URL: https://www.sciencenews.org/article/mars-two-sound-speeds-laser-helicopter?utm_source=internal&utm_medium=email&utm_campaign=email_share.

[27] *Transonic Flight*. May 2021. URL: https://skybrary.aero/articles/transonic-flight.

[28] Kathryn Mersmann. *The fact and fiction of martian dust storms*. Sept. 2015. URL: https://www.nasa.gov/feature/goddard/the-fact-and-fiction-of-martian-dust-storms.

[29] G. Horneck et al. “Humex, a study on the survivability and adaptation of humans to long-duration exploratory missions, part I: Lunar missions”. In: *Advances in Space Research* 31.11 (2003). The Moon: Science, Exploration and Utilisation, pp. 2389–2401. ISSN: 0273-1177. DOI: https://doi.org/10.1016/S0273-1177(03)00568-4. URL: https://www.sciencedirect.com/science/article/pii/S0273117703005684.

[30] *Electrical power*. URL: https://mars.nasa.gov/mars2020/spacecraft/rover/electrical-power/.

[31] Loura Hall. *Kilopower*. Dec. 2017. URL: https://www.nasa.gov/directorates/spacetech/kilopower.

[32] Donald Barker, Gregory Chamitoff, and George James. “Resource Utilization and Site Selection for a Self-Sufficient Martian Outpost”. In: (May 1998).

[33] John Bluck. *ANTARCTIC/ALASKA-LIKE WIND TURBINES COULD BE USED ON MARS*. Oct. 2001. URL: https://www.nasa.gov/centers/ames/news/releases/2001/01_72AR.html.

[34] Sumedha Garud. *NASA Spinoff Article: Mars Technologies Spawn Durable Wind Turbines*. Tech. rep. 2013.

[35] Henry Haslach Jr. “Wind Energy: a Resource for a Human Mission to Mars”. In: *Jbis-journal of The British Interplanetary Society - JBIS-J BR INTERPLANET SOC* 42 (Jan. 1989).

[36] Alfonso Delgado-Bonal et al. “Solar and wind exergy potentials for Mars”. In: *Energy* 102 (2016), pp. 550–558. ISSN: 0360-5442. DOI: https://doi.org/10.1016/j.energy.2016.02.110. URL: https://www.sciencedirect.com/science/article/pii/S0360544216301724.

[37] Vera Schorbach and Tilo Weiland. “Wind as a back-up energy source for mars missions”. In: *Acta Astronautica* 191 (2022), pp. 472–478. DOI: 10.1016/j.actaastro.2021.11.013.

[38] C. Holstein-Rathlou et al. “Wind Turbine Power Production Under Current Martian Atmospheric Conditions”. In: *Mars Workshop on Amazonian and Present Day Climate*. Vol. 2086. LPI Contributions. June 2018, 4004, p. 4004.

[39] Vimal Kumar, Marius Paraschivoiu, and Ion Paraschivoiu. “Low Reynolds number vertical axis wind turbine for Mars”. In: *Wind Engineering* 34.4 (2010), pp. 461–476.

[40] URL: https://skysails-group.com/wp-content/uploads/2022/01/SkySailsMarine_Brochure_EN_web.pdf.

[41] “Airborne wind energy resource analysis”. In: *Renewable Energy* 141 (2019), pp. 1103–1116. ISSN: 0960-1481. DOI: https://doi.org/10.1016/j.renene.2019.03.118. URL: https://www.sciencedirect.com/science/article/pii/S0960148119304306.

[42] Chris Vermillion et al. “Electricity in the Air: Insights From Two Decades of Advanced Control Research and Experimental Flight Testing of Airborne Wind Energy Systems”. In: *Annual Reviews in Control* (Apr. 2021). DOI: 10.1016/j.arcontrol.2021.03.002.

[43] Vaughn Nelson. *Innovative wind turbines: An illustrated guidebook*. CRC Press Taylor amp; Francis Group, 2020.

[44] Bob Silberg. *Electricity in the air – climate change: Vital signs of the planet*. Nov. 2018. URL: https://climate.nasa.gov/news/727/electricity-in-the-air/.

[45] Roland Schmehl. *Airborne wind energy: AWESCO - Airborne Wind Energy System Modelling, control and optimisation*. June 2019. URL: http://www.awesco.eu/awe-explained/.

[46] Antonello Cherubini et al. “Airborne Wind Energy Systems: A review of the technologies”. In: *Renewable and Sustainable Energy Reviews* 51 (2015), pp. 1461–1476. ISSN: 1364-0321. DOI: https://doi.org/10.1016/j.rser.2015.07.053. URL: https://www.sciencedirect.com/science/article/pii/S1364032115007005.

[47] R.H. Luchsinger. “Pumping Cycle Kite Power”. In: *Airborne Wind Energy*. Ed. by U. Ahrens, M. Diehl, and R. Schmehl. Green Energy and Technology. Berlin Heidelberg: Springer, 2014. Chap. 3, pp. 47–64. DOI: 10.1007/978-3-642-39965-7_3.

[48] Rolf van der Vlugt et al. “Quasi-Steady Model of a Pumping Kite Power System”. In: *Renewable Energy* 131 (2019), pp. 83–99. DOI: 10.1016/j.renene.2018.07.023.

[49] Robert Boumis. *The average wind speed on Mars*. Mar. 2019. URL: https://sciencing.com/average-wind-speed-mars-3805.html.

[50] M.D. Paton et al. “Martian boundary layer wind profiles during the landings of Viking and InSight”. In: *Icarus* 367 (2021), p. 114581. ISSN: 0019-1035. DOI: https://doi.org/10.1016/j.icarus.2021.114581. URL: https://www.sciencedirect.com/science/article/pii/S0019103521002505.

[51] M. M. Joshi et al. “Western boundary currents in the Martian atmosphere: Numerical simulations and observational evidence”. In: *Journal of Geophysical Research* 100.E3 (Mar. 1995), pp. 5485–5500. DOI: 10.1029/94JE02716.

[52] M. Joshi et al. “Low-level jets in the NASA Ames Mars general circulation model”. In: *Journal of Geophysical Research E: Planets* 102 (Mar. 1997). DOI: 10.1029/96JE03765.

[53] E Millour. *The Mars Climate Database (Version 5.3)*. 2018. URL: http://www-mars.lmd.jussieu.fr/mars/access.html.

[54] M. M. Joshi et al. “Western boundary currents in the Martian atmosphere: Numerical simulations and observational evidence”. English. In: *Journal of Geophysical Research* 100.E3 (Mar. 1995), pp. 5485–5500. ISSN: 0148-0227. DOI: 10.1029/94JE02716.

[55] Scot Rafkin, Magdalena Rosario Sta. Maria, and Timothy Michaels. “Simulation of the atmospheric thermal circulation of a Martian volcano using a mesoscale numerical model”. In: *Nature* 419 (Oct. 2002), pp. 697–9. DOI: 10.1038/nature01114.

[56] Miles L. Loyd. “Crosswind kite power (for large-scale wind power production)”. In: *Journal of Energy* 4.3 (1980), pp. 106–111. DOI: 10.2514/3.48021.

[57] *Off-Earth Manufacturing and Construction (of Habitats)*. 2021. URL: http://cs.roboticbuilding.eu/index.php/Shared:2019Final.

[58] Francesco Sauro et al. “Lava tubes on Earth, Moon and Mars: A review on their size and morphology revealed by comparative planetology”. In: *Earth-Science Reviews* 209 (2020), p. 103288. ISSN: 0012-8252. DOI: https://doi.org/10.1016/j.earscirev.2020.103288. URL: https://www.sciencedirect.com/science/article/pii/S0012825220303342.

[59] *Mount Everest*. 2022. URL: https://education.nationalgeographic.org/resource/mount-everest.

[60] E Millour. *Martian Climate Database Documentation*. 2018. URL: http://www-mars.lmd.jussieu.fr/mars/info_web/index.html.

[61] Hannu Savijärvi and Tero Siili. “The Martian Slope Winds and the Nocturnal PBL Jet”. In: *Journal of Atmospheric Sciences* 50.1 (1993), pp. 77–88. DOI: 10.1175/1520-0469(1993)050<0077:TMSWAT>2.0.CO;2. URL: https://journals.ametsoc.org/view/journals/atsc/50/1/1520-0469_1993_050_0077_tmswat_2_0_co_2.xml.

[62] Mark Schelbergen and Roland Schmehl. “Validation of the quasi-steady performance model for pumping airborne wind energy systems”. In: *Journal of Physics Conference Series* 1618 (Sept. 2020), p. 32003. DOI: 10.1088/1742-6596/1618/3/032003.

[63] Rolf van der Vlugt, Johannes Peschel, and Roland Schmehl. “Design and Experimental Characterization of a Pumping Kite Power System”. In: *Airborne Wind Energy*. Ed. by Uwe Ahrens, Moritz Diehl, and Roland Schmehl. Green Energy and Technology. Berlin Heidelberg: Springer, 2013. Chap. 23, pp. 403–425. DOI: 10.1007/978-3-642-39965-7_23.

[64] U. Fechner and R. Schmehl. “Model-Based Efficiency Analysis of Wind Power Conversion by a Pumping Kite Power System”. In: *Airborne Wind Energy*. Ed. by U. Ahrens, M. Diehl, and R. Schmehl. Green Energy and Technology. Berlin Heidelberg: Springer, 2014. Chap. 14, pp. 249–269. DOI: 10.1007/978-3-642-39965-7_10.

[65] Roland Schmehl, Michael Noom, and Rolf van der Vlugt. “Traction Power Generation with Tethered Wings”. In: *Airborne Wind Energy*. Ed. by Uwe Ahrens, Moritz Diehl, and Roland Schmehl. Green Energy and Technology. Berlin Heidelberg: Springer, Oct. 2, 2013. Chap. 2, pp. 23–45. ISBN: 978-3-642-39964-0. DOI: 10.1007/978-3-642-39965-7_2.

[66] M.N. Noom. *Theoretical analysis of mechanical power generation by Pumping Cycle Kite Power Systems*. Jan. 1970. URL: https://repository.tudelft.nl/islandora/object/uuid:1c1a3e90-11e6-4fe7-8808-8c6a1227dadb?collection=education.

[67] Fred Lambert. *Tesla is increasing Powerwall power capacity by up to 50%*. Apr. 2021. URL: https://electrek.co/2021/04/22/tesla-increasing-powerwall-power-capacity)..

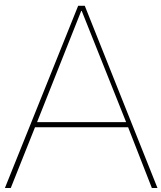

16 season parameters

Sols range	0 : 43	44 : 88	89 : 133	134 : 179	180 : 224	225 : 269	270 : 312	313 : 352
k	2.64	2.377	2.589	2.76	3.014	2.867	2.788	3.02
$u[m/s]$	19.452	18.002	17.635	17.827	18.714	18.422	19.158	21.479
Sols range	353 : 391	392 : 430	431 : 468	469 : 507	508 : 545	546 : 585	586 : 626	627 : 668
k	3.293	3.34	3.118	2.853	2.931	2.977	2.94	2.886
$u[m/s]$	23.478	23.919	23.042	20.999	20.025	20.534	21.249	21.273

(A.1)